Experimentelle Physik

Precision high voltage at the KATRIN experiment and new methods for an absolute calibration at ppm-level for high-voltage dividers

Inaugural-Dissertation
zur Erlangung des Doktorgrades
der Naturwissenschaften im Fachbereich Physik
der Mathematisch-Naturwissenschaftlichen Fakultät
der Westfälischen Wilhelms-Universität Münster

vorgelegt von
Oliver Rest
aus Lingen (Ems)

- 2019 -
(überarbeitete Version, Juli 2019)

WWU
MÜNSTER

Abstract

Since experiments observed neutrino oscillation in the 1990s, it is proven that these particles are not massless, as it is assumed in the Standard Model of particle physics. Experiments aiming to measure the neutrino mass could up to now only determine an upper limit of $2\,\mathrm{eV\,c^{-2}}$. As neutrinos are the most abundant massive elementary particles in the universe, their absolute mass scale is an important parameter for particle physics and cosmology. A model-independent method to determine the neutrino mass is given by the precise measurement of the endpoint region of β-decays. The goal of the KATRIN experiment is to measure the endpoint region of the tritium-β-decay with an unprecedented precision in order to determine the neutrino mass with a sensitivity of $0.2\,\mathrm{eV\,c^{-2}}$ (90 % C.L.). Decay electrons start in a windowless gaseous tritium source and their energy is measured with an electrostatic retarding spectrometer according to the principle of a MAC-E-filter. The retarding potential of the main spectrometer of about $-18.6\,\mathrm{kV}$ is created by mutliple HV supplies and distributed to a wire electrode system, which covers the inner surface of the spectrometer vessel. In order to reach the design sensitivity, the uncertainty of the HV monitoring has to be less than $60\,\mathrm{mV}$ (3 ppm) over a measurement period of 2 months. Within this thesis, first precision measurements with the HV system at the KATRIN main spectrometer were performed. These demonstrate, that the existing system outperformes the requirement with achieved uncertainies below $20\,\mathrm{mV}$ (1 ppm). In this context, two custom-made precision high-voltage dividers K35 and K65, which are used in order to measure the retarding potential of the main spectrometer, are of crucial importance. The calibration of the scale factors of these devices to the ppm-level could up to now only be performed at specialized metrology institutes or up to $1\,\mathrm{kV}$ with commercially available devices, in both cases not completely traceable to natural standards. In the context of this work, two new calibration methods were developed and applied successfully, which can be used in order to calibrate high-voltage dividers to the ppm-level on-site.

The basic idea of the first method is to operate commercially available devices of up to $1\,\mathrm{kV}$ on high-voltage potential to determine a differential scale factor, directly traceable to the Josephson voltage standard. This can be used in order to calculate the real scale factor, which could be demonstrated for the high-voltage divider K65 with uncertainties below $1\,\mathrm{ppm}$.

The second method utilizes mono-energetic conversion electrons from the decay of Kr-83m in order to calibrate the scale factor. By using the difference of two conversion electron lines, a large part of systematic uncertainties was eliminated, allowing the calibration of the voltage divider K35 directly traceable to a natural standard of a nuclear decay with an uncertainty of $5\,\mathrm{ppm}$.

Zusammenfassung

Seit in den 1990er Jahren der experimentelle Nachweis für Neutrinooszillation erbracht wurde, ist bekannt, dass die im Standardmodell der Teilchenphysik als masselos angenommenen Neutrinos eine Masse besitzen. Die Experimente zur Messung dieser Masse konnten bisher jedoch nur eine Obergrenze von aktuell $2\,\mathrm{eV\,c^{-2}}$ bestimmen. Da Neutrinos die häufigsten massebehafteten Teilchen im Universum sind, ist die Bestimmung ihrer Masse ein bedeutender Parameter für die Teilchenphysik und Kosmologie. Eine Möglichkeit zur modelunabhängigen Massenbestimmung bietet die präzise Vermessung des Endpunktbereichs von β-Zerfallsspektren. Das KATRIN Experiment zielt darauf ab, den Endpunktbereich des Tritium-β-Zerfalls mit bisher unerreichter Genauigkeit zu vermessen, um die Neutrinomasse mit einer Sensitivität von $0.2\,\mathrm{eV\,c^{-2}}$ (90 % C.L.) zu bestimmen. Dazu wird die kinetische Energie der in einer fensterlosen gasförmigen Quelle startenden Zerfallselektronen mit einem elektrostatischen Retardierungsspektrometer nach dem Prinzip eines MAC-E-Filters bestimmt. Die Retardierungsspannung dieses Spektrometers von etwa $-18.6\,\mathrm{kV}$ wird über ein komplexes Verteilungssystem auf die Drahtelektrode im Inneren des Spektrometertanks verteilt. Die Genauigkeit der Spannungsüberwachung muss mit $60\,\mathrm{mV}$ (3 ppm) über eine Messphase von 2 Monaten erfolgen um die angestrebte Sensitivität zu erreichen. Im Rahmen dieser Arbeit wurden erste Präzisionsmessungen mit dem Hochspannungssystem am Hauptspektrometer durchgeführt die zeigen, dass die erforderliche Genauigkeit erreicht und die Anforderungen mit Unsicherheiten im Bereich von $20\,\mathrm{mV}$ (1 ppm) übertroffen werden können.

Eine besondere Rolle nehmen dabei die für das Experiment entwickelten Präzisionshochspannungsteiler K35 und K65 ein, mit denen das Retardierungspotential des Hauptspektrometers direkt gemessen wird. Entscheidend ist dabei die Kalibration der Maßstabsfaktoren der Spannungsteiler, die mit ppm-Genauigkeit bisher nur in spezialisierten Metrologie-Instituten oder im Niederspannungsbereich bis $1\,\mathrm{kV}$ mit kommerziellen Geräten vorgenommen werden konnte, in beiden Fällen nicht vollständig rückführbar auf einen natürlichen Standard. Im Rahmen dieser Arbeit wurden zwei neue Techniken entwickelt und erfolgreich angewandt, die dies ermöglichen und mit deren Hilfe Hochspannungsteiler im ppm-Bereich vor Ort kalibriert werden können.

Die erste Methode basiert auf der Idee, kommerziell verfügbare Geräte bis zu $1\,\mathrm{kV}$ auf Hochspannungspotential zu verwenden und so einen differentiellen Maßstabsfaktor zu bestimmen, der auf Josephson-Spannungsnormale rückführbar ist. Daraus kann der reale Maßstabsfaktor berechnet werden, was anhand des K65 mit Unsicherheiten unter $1\,\mathrm{ppm}$ gezeigt werden konnte.

Grundlage der zweiten Methode sind mono-energetischer Konversionselektronen vom Kr-83m-Zerfall. Durch die Bestimmung der Differenz zweier Konversionselektronenlinien konnte ein Großteil systematischer Unsicherheiten eliminiert werden, sodass der K35 mit einer Genauigkeit von $5\,\mathrm{ppm}$ rückführbar auf den natürlichen Standard eines radioaktiven Zerfalls kalibriert werden konnte.

CONTENTS

INTRODUCTION

Neutrinos are the most abundant massive elementary particles in the universe. After their postulation in the 1930s by Wolfgang Pauli, it took experimental physicists more than 20 years to detect the neutrino for the first time. This charge-less elementary fermion is extremely hard to observe, because it interacts only via gravitation and weak interaction with corresponding small cross sections [1]. In order to study neutrinos, their properties and interactions, detectors like Super-Kamiokande [2], the Sudbury Neutrino Observatory (SNO) [3] and IceCube [4] use huge detection volumes in the order of kilotons and more. Even though significant technical and physical progress was achieved over the last decades, key questions regarding neutrinos are still not answered. Due to the experimental proof of neutrino oscillation by Super-Kamiokande and SNO, the prior assumption of massless neutrinos by the Standard Model of particle physics was proven wrong. In 2015 Takaaki Kajita and Arthur B. McDonald, representing their collaborations Super-Kamiokande and SNO, were awarded with the Nobel Price in physics for supplying the evidence that neutrinos have mass. This discovery gave a significant boost to the field. The current upper mass limit of about $2\,\mathrm{eV\,c^{-2}}$ [5] was determined by the Troitsk [6] and Mainz [7] neutrino experiments. Continuing this effort of the determination of the neutrino mass, the next generation experiment KATRIN aims to improve the sensitivity to $0.2\,\mathrm{eV\,c^{-2}}$.

In this chapter, a short historical overview about the exploration and discovery of neutrinos as well as experimental milestones are presented. The solar neutrino problem and its explanation with the theory of neutrino oscillation experiments is discussed subsequently. Finally, the different approaches for the determination

of the neutrino mass are presented. The discussions focus on key aspects and are mainly based on the references [8] and [9], where an extensive overview is given.

1.1 History of neutrino physics

The history of neutrino physics starts with the investigation of the β-decay by Chadwick in 1914 [10]. In contrast to the well known (two-body) α- and γ-decay, the energy spectrum of the electrons observed by Chadwick was continuous. In the physics community two possible explanations for this were discussed at that time. Either the energy conservation law was not valid for β-decays or an additional, at that time undetectable particle carried away a fraction of the energy. The latter assumption describes the process as three-body decay and was favored by Pauli, who wrote his famous letter regarding this issue in 1930 [11]. Therein, he postulated the existence of a neutral spin $1/2$ particle, which is emitted together with the electron. The sum of the kinetic energies in this three-body decay would be constant, conserving the overall decay energy. Shortly after the discovery of the neutron by Chadwick in 1932 [12], the theory of the β-decay was described mathematically by Fermi in 1934 [13]. He gave the particle the name *neutrino* and concluded, that its mass is small compared to mass of the electron. Fermi also deduced, that the neutrino mass influences the shape of the β-decay spectrum, especially in the endpoint region, where the electron gets most of the decay energy. This is the basis for neutrino mass measurements with the kinematic approach, which is discussed in section 1.5.
After the theoretical description it took experimental physicists about 20 years until the existence of the neutrino was proven by Cowan and Reines in 1956 [14]. Their experiment is based on the inverse β-decay

$$\overline{\nu}_e + p \rightarrow e^+ + n, \tag{1.1}$$

where an electron antineutrino $\overline{\nu}_e$ and a proton p are converted into a positron e^+ and a neutron n. Because of the small interaction cross section, an intensive neutrino source is needed in order to get enough statistics for an observation of this process. Therefore, the experiment was located at the Savannah River reactor in the USA, which provided a sufficiently high flux of antineutrinos.
An overview of the detection mechanism is shown schematically in figure 1.1. A liquid scintillator serves as detector and cadmium loaded water as target material. When an incoming antineutrino from the reactor is captured by a target proton, a positron (β^+) and a neutron are created. The positron annihilates with an electron (β^-) under the emission of two γ-rays with $511\,\mathrm{keV}$ each. The neutron is moderated by the scintillator and captured by the cadmium, which produces additionally emitted γ-rays. As a result of these two processes, coincident signals are recorded as a clear signature for the inverse β-decay, proving the existence of the neutrino.
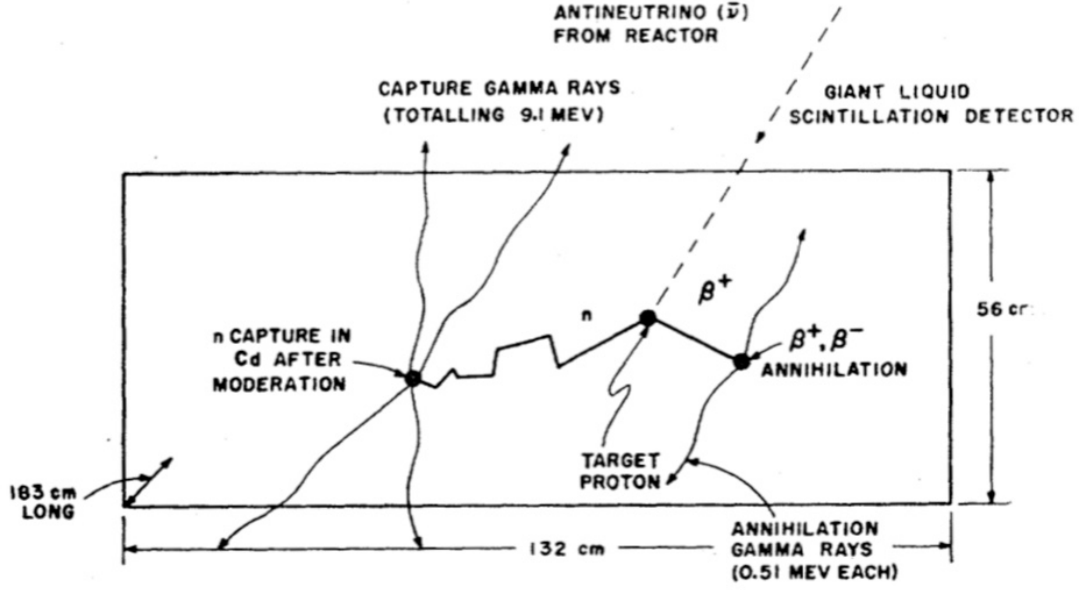
Figure 1.1: Schematic overview of the antineutrino detector used by Cowan and Reines. The incoming antineutrino converts a target proton into a neutron under the emission of a positron. The annihilation of the β^+ with an electron yields two γ-rays with $511\,\mathrm{keV}$ each. The neutron is moderated by the detector material, which is also loaded with cadmium. The Cd captures the neutron, which produces additional γ-rays. The image was taken from one of the original publications by Cowan and Reines in 1959 [15].

1.2 Neutrinos in the Standard Model

In the following years after the discovery of the neutrino, its properties and interactions were further investigated. Today, the standard model of particle physics describes all known particles and their interactions. The matter particles are fermions (spin $1/2$ particles), including six quarks and leptons (see table 1.1). Additionally, each particle has its antiparticle with opposite charge, but equal mass and spin[1].

The leptons consist of the electron, muon and tau and their corresponding neutrino flavors, forming a weak isospin doublet arranged into three generations. The actual number of neutrino species was investigated in the end of the 1980s with the Large Electron-Positron collider (LEP) at the European Organization for Nuclear Research (CERN) in Switzerland. Here, the width of the decaying neutral carrier of the weak force, the Z-boson, was measured. The decay width Γ_Z is defined as

$$\Gamma_\mathrm{Z} = \Gamma_\mathrm{ee} + \Gamma_{\mu\mu} + \Gamma_{\tau\tau} + \Gamma_\mathrm{had} + N_\nu \Gamma_{\nu\nu}, \tag{1.2}$$

---

[1]As neutrinos have no charge, it is still under investigation if they are their own antiparticles (Majorana nature) or not (Dirac nature).

Table 1.1: Periodic table of elementary matter particles in the standard model. The neutrinos form three generations of weak isospin doublets with their corresponding charged leptons. The table was taken from [8].

LEPTONS ℓ, spin $\frac{1}{2}\hbar$ (antileptons $\bar{\ell}$)						
electr. charge [e]	1. generation		2. generation		3. generation	
	flavour	mass [GeV/c^2]	flavour	mass [GeV/c^2]	flavour	mass [GeV/c^2]
0	ν_e electron neutrino	$< 2.5 \times 10^{-9}$ at 95% CL	ν_μ muon neutrino	$< 1.9 \times 10^{-4}$ at 90% CL	ν_τ tau neutrino	< 0.018 at 95% CL
-1	e electron	5.11×10^{-4}	μ muon	0.106	τ tau	1.777

QUARKS q, spin $\frac{1}{2}\hbar$ (antiquarks $\bar{q}$)						
electr. charge [e]	flavour	$\simeq$ mass [GeV/c^2]	flavour	$\simeq$ mass [GeV/c^2]	flavour	$\simeq$ mass [GeV/c^2]
$+2/3$	u up	1.5×10^{-3} to 4×10^{-3}	c charm	1.15 to 1.35	t top	174.3
$-1/3$	d down	4×10^{-3} to 8×10^{-3}	s strange	0.08 to 0.13	b bottom	4.1 to 4.4

where the first three terms represent the widths of decays into the charged leptons and Γ_{had} into the quarks (excluding the top-quark, since its mass is heavier than half of the Z-mass). By the simultaneous measurement of Γ_{Z} and observables related to the widths of charged leptons and hadrons, the contribution of the invisible decay width $\Gamma_{\nu\nu}$ and therefore the number of neutrino species N_ν can be determined. The measurement confirmed the assumption of three generations with

$$N_\nu = 2.9840(82) \qquad [16]. \qquad (1.3)$$

One has to keep in mind, that this number holds only for standard model neutrinos, participating in weak interaction. In recent years there were also discussions about the existence of a sterile neutrino, which interacts only via gravitation [17].

The electron (anti)neutrino measured by Cowan and Reines is a neutral spin-$1/2$ particle, which interacts only via gravitation and the weak force. Since the interaction cross section for the weak force is orders of magnitude smaller than for the electromagnetic interaction, the experimental examination of neutrinos was challenging in the beginning of neutrino physics. Within the Standard Model, the neutrinos are assumed to be massless. However, the observation of neutrino oscillation proves, that the mass is different from zero (see section 1.4). Until today, only an upper limit of $2\,\text{eV}$ [5] for the neutrino mass was determined

experimentally.

1.3 Solar neutrino problem

The sun releases its energy by nuclear fusion processes. The initial reaction is the fusion of two protons into deuterium d, a positron and an electron neutrino:

$$p + p \rightarrow d + e^+ + \nu_e. \tag{1.4}$$

The fact that this reaction proceeds via the weak interaction explains the longevity of the sun. Considering its huge mass, the sun is the biggest natural source for neutrinos on earth in our stellar neighborhood, producing a total flux in the order of 10^{10} particles per second and cm^2. The community of neutrino physics worked over several decades towards the measurement of these solar neutrinos in order to proof (among other things), that the origin of the released energy of the sun is based on nuclear fusion. Although almost 86% [8] of the solar neutrinos reaching the earth are produced in the reaction of equation (1.4), their energy was too small (well below $1\,\text{MeV}$) to be measured for a long time for most of the detectors. Recently, the BOREXINO collaboration reported about comprehensive measurements of the *pp*-reaction solar neutrinos [18].
However, there are following reactions in the proton-proton fusion chain of the sun, yielding neutrinos with higher energies. In this context, especially the β-decay of boron

$$^8\text{B} \rightarrow {}^8\text{Be} + e^+ + \nu_e \tag{1.5}$$

with neutrino energies of up to about $10\,\text{MeV}$ has to be mentioned. The first experiment which measured these solar neutrinos was the Homestake solar neutrino experiment by Davis in the 1960s. The basic detection reaction is given by

$$\nu_e + {}^{37}\text{Cl} \rightarrow {}^{37}\text{Ar} + e^- \tag{1.6}$$

with an energy threshold of $814\,\text{keV}$ [9]. A tank filled with $615\,\text{t}$ of perchlorethylene (C_2CL_4) served as detector. In order to shield the experiment against cosmic rays, it was installed at $1500\,\text{m}$ depth in the Homestake gold mine in the USA. The produced argon was volatile in solution and had to be removed every few months by flushing the system with a noble gas. Subsequently, the ^{37}Ar atoms were counted by the decay

$$^{37}\text{Ar} \rightarrow {}^{37}\text{Cl} + e^- + \overline{\nu}_e \tag{1.7}$$

with a half-life of $35\,\text{days}$. The ^{37}Cl atom emits $2.82\,\text{keV}$ X-rays or Auger electrons in order to re-arrange its electron structure since the electron capture predominantly occurs from the K-shell.
Because of the low expected capture rate of less than one neutrino per day, the experiment was designed to run over several years in order to gather enough
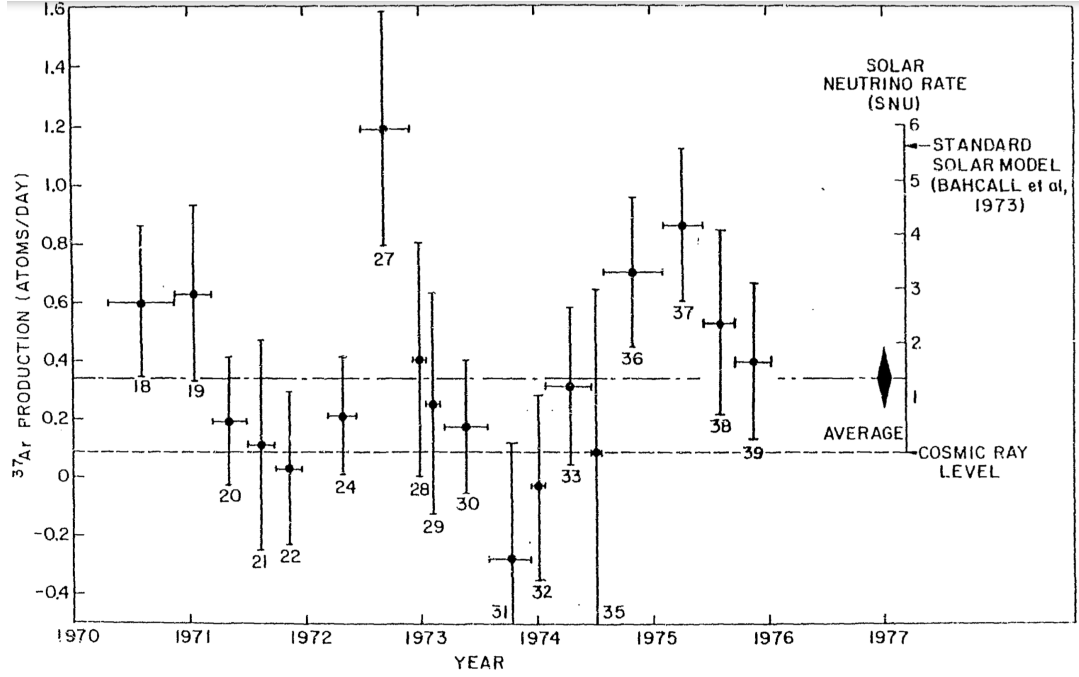
Figure 1.2: Result of the first years of operation of the Homestake experiment. The averaged production rate of ^{37}Ar atoms per day is shown for different years. The average value (and corresponding solar neutrino rate) is more than three times below the expected value by the standard solar model. The image was taken from the original publication by Ray Davis Jr. in 1976 [19].

statistics. During the operation time, it became more and more evident that there is a deficit of measured solar neutrinos. Figure 1.2 shows the determined production rate of ^{37}Ar per day for the first years of the experimental runtime published in 1976 by Davis. In average, only less than $0.4\,\text{atoms}\,\text{day}^{-1}$ were measured, corresponding to a solar neutrino rate more than a factor three below the expectations from the standard solar model. In 1998, after an operation time of over 20 years, the final results with an average ^{37}Ar production rate of

$$0.478 \pm 0.030 \text{ (stat)} \pm 0.029 \text{ (sys) atoms per day} \tag{1.8}$$

were published in [20], which is about a factor of three lower than the expected value. This discrepancy was called the *solar neutrino problem* and was solved in the end of the 1990s by the SNO- and Super-Kamiokande experiments. In 2002, Davis was awarded with the Nobel Prize in physics for his pioneering contributions to the field of neutrino astrophysics by measuring the solar neutrinos.

1.4 Neutrino oscillation

The **Sudbury Neutrino Observatory** (SNO) started its operation in 1999 with the goal to detect solar neutrinos and their composition. It is a real-time

Cerenkov detector using $1000\,t$ of heavy water (D_2O) in order to measure solar neutrinos with energies above $5\,MeV$. The D_2O is located in a transparent acrylic tank, surrounded by 9500 photo-multipliers. Several kilotons of pure water serve as a shielding against ambient radioactivity and the whole experiment is set up in $2100\,m$ depth of the Creighton Mine near Sudbury in Canada in order to reduce effects of cosmic rays.

The usage of heavy water as detector material allows the distinction between three different interaction mechanisms:

$$\nu_e + d \rightarrow e^- + p + p \qquad \text{(CC)} \qquad (1.9)$$

$$\nu_\alpha + e^- \rightarrow \nu_\alpha + e^- \qquad \text{(ES)} \qquad (1.10)$$

$$\nu_\alpha + d \rightarrow \nu_\alpha + p + n \qquad \text{(NC)}. \qquad (1.11)$$

The charged current (CC) is only sensitive to electron neutrinos ν_e, since the mass of the muon ($106\,MeV$) or tau ($1.8\,GeV$) is much higher than the kinetic energy of the neutrinos. Elastic scattering (ES) and neutral current (NC) reactions occur for all three flavors of neutrinos ν_α. The CC and ES processes are observed via Cherenkov light emitted by the electrons. In the case of the NC, the observation of the neutron is given by the reaction

$$n + d \rightarrow\, ^3H + \gamma \qquad (1.12)$$

via the detection of the gamma-rays with energies of about $6.3\,MeV$. By comparing the total flux in the CC channel with the NC channel, SNO was able to make a direct measurement of neutrino flavor changes. The total flux of all neutrinos measured via the NC channel was determined to be

$$\Phi_{\text{NC}} = 5.21(27)_{\text{stat}}(38)_{\text{sys}} \qquad [21] \qquad (1.13)$$

in agreement with the ^8B neutrino predictions obtained from solar models $\Phi_{\text{SSM}} = 5.31(60)$ [22]. For the CC channel, a significantly lower flux of

$$\Phi_{\text{CC}} = 1.59^{+0.08}_{-0.07}(\text{stat})^{+0.06}_{-0.08}(\text{sys}) \qquad [21] \qquad (1.14)$$

was measured, indicating that about two-thirds of electron neutrinos created in the sun change their flavor.

This can only be explained by neutrino oscillation and was the first observation and proof of physics beyond the standard model.

In general, the process of **neutrino oscillation** is based on the assumption, that the flavor eigenstates $|\nu_\alpha\rangle$ with $\alpha = (e, \mu, \tau)$ – corresponding to the eigenstates of the weak interaction – are not identical to the mass eigenstates $|\nu_i\rangle$ with $i = (1, 2, 3)$ of neutrinos, but connected via the matrix U_{PMNS}

$$\begin{pmatrix} \nu_e \\ \nu_\mu \\ \nu_\tau \end{pmatrix} = U_{\text{PMNS}} \cdot \begin{pmatrix} \nu_1 \\ \nu_2 \\ \nu_3 \end{pmatrix} = \begin{pmatrix} U_{e1} & U_{e2} & U_{e3} \\ U_{\mu1} & U_{\mu2} & U_{\mu3} \\ U_{\tau1} & U_{\tau2} & U_{\tau3} \end{pmatrix} \cdot \begin{pmatrix} \nu_1 \\ \nu_2 \\ \nu_3 \end{pmatrix} \qquad (1.15)$$

analog to the CKM-matrix [23] in the quark sector. The 3×3 mixing matrix

$$U_{\text{PMNS}} = \begin{pmatrix} c_{12}c_{13} & s_{12}c_{13} & s_{13}e^{-i\delta} \\ -s_{12}c_{23} - c_{12}s_{23}s_{13}e^{i\delta} & c_{12}c_{23} - s_{12}s_{23}s_{13}e^{i\delta} & s_{23}c_{13} \\ s_{12}c_{23} - c_{12}s_{23}s_{13}e^{i\delta} & -c_{12}c_{23} - s_{12}s_{23}s_{13}e^{i\delta} & c_{23}c_{13} \end{pmatrix} \quad (1.16)$$

with $s_{ij} = \sin(\theta_{ij})$ and $c_{ij} = \cos(\theta_{ij})$ can be parameterized by 3 angles $\theta_{ij} = [0, \frac{\pi}{2})$ and one[2] complex CP violating phase ($\delta = [0, 2\pi)$) [5]. It is named after Pontecorvo, Maki, Nakagawa and Sakata, who discussed neutrino oscillation and mixing for the first time.

A neutrino generated as flavor eigenstate in a weak interaction process can be written as superposition of the mass eigenstates

$$|\nu_\alpha\rangle = \sum_i U_{\alpha i} |\nu_i\rangle. \quad (1.17)$$

As the propagation through space takes place in the system of mass eigenstates

$$|\nu_i\rangle = \sum_i U^*_{\alpha i} |\nu_\alpha\rangle, \quad (1.18)$$

the applied time evolution operator yields

$$|\nu_i(t)\rangle = e^{-iE_i t} |\nu_i(t=0)\rangle \quad (1.19)$$

with the neutrino energy E_i and $\hbar = c = 1$. For the relativistic case that the momentum $p \approx E$ is much larger than the mass m, the approximation

$$E_i = \sqrt{p_i^2 + m_i^2} \approx p + \frac{m_i^2}{2p} \approx E + \frac{m_i^2}{2E} \quad (1.20)$$

can be assumed. As E_i depends on m_i, the mass eigenstates propagate with different velocities and therefore the flavor can change during the propagation, before the neutrino is detected – typically again via charged current reaction associated with a specific lepton flavor. In this case of $p >> m$ it can also be assumed, that the flight time t corresponds to a distance $L \approx t$. Therefore, the following equation can be derived

$$(E_i - E_j)t \approx \frac{m_i^2 - m_j^2}{2} \frac{L}{E} := \frac{\Delta m_{ij}^2 L}{2E}. \quad (1.21)$$

The time dependent probability P to measure a neutrino which changed its flavor from α to β during propagation through vacuum is given by

$$P(\alpha \to \beta, t) = \left| \sum_i U_{\alpha i} U^*_{\beta i} e^{-iE_i t} \right|^2 \quad (1.22)$$

$$= \sum_i |U_{\alpha i} U^*_{\beta i}|^2 + 2\text{Re} \sum_{j>i} U_{\alpha i} U^*_{\alpha j} U^*_{\beta i} U_{\beta j} e^{-i(E_i - E_j)t}. \quad (1.23)$$

---

[2]Assuming, that neutrinos are Dirac particles, one CP violation phase exists. Otherwise, two additional Majorana CP violation phases have to be considered.

Equation (1.23) can be divided into a time-independent average transition probability (first term) and an oscillation term, varying periodically with t or L/E, respectively. Using equation (1.23) and equation (1.21), one can derive the second basic assumption of neutrino oscillation: if neutrinos would be massless, the difference Δm_{ij}^2 would be zero and oscillations would not occur. Therefore, the experimental observation of solar neutrino oscillation by SNO proofed, that at least one mass eigenstate is non-zero. These findings were confirmed by Super-Kamiokande, where the oscillation of atmospheric and also solar neutrinos was observed [2].

For demonstration, it is appropriate to reduce neutrino oscillation to a mixing of two flavors, such that the PMNS-matrix is simplified to a 2×2 matrix with only one mixing angle θ:

$$\begin{pmatrix} \nu_\alpha \\ \nu_\beta \end{pmatrix} = \begin{pmatrix} \cos\theta & \sin\theta \\ -\sin\theta & \cos\theta \end{pmatrix} \begin{pmatrix} \nu_1 \\ \nu_2 \end{pmatrix}. \tag{1.24}$$

In this case, the transition probability is given by

$$P(\alpha \to \beta) = \sin^2(2\theta) \sin^2\left(\frac{\Delta m_{ij}^2 L}{4E}\right), \tag{1.25}$$

where the mixing angle defines the amplitude and Δm_{ij}^2 the oscillation frequency. For illustration, figure 1.3 shows the probability $P(\alpha \to \alpha)$ as function of L/E for an assumed mixing of $\sin^2 2\theta = 0.83$. The experimental investigation of oscillation parameters is done by measuring the ratio of flavor eigenstates at different lengths and energies. Three cases which are in this context important for experiments are shown in figure 1.3. When the factor L/E is much smaller than $1/\Delta m^2$, the experiment is too close to the source and oscillations can not be observed (a). For $L/E >> 1/\Delta m^2$, only an average transition probability can be measured, since several oscillations happened between the source and detector (c). The ideal case is $L/E \approx 1/\Delta m^2$, where experiments are most sensitive to oscillations.

In the past, numerous experimental approaches using different source types were pursued in order to investigate the mixing parameters. These sources can be divided into four categories: solar and atmospheric neutrinos are natural sources, which were investigated i.a. by SNO and Super-Kamiokande. Artificial sources are given by fission reactions in nuclear power plants (e.g. the Daya-Bay experiment) and accelerator neutrinos (e.g. the NOvA experiment).

Table 1.2 shows the neutrino mixing parameters, which are known to this day. As neutrino oscillation is only sensitive to mass differences and not to the absolute scale, the order of mass eigenstates is not known. There are two possible orders: in the so-called *normal hierarchy*, the case of $m_1 < m_2 < m_3$ occurs, whereas in the *inverted hierarchy* m_3 is smaller than $m_1 < m_2$. It is known from matter-enhanced neutrino oscillation (MSW-effect[3]), that $m_1 < m_2$ [24]. The mixing angle θ_{23} is nearly maximal, but it is not known if it is larger or smaller then $\pi/4$.

---

[3]The MSW effect is named after Mikheyev, Smirnov and Wolfenstein.

Table 1.2: Mixing parameters of neutrinos taken from [5]. The abbreviations NH and IH represent the normal and inverted mass hierarchy.

mixing angle	mass difference (eV^2)
$\sin^2(\theta_{12}) = 0.307 \pm 0.013$	$\Delta m^2_{21} = (7.53 \pm 0.18) \cdot 10^{-5}$
$\sin^2(\theta_{23}) = 0.421^{+0.033}_{-0.025}$ IH, $\theta < \pi/4$	
$\sin^2(\theta_{23}) = 0.592^{+0.023}_{-0.030}$ IH, $\theta > \pi/4$	$\Delta m^2_{32} = (-2.56 \pm 0.04) \cdot 10^{-3}$ IH
$\sin^2(\theta_{23}) = 0.417^{+0.025}_{-0.028}$ NH, $\theta < \pi/4$	
$\sin^2(\theta_{23}) = 0.597^{+0.024}_{-0.030}$ NH, $\theta > \pi/4$	$\Delta m^2_{32} = (2.51 \pm 0.05) \cdot 10^{-3}$ NH
$\sin^2(\theta_{13}) = (2.12 \pm 0.08) \cdot 10^{-2}$	

1.5 Determination of the neutrino mass

Since oscillation experiments are not sensitive to neutrino masses, this section gives a short overview of different experimental approaches to determine these parameters.
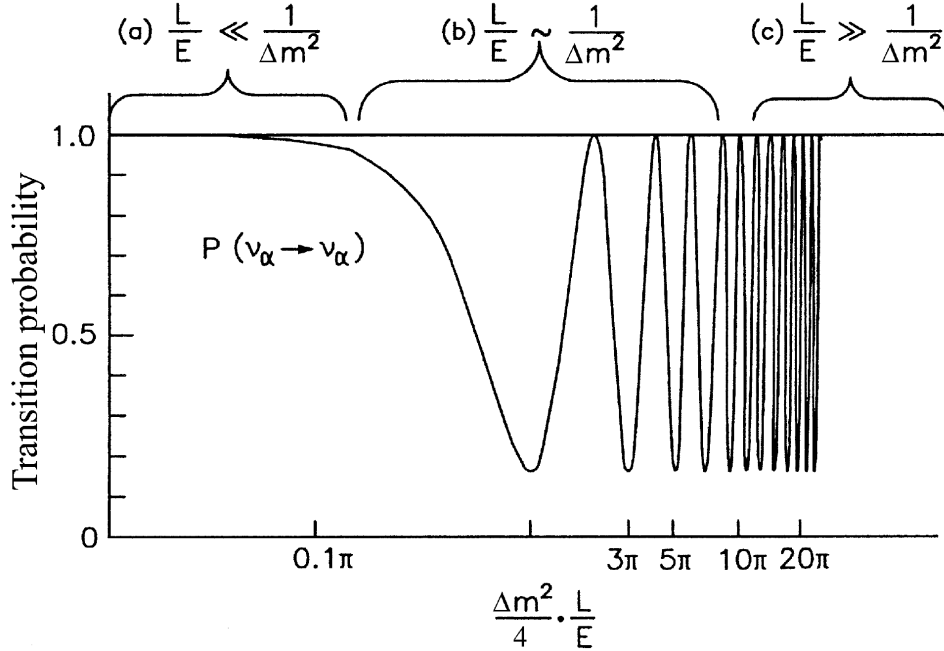

Figure 1.3: Oscillation probability for $P(\alpha \to \alpha)$ as function of L/E for an assumed mixing of $\sin^2 2\theta = 0.83$. The three cases (a,b and c) illustrate the case of no oscillation, oscillation and an average oscillation depending on the parameters L/E and $1/\Delta m^2$. The image was taken from [9].

Cosmology

As neutrinos are the most abundant massive particles in the universe, their mass has an influence on the evolution of the universe. It is assumed, that analog to the cosmic microwave background (CMB) relic neutrinos from the early universe form a low energy cosmic neutrino background with a number of $n_\nu = 336$ neutrinos per cm^3 [9].

The parameter obtained by cosmic observations is the sum of the neutrino masses $\sum_i m_i$. Cosmological calculations for the neutrino mass are model dependent and rely on the underlying physical phenomenon, e.g. the cosmic microwave background, structure formation and the distribution of galaxies in the universe, or supernovae. The most recent results were published in 2015 by the Planck collaboration. In this case, a satellite based experimental set-up was used in order to measure the CMB with high precision. The determined upper limit for the sum of the neutrino masses is

$$\sum_i m_i < (0.17 - 0.72) \text{ eV} \qquad [25] \qquad (1.26)$$

at 95 % C.L., where the exact value depends on the model parameters and the used data sets.

Neutrinoless double beta decay

The double β-decay ($2\nu\beta\beta$) is a process, where two β-decays occur simultaneously within a nucleus. It can be observed for isotopes, where the direct (single) β-decay ($n \to p + e^- + \overline{\nu}_e$) is energetically forbidden. The first experimental observation of this process was published 1987 in [26] for Se-82. Since these decays represent processes of second order of weak interaction, the probabilities are comparably low and the corresponding half-lives are in the order of 10^{20} years and higher.

A special case is the so-called neutrinoless double β-decay ($0\nu\beta\beta$). In this case, the $\overline{\nu}_e$ emitted at the first vertex is absorbed at the second vertex as ν_e, such that no neutrino leaves the system:

$$(Z, A) \to (Z + 2, A) + 2e^-. \qquad (1.27)$$

Here, Z corresponds to the number of protons and A to the number of nucleons in a nucleus. This process requires that neutrinos are their own anti-particles ($\nu = \overline{\nu}$, Majorana particles) and violates the lepton number, which is conserved in the Standard Model. The decay rate Γ for the ($0\nu\beta\beta$) scales with the so-called effective Majorana mass squared $m_{\beta\beta}^2$

$$\Gamma \propto \left| \sum_i U_{ei}^2 m_i \right|^2 := m_{\beta\beta}^2, \qquad (1.28)$$

with the complex mixing matrix elements U_{ei} in this coherent sum over the three mass eigenstates. The experimental signature of this decay is a discrete peak at the end of the continuous spectrum of the double β-decay, since the two emitted electrons carry the entire decay energy (neglecting the small recoil of the daughter nucleus).

The current upper limit of the neutrino mass determined by the GERDA collaboration using Ge-76 is given by

$$m_{\beta\beta} \leq (0.12 - 0.26) \text{ eV} \qquad [27], \qquad (1.29)$$

where the large uncertainties are caused by nuclear matrix elements, which are not precisely known.

Direct kinematic measurements

The neutrino mass can also be measured via direct kinematic measurements of a single β-decay

$$(Z, A) \rightarrow (Z + 1, A) + e^- + \overline{\nu}_e. \qquad (1.30)$$

In contrast to the previously mentioned methods, here the only assumptions for the determination of the average electron neutrino mass squared $m_{\nu_e}^2$, which is a weighted sum over the squared neutrino mass eigenstates

$$m_{\nu_e}^2 = \sum |U_{ei}^2| m_i^2, \qquad (1.31)$$

are energy and momentum conservation. According to Fermi′s golden rule, the spectral shape of the β-decay for a neutrino with mass $m_{\overline{\nu}_e}$ can be described by [28, 29]

$$\begin{aligned}
\frac{dN^2}{dEdt} =& \frac{G_F^2 \cos^2(\theta_C)}{2\pi^3} |M|^2 F(Z + 1, E) p(E - m_e) \\
& \cdot (E_0 - E)\sqrt{(E_0 - E)^2 - m_{\overline{\nu}_e}^2} \, \Theta(E_0 - E - m_{\overline{\nu}_e}),
\end{aligned} \qquad (1.32)$$

where E denotes the kinetic energy, m_e the mass and p the momentum of the electron. The endpoint energy E_0 is the maximal kinetic energy of the electron, when a vanishing neutrino mass is assumed. F is the Fermi- and Θ the step function. The parameter G_F denotes the Fermi constant, θ_C the Cabibbo angle and M the nuclear matrix element.

One can conclude from equation (1.32), that $m_{\overline{\nu}_e}$ only influences the shape of the spectrum via the factor $\sqrt{(E_0 - E)^2 - m_{\overline{\nu}_e}^2}$. Hence, the most significant impact of the neutrino mass is in the endpoint region. This is shown exemplarily for two assumed masses of 0 eV and 1 eV in figure 1.4. A non-zero neutrino mass changes the spectral shape.

Hence, for the experimental approach sources with a low endpoint energy are preferable, since in this case a bigger fraction of decay electrons is located in

that region. Additionally, the energy resolution of a detector is usually energy dependent and therefore better at lower energies. The β-decay source with the lowest energy of $E_0 = 2.47\,\text{keV}$ is Re-187. On the other hand side, this isotope has a half-life in the order of 10^{10} years and a rather complicated electronic structure. The isotope with the second lowest endpoint energy (tritium) does not suffer from this disadvantages. It offers a super-allowed [29] β-decay with a half-life of 12.3 years and features a simple electronic structure. With an endpoint energy of about $18.6\,\text{keV}$, the spectrum can be recorded with high precision using a MAC-E-filter type spectrometer (see section 2.2.1).

The current upper limit of the neutrino mass for direct measurements of the tritium β-decay with a MAC-E-filter was obtained by the Mainz [7] and Troitsk [6] experiments, where a combined analysis of the two experiments yield

$$m_{\overline{\nu}_e} < 2\,\text{eV} \qquad [5]. \tag{1.33}$$

The improvement of this result by one order of magnitude and the measurement of the neutrino mass with a sensitivity of $0.2\,\text{eV}$ (90 % C.L.) is the goal of the KATRIN experiment, which is the successor of the Mainz- and Troitsk experiments.

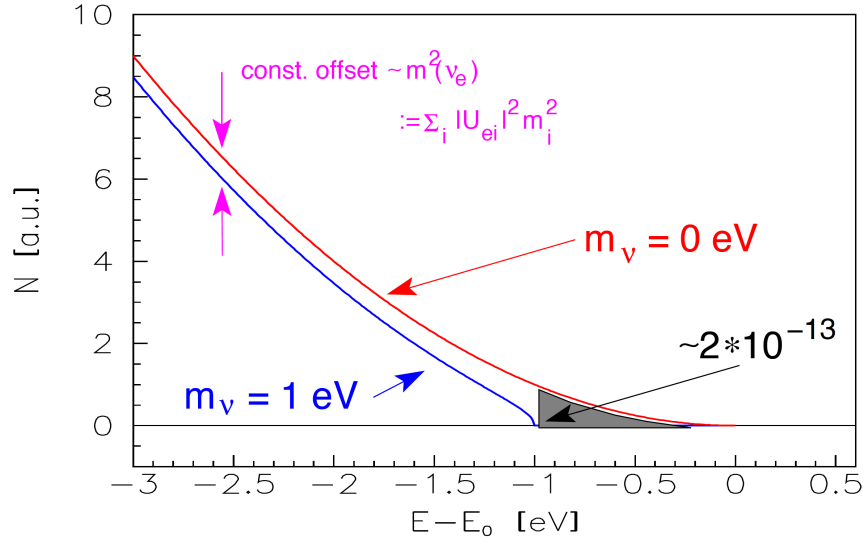**Figure 1.4:** Endpoint region of an allowed or super-allowed β-decay spectrum for two assumed neutrino masses. With a non-vanishing value of $m_{\overline{\nu}}$, the spectral shape is changed and the endpoint is shifted to lower energies. For tritium, only $2 \cdot 10^{-13}$ decay electrons appear in the last $1\,\text{eV}$ of the decay energy (see gray shaded area). The image was taken from [29].

1.6 Outline of this thesis

This thesis focuses on the high-voltage system of KATRIN and is structured in
the following way:

Chapter 2 gives an overview of the set-up of the KATRIN experiment, its
major components and their functionality. Furthermore, the general principle
of a MAC-E-filter and the technical realization by the main spectrometer are
discussed in more detail.

In **chapter 3** the systematic uncertainties of the KATRIN experiment are
discussed with a focus on the requirements for the high-voltage monitoring
system. Subsequently, the usage of Kr-83m conversion electrons for the high-
voltage calibration and the three different source types at KATRIN are presented.
Finally, the principle of electrical high-voltage calibrations is discussed.

Chapter 4 focuses on the set-up of the KATRIN main spectrometer high-
voltage system and its performance during commissioning measurements. In
the scope of this thesis, for the first time precision measurements regarding
the longterm stability of the whole apparatus were performed. Additionally, a
system for ppm-precise fast high-voltage measurements in the order of seconds
was developed. The set-up and first measurements are described in this chapter.
Furthermore, the contributions to other high-voltage components of KATRIN in
the context of this thesis are presented.

Chapter 5 is focused on a novel absolute calibration method for high-voltage
dividers, which was developed in the context of this thesis. After a brief overview
about the setup of the KATRIN high-voltage dividers and former calibration
methods, the idea of the newly developed absolute calibration procedure and the
technical realization are discussed. Finally, results of calibration measurements
performed over 1 year are presented.

In **chapter 6** a second newly developed calibration method of the KATRIN
high-voltage dividers with conversion electrons of Kr-83m is discussed. During
a krypton measurement campaign in 2017 at KATRIN, for the first time mea-
surements according to this calibration principle were performed. Furthermore,
results obtained with the newly developed fast high-voltage measurement system
are presented, which was tested successfully during this krypton campaign.

Chapter 7 summarizes the main results of this thesis and concludes with an
outlook.

The KATRIN experiment

The Karlsruhe Tritium Neutrino experiment (KATRIN) aims for the mass determination of the electron antineutrino by measuring the endpoint region of the tritium-β-decay spectrum. It is located at the Karlsruhe Institute of Technology (KIT) since the affiliated Tritium Laboratory Karlsruhe (TLK) provides infrastructure, experience and a sufficient amount of tritium which is necessary for the experiment. The discovery potential for the neutrino mass is $0.35\,\text{eV}$ at 5σ and a new upper limit of $0.2\,\text{eV}$ with a $90\,\%$ confidence level can be assumed if no mass is found [28]. This improves the current upper limit of the neutrino mass measured with the Mainz- and Troitsk neutrino experiments by one order of magnitude.

The experimental setup is shown in figure 2.1. In general, KATRIN features two major stages consisting of several subsections:

The **source and transport section** (STS) consists of the windowless gaseous tritium source (WGTS), where the tritium decays under the emission of electrons and neutrinos. Superconducting magnets create strong magnetic fields which are used to guide the electrons through the beam line. The rear section is used for calibration and monitoring of the source system. Utilizing differential and cryogenic pumping, gaseous tritium, deuterium, and hydrogen are removed from the beam tube.

The energy analysis of the electrons is pursued in the **spectrometer detector section** (SDS) consisting of the pre- and main spectrometer and the focal plane detector (FPD). The two spectrometers, as well as the monitor spectrometer, are operated as electrostatic spectrometers according to the principle of a MAC-E-filter (magnetic adiabatic collimation combined with an electrostatic filter).

One key parameter for the energy analysis with the main spectrometer is the high voltage, which creates the retarding potential. As one of the 5 major uncertainties (see section 3.1), the stability of the retarding potential has to be maintained and monitored with a precision of $60\,\mathrm{mV}$ at $-18.6\,\mathrm{kV}$ ($3\,\mathrm{ppm}$). The main topic of this thesis is the precision high-voltage system of the KATRIN experiment, which is discussed in detail in chapter 4.

In order to reach the desired sensitivity, key technologies of the predecessor experiments have to be improved and pushed beyond the limitations of state-of-the-art technology. One important example in the context of this thesis are the ultra-precise KATRIN high-voltage dividers, which were developed and built in cooperation with the German national metrology institute Physikalisch-Technische Bundesanstalt (PTB). In this work, a novel absolute calibration method was developed, presented in chapter 5.

In 2017, all major components of KATRIN had arrived at KIT and commissioning measurements with the whole beam line were performed. Before first tritium measurements in 2018 started, a Kr-83m measurement campaign was performed in order to study the system and check its functionality without the risk of tritium contamination. Results of the energy and HV calibration measurements performed in the scope of this thesis during the krypton campaign are discussed in chapter 6.

In the next sections, the main components of the KATRIN experiment are presented shortly. In particular, the functionality and operation mode of a MAC-E-filter is described in section 2.2.1. Since this thesis focuses on the high-voltage system and its calibration, the focus of the experimental description is set to this topic. Extensive information about the whole apparatus are given in the technical design report [28].

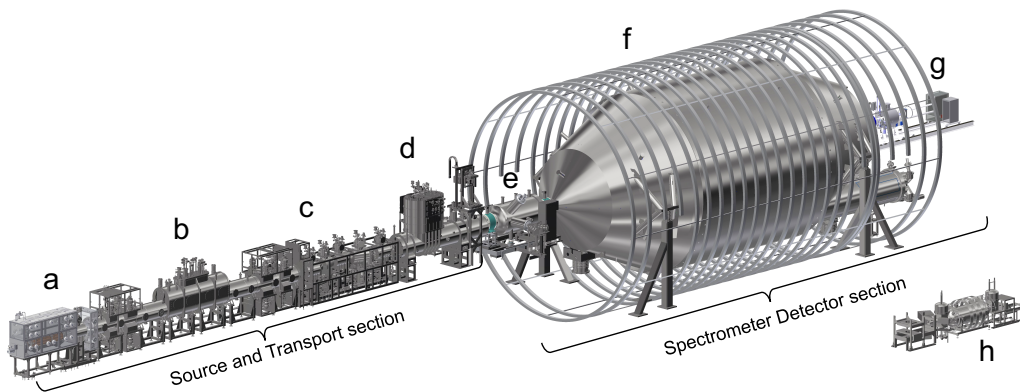
Figure 2.1: Setup of the KATRIN experiment: a) Rear section, b) windowless gaseous tritium source, c) differential pumping section, d) cryogenic pumping section, e) pre-spectrometer, f) main spectrometer, g) focal plane detector, h) monitor spectrometer. The whole beam line has a length of approx. $70\,\mathrm{m}$ and the largest diameter at the main spectrometer is about $10\,\mathrm{m}$.

2.1 Source and Transport Section

The main purpose of STS is on the one hand to provide the tritium of the WGTS and on the other hand to prevent it from reaching the spectrometer section. Since the handling of the radioactive tritium requires special safety regulations, this part of the experiment is contained in the area of TLK.

2.1.1 Windowless gaseous tritium source

The WGTS consists of a cylindrical tube of $10\,\mathrm{m}$ length and an inner diameter of $90\,\mathrm{mm}$. As depicted in figure 2.2, molecular tritium with high isotopic purity ($>95\,\%$) gets injected into the middle of the tube with a temperature of about $30\,\mathrm{K}$. The key parameter of the source regarding systematic uncertainties is the column density $\varrho d = 5 \cdot 10^{17}\mathrm{molecules\,cm^{-2}}$, which has to be known to a precision of $0.1\,\%$. Depending on the amount of gas inside the source, electrons leave the WGTS without interactions or with energy losses due to scattering with molecules. A diagnostic tool to investigate the energy loss of electrons in the source – an angular selective photo-electron source – is located in the rear section and is discussed briefly in the next section. Since the temperature of the gas is directly connected to the column density, the temperature stabilization of the system has to be constant to a level of $30\,\mathrm{mK}$.

While the β-decay electrons are guided adiabatically towards the transport- and spectrometer (and the rear-) section with strong magnetic fields provided by superconducting magnets, the tritium diffuses to both ends of the WGTS. There, it gets pumped out with two differential pumping sections (DPS1-R and DPS1-F) and fed back to the center by a closed loop system (see figure 2.2).

In total, the WGTS will provide about 10^{11} decay electrons per second with nearly $50\,\%$ being emitted in the direction of the FPD and guided by a magnetic flux of about $191\,\mathrm{T\,cm^2}$. One important aspect of the setup is the intentional waiving of a window or another mechanical separation between the WGTS and the rest of the experiment in order to avoid an unknown energy loss of the electrons. In addition to safety requirements concerning the radioactive isotope, there are also physical reasons to prevent tritium to reach the spectrometer section: decaying molecules would create an additional background at the focal plane detector. Therefore, the tritium which crosses the differential pumping section DPS1-F of the WGTS has to be removed in the transport section, which will be described in section 2.1.3.
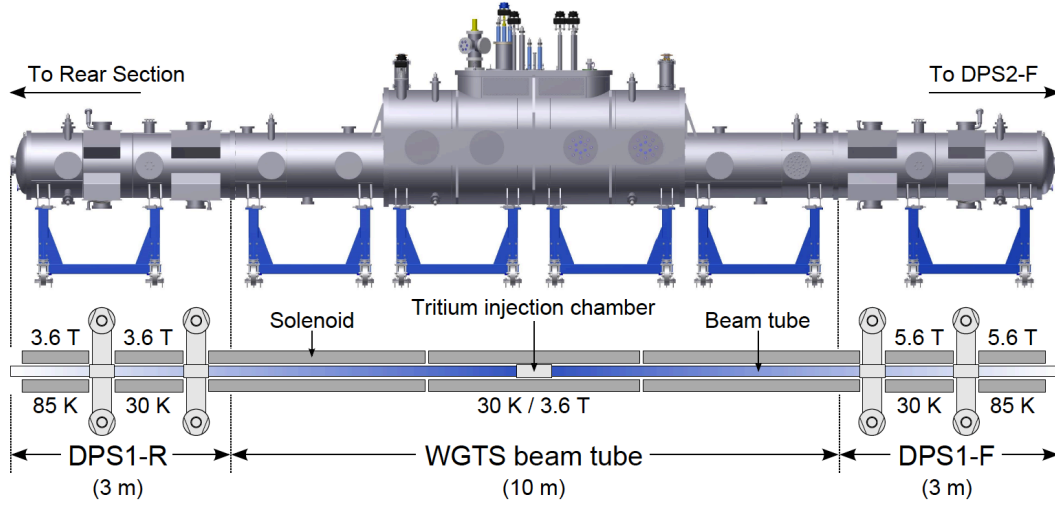
Figure 2.2: CAD model of the WGTS. Gaseous tritium with a temperature of 30 K gets injected in the center and is pumped out at both ends of the approx. 10 m long source tube by differential pumping (DPS1-F/R). The electrons are guided with magnetic fields created by superconducting magnets and follow the field lines to the adjacent transport section (right side). The left side of the WGTS is connected to the calibration and monitoring rear section. The image was taken from [30].

2.1.2 Rear section

In order to reduce systematic uncertainties related to the KATRIN source, the rear section (RS) (see figure 2.3) is used to monitor and calibrate WGTS properties in several ways. As mentioned in the previous section, the most important parameters here are the tritium column density and, directly connected, the source activity. Because of the importance of these parameters for the systematic uncertainties of the whole experiment, redundant monitoring systems are used: the activity is measured with the forward beam monitor [31] in forward direction and with beta-induced X-ray spectrometry (BIXS) within the rear section in backward direction [31]. The column density can also be investigated via inelastic scattering of mono-energetic electrons provided by a photo-electron source. Since the precise knowledge of the energy of the electrons is of crucial importance for this measurement, the difference between the acceleration voltage and the retarding potential of the main spectrometer has to be known to the 10 mV level at typical voltages of -18.6 kV. An overview of the HV system for the rear section photo-electron source is given in section 4.5.

The WGTS potential is of the same importance as the retarding voltage of the main spectrometer, since this potential difference is the observable for the spectroscopic measurements. Hence, a special rear wall with an optimized surface potential is used in order to control the potential of the WGTS [31].
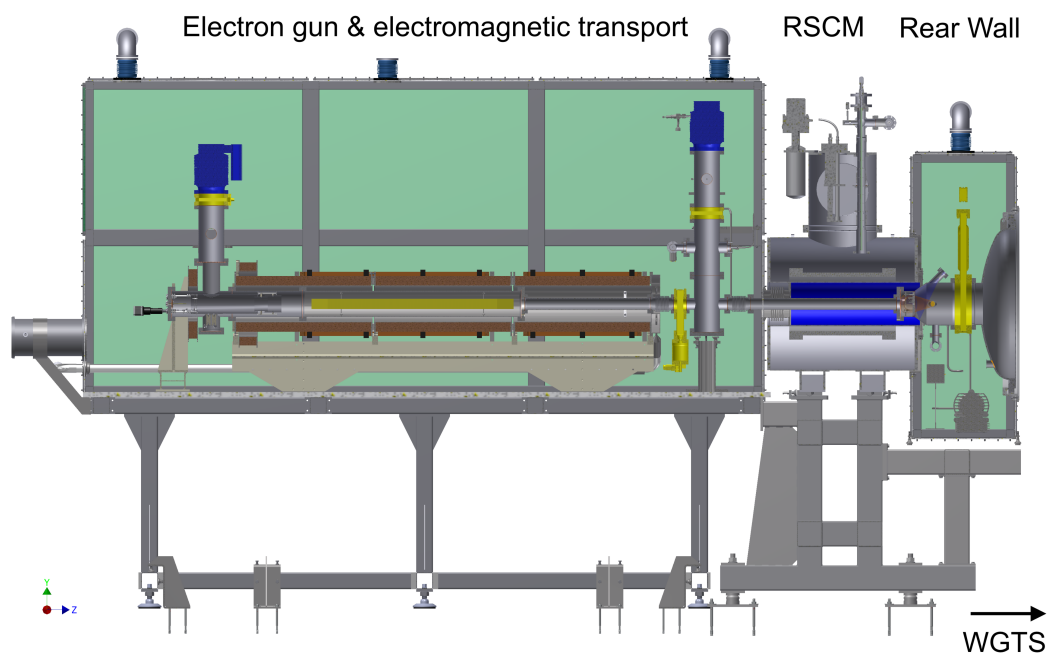
Figure 2.3: CAD model in half cut view of the rear section. The WGTS is connected on the right side at the chamber with the rear wall. The left part shows the setup of the photo-electron source. The image was taken from [32].

2.1.3 Transport section

Differential Pumping

In order to remove the tritium – which was not pumped out by the DPS1-F – from the beam tube, a second differential pumping section (DPS2-F) is directly connected to the WGTS (see figure 2.4 a)). It consists of five tubes with each 1 m length, whereat two segments are tilted by 20 degree compared to the beam axis of the experiment (compare figure 2.4 b)). By this alignment, the neutral molecules will collide with the walls of the beam tube and get pumped out by four turbo molecular pumps installed at the connection elements of the tubes. The electrons are guided by magnetic fields and can transit the DPS2-F undisturbed. The reduction factor of the DPS of about 100000 results in a remaining gas flow of only $\approx 10^{-7}\,\mathrm{mbar\,L\,s^{-1}}$.

Since positive charged ions – resulting from the decay of tritium – are also following the magnetic field lines, additional steps are required in order to remove them from the beam tube and prevent them from reaching the spectrometer section. The installed Fourier Transformation Ion Cyclotron Resonators (FTICR) [28] can be used to investigate the ion species and with electric dipole electrodes these positively charged particles can be removed.
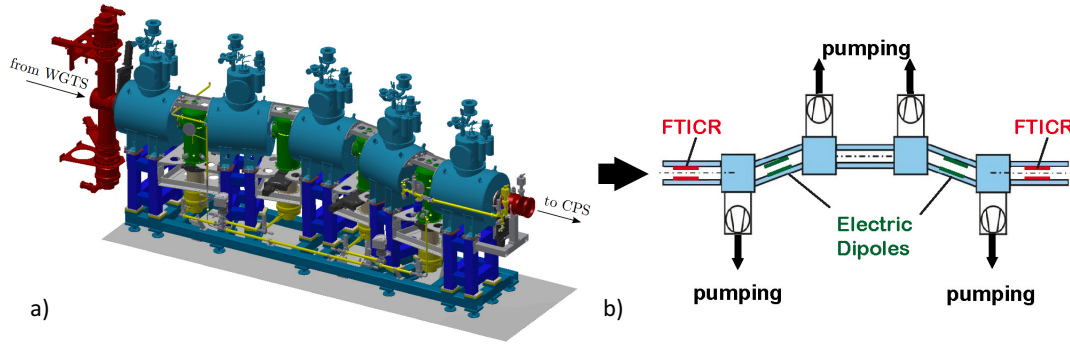
Figure 2.4: Differential Pumping Section 2 - F. a) CAD model of DPS2-F consisting of five (tilted) segments of $1\,\mathrm{m}$ beam tubes and superconducting magnets to guide electrons through the tilted beam line. The gas flow is reduced up to five orders of magnitude by four turbo molecular pumps. b) Schematic overview of DPS2-F. By this alignment, a direct line of sight between the KATRIN detector and the source is avoided, which prevents neutral particles from transiting the transport section, while the charged electrons are deflected by magnetic fields. The neutral tritium molecules hit the walls of the beam tube and are pumped out. Positively charged ions, which result from the decay of tritium, are removed from the beam tube with electric dipoles. Fourier transformation Ion Cyclotron Resonators (FTICR) can be used to investigate the ion species. The images were taken from [33] (a) and [34] (b).

Cryogenic pumping

With the cryogenic pumping section all remaining traces of tritium and other residual gases are trapped. Like at the DPSF-2, the alignment of the CPS is arranged with tilted segments in order to avoid a direct line of sight between the source and the detector and to increase the probability of tritium to collide with the walls of the beam tube. Since the inner surface of the gold plated tubes is cooled to $3\,\mathrm{K}$, tritium is trapped by cryo-sorption processes. In order to increase the surface area, the inner surface is covered with argon frost (see figure 2.5). When the surface is saturated with tritium after approximately $60\,\mathrm{days}$, the valves between CPS and DPS/ the spectrometers are closed and the system is heated to $100\,\mathrm{K}$. The evaporated gas gets pumped out with turbomolecular pumps and the tritium is reprocessed and fed into the WGTS.

At the end of the transport section, the partial pressure of tritium is reduced by twelve orders of magnitude compared to the inlet in the middle of the WGTS. The electrons are guided with magnetic fields and proceed to the spectrometer section.

At the CPS a condensed krypton source is installed for calibration and characterization measurements of the spectrometer detector section. More details about this system are given in section 3.2.2 and a detailed overview of the setup and commissioning is given in [35], [36] and [37].
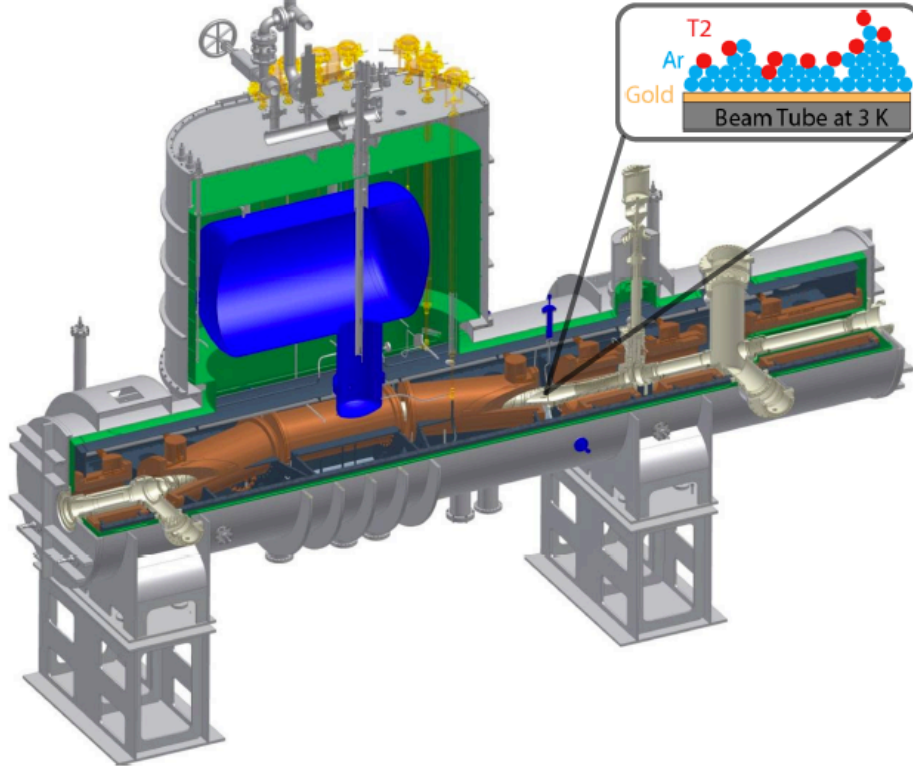
Figure 2.5: CAD model of the cryogenic pumping section. It consists of seven partially tilted segments with a gold plated inner surface, on which argon frost freezes out at a temperature of $3\,\mathrm{K}$. Tritium molecules are trapped via cryo-sorption. The image was taken from [38].

2.2 Spectrometer Detector Section

The spectrometer detector section consists of three electrostatic spectrometers (pre-, main- and monitor spectrometer) and the focal plane detector (FPD). Since all three spectrometers are operated as MAC-E filters, the main idea and concept of this kind of apparatus is discussed in the next section. Specific numbers (e.g. for magnetic fields) and calculations are assumed for the main spectrometer. Further details are given in [39].

2.2.1 MAC-E-filter

In order to measure the neutrino mass from the endpoint region of the β-decay spectrum of tritium one key parameter for the spectrometer is energy resolution. Since predecessor experiments showed that the mass is smaller than $2\,\mathrm{eV\,c^{-2}}$, the resolution of the KATRIN main spectrometer has to be in the order of $1\,\mathrm{eV}$ or better. Additionally, a high luminosity is essential, since the amount of
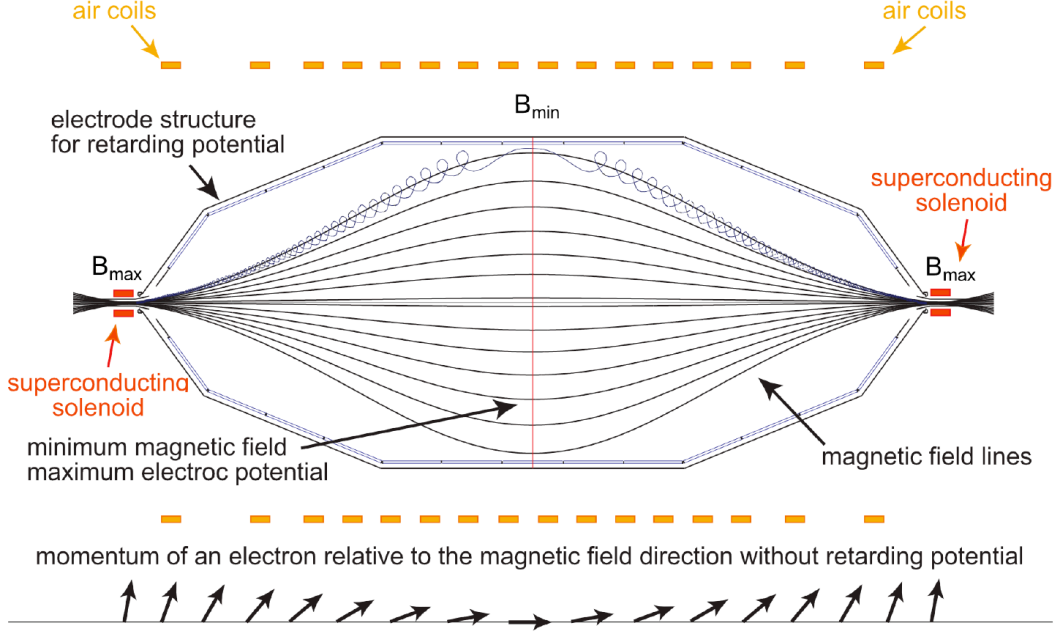
Figure 2.6: Principle of MAC-E filter explained for the KATRIN main spectrometer. Two superconducting solenoids (red) at both exits form a strong magnetic field, which decreases over several orders of magnitude towards the center of the spectrometer. Electrons are following the magnetic field lines on cyclotron motions. A retarding potential, which is applied to the electrode structure (blue), is used to record an integral spectrum of the β-decay electrons. The most negative potential is located at the center of the spectrometer (analyzing plane), where the minimal magnetic field strength is reached. The magnetic field of the earth is compensated with an air coil system (yellow). At the bottom of the figure, the conversion of the momentum direction of an electron starting with a high pitch angle is shown. In the analyzing plane, almost all momentum is transferred into longitudinal direction. The image was taken from [40].

tritium in the source is limited: as explained in section 2.1.1, a too high column density would go along with an increased scattering probability of the electrons and therefore a raised systematic uncertainty. Finally, the background of the spectrometer has to be small, since the count rate in the endpoint region is in the order of one electron per second.

All these features are characteristics of the magnetic adiabatic collimation combined with an electrostatic (MAC-E) filter. The operating principle of a MAC-E filter is shown in figure 2.6. Two superconducting magnets create a strong magnetic field B at both exits of the spectrometer. Arriving electrons with the mass m_e and charge e follow the magnetic field lines through the spectrometer on a cyclotron motion with the gyro-radius

$$r = \frac{\sqrt{2m_e E_\perp}}{eB}. \tag{2.1}$$

In the case of an isotropic source, the momentum vector of an emitted electrons has a certain pitch angle with respect to the magnetic field defined as polar angle θ. Thus, the kinetic energy E_{kin} is divided into two parts: one longitudinal $E_{\parallel}$ and one transversal $E_{\perp}$ to the magnetic field direction:

$$E_{\text{kin}} = E_{\parallel} + E_{\perp} = E_{\text{kin}}(\cos^2\theta + \sin^2\theta). \tag{2.2}$$

Since only the longitudinal part $E_{\parallel}$ is measured with a MAC-E-filter, the transversal component $E_{\perp}$ has to be converted into $E_{\parallel}$ in order to analyze the whole kinetic energy of the electrons. This is illustrated by the arrows in the bottom part of figure 2.6.

Because of the slow change of the magnetic field from the exits towards the center of the spectrometer, the transformation from transversal to longitudinal kinetic energy is adiabatic. In this case, the magnetic moment μ of the electron is constant during the transit through the spectrometer [41]

$$\mu = |\vec{\mu}| = \frac{e}{2m_e}|\vec{l}| = \frac{E_{\perp}}{B} = \text{const}, \tag{2.3}$$

which is assumed for the classical, non-relativistic case. Hence, the following equation can be derived:

$$\frac{E_{\perp}^{\text{source}}}{B_{\text{source}}} = \frac{E_{\perp}^{\text{ana}}}{B_{\text{ana}}} = \frac{E_{\perp}^{\text{pinch}}}{B_{\text{pinch}}}, \tag{2.4}$$

meaning, that the ratio is constant for the electrons in the source, in the analyzing plane at the center of the spectrometer, where the magnetic field reaches its minimum, and in front of the detector at the pinch magnet, where the magnetic field is at its maximum. The retarding voltage U_{ret} is applied to the vessel and creates a potential barrier, which the electrons have to overcome in order to reach the detector. If the kinetic energy is smaller than the retarding energy $e \cdot U_{\text{ret}}$, incoming electrons are reflected. Electrons with higher energies are transmitted. Accordingly, the transmission condition is given by

$$E_{\text{kin}} \geqslant q \cdot U_{\text{ret}}. \tag{2.5}$$

Figure 2.7 shows the transmission probability T as a function of the surplus energy of a general MAC-E filter. For mono-energetic electrons with only one fixed pitch angle it would be a sharp step function. However, due to the different distribution of pitch angles, a transition region between reflection and transmission of electrons appears depending on the surplus energy and the starting angle. In addition, the magnetic fields at the exit B_{pitch} and in the center B_{ana} of the spectrometer define the width of the transmission function ΔE_{trans}:

$$\Delta E_{\text{trans}} = E \cdot \frac{B_{\text{ana}}}{B_{\text{pinch}}} \cdot \frac{\gamma + 1}{2}. \tag{2.6}$$
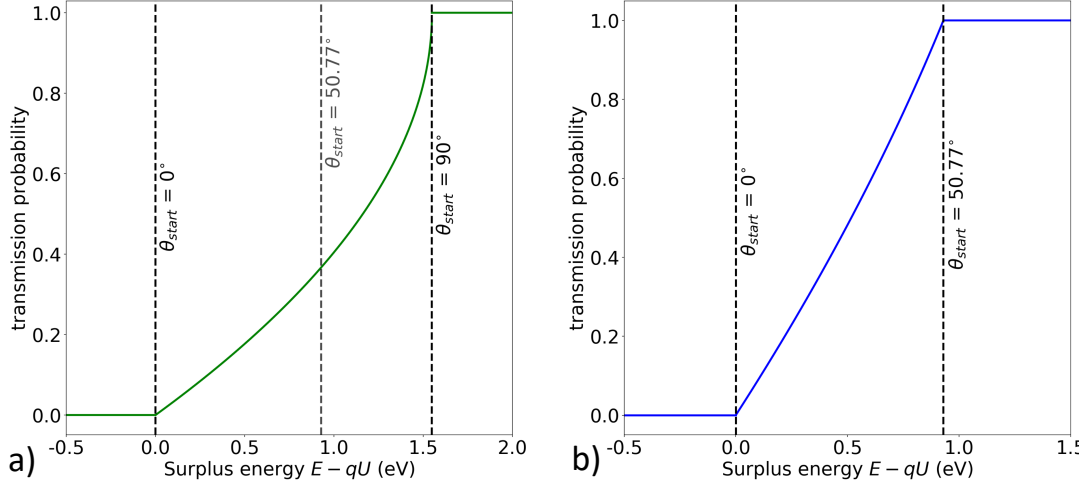
Figure 2.7: Transmission function of a MAC-E filter. a) General transmission probability as function of surplus energy. Electrons with a kinetic energy smaller than the retarding potential are reflected. For high surplus energies, the transmission probability is one. Due to different starting angles the transition is not a sharp step function, but a smeared out region. Electrons with higher starting angles than 90° will not reach the spectrometer, but are guided to the rear section. b) Since the magnetic field in the source is smaller than the maximum magnetic field of the pinch magnet, electrons with an angle higher than 50.77° are magnetically reflected. Hence, the transmission function is normalized to one at that angle, resulting in a width of 0.93 eV.

According to this equation, the energy resolution $\frac{\Delta E}{E}$ of a MAC-E filter depends on the ratio of the magnetic fields. The analytical transmission function is given by

$$
T(E, qU) = \begin{cases}
0 & \text{for } E - qU \leq 0 \\
1 - \sqrt{1 - \frac{E-qU}{E} \frac{B_{\text{source}}}{B_{\text{ana}}} \cdot \frac{2}{\gamma+1}} & \text{for } 0 < E - qU < \Delta E_{\text{trans}} \\
1 & \text{for } E - qU \geq \Delta E_{\text{trans}}
\end{cases} \quad (2.7)
$$

with the relativistic Lorentz factor γ of the electron.

Since a differentiation between electron energies higher than the retarding potential is not possible, the MAC-E filter works as a high-pass filter. The integrated β-decay spectrum is recorded by varying the retarding potential.

Equation (2.7) is derived by assuming an isotropic emitting source. For the KATRIN setup, the fact that the magnetic field in the source ($B_{\text{source}} = 3.6\,\text{T}$) is smaller than the maximum magnetic field leads to magnetic reflections of electrons with an angle θ higher than the cut-off angle

$$
\theta_{\text{start}}^{\text{max}} = \arcsin\left(\sqrt{\frac{B_{\text{source}}}{B_{\text{pinch}}}}\right) = 50.77°. \quad (2.8)
$$

In this case, only electrons with a smaller pitch angle are transmitted, independently from the starting energy. At energies of 18.6 keV and with $B_{\text{pinch}} = 6\,\text{T}$

and B_{ana} = 0.27 mT, this results in a width of the transmission function of 0.93 eV for KATRIN. Hence, equation (2.7) has to be normalized, which is shown in figure 2.7 b) and leads to the equation

$$T(E, qU) = \begin{cases} 0 & \text{for } E - qU \leq 0 \\ \frac{1 - \sqrt{1 - \frac{E - qU}{E} \frac{B_{\text{source}}}{B_{\text{ana}}} \cdot \frac{2}{\gamma + 1}}}{1 - \sqrt{1 - \frac{B_{\text{source}}}{B_{\text{pinch}}}}} & \text{for } 0 < E - qU < \Delta E_{\text{trans}} \\ 1 & \text{for } E - qU \geq \Delta E_{\text{trans}} \end{cases}$$

(2.9)

2.2.2 Pre- and main spectrometer

The first component of SDS is the pre-spectrometer (PS). Its main purpose is the reduction of the amount of electrons reaching the main spectrometer, where they could scatter on residual gas molecules and create additional background. A retarding potential of typically a few hundred eV below the one of the MS is applied to the cylindrical vessel with a diameter of 1.7 m and a length of 3.4 m. This results in the reflection of most of the β-decay electrons, while only the high-energy part of the spectrum (about 1000 electrons per second) is transmitted to the main spectrometer. For fine-tuning of the electrical field and in order to reduce background a simple inner wire electrode system is installed covering the inner surface of the spectrometer. By applying a slightly more negative potential to the wire electrode compared to the vessel, electrons coming from the walls are reflected. More details about the high-voltage system of the pre-spectrometer are given in section 4.4.

Since many of the requirements for both spectrometers in the KATRIN beam line are identical (e.g. ultra-high vacuum, high-voltage system with operation of the whole vessel up to −35 kV ...), the PS, which was the first major KATRIN hardware component at KIT, could be used as prototype and test system.

Following the PS, the main spectrometer (MS) is used in order to scan the endpoint region of the tritium β-decay with unprecedented precision. With a length of 23 m and a diameter of 10 m, it is the largest single component of the KATRIN setup. Via three pump ports with a diameter of 1.7 m an ultra-high vacuum in the order of 10^{-11} mbar is created with multiple non-evaporative getter (NEG)- and turbomolecular pumps. Details about the commissioning of the vacuum system are given in [42].

Figure 2.8 shows two pictures of the MS. As one can see on the left image, the stainless steel vessel is surrounded by a large air coil system, which is used mainly for compensating the magnetic field of the earth and in order to shape the magnetic field in the center of the spectrometer. Furthermore, it can be used for background reduction by removing stored charged particles by a magnetic pulse method, which is described in [43] and [44].

A two layer wire electrode system ([45], [46]), which is shown on the right side of figure 2.8, covers the whole inner surface of 650 m^2. In total, it consists of 248

modules which are arranged in 15 electrically isolated rings and two separate dipole halves. The main task of the wire electrode is to fine-tune the shape of the retarding potential inside the MS. Furthermore, by applying a more negative voltage of generally a few hundred Volts compared to the vessel, low-energy electrons coming from the spectrometer walls are reflected. These electrons are mainly created by cosmic muons hitting the vessel. This is described in more details in section 4.1.1.

During bake-out processes, which were performed in order to improve the vacuum conditions of the MS, some parts of the wire electrode system were deformed and created a short circuit between wire layers and rings. Details about this challenge and repair attempts are reported in [37]. One possibility to check and monitor the integrity of the wire electrode system is a capacitance measurement, which is described in [47].

Since the MS retarding potential is of crucial importance for the measurement of the neutrino mass, its maintenance and monitoring is one of the key challenges of the whole experiment. Details about the HV system are discussed in chapter 4. In general, two independent solutions are used in order to guarantee system redundancy: two ultra-precise high-voltage dividers (see section 5.1) are used to measure the retarding potential directly. In addition, the monitor spectrometer is used to monitor the retarding potential of the MS (see next section).

Figure 2.8: Main spectrometer. a) View from the detector to the source side along the beam axis. The air coil system surrounds the MS vessel. b) View from the inside showing the wire electrode system covering the whole inner surface. The images were taken from [34].

2.2.3 Monitor spectrometer

The spectrometer of the former Mainz neutrino mass experiment (see figure 2.9) is directly connected to the retarding potential of the main spectrometer and used as monitor spectrometer (MoS) [48]. The longterm stability of the HV is monitored by a comparison to the nuclear standard of Kr-83m conversion electrons. This isotope offers a variety of multiple conversion electron lines (see section 3.2.1), whereat the K-32 line with an energy of 17.8 keV is of major
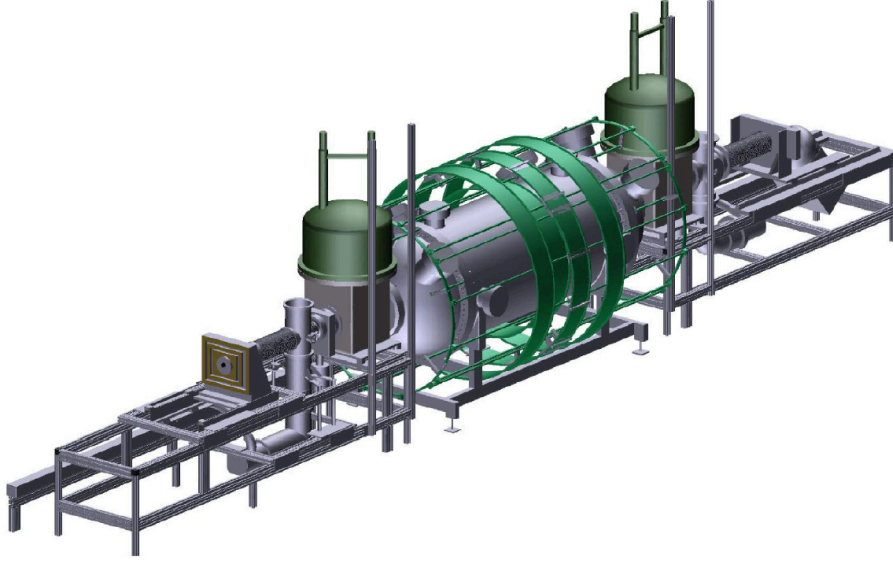
Figure 2.9: CAD-drawing of the monitor spectrometer. Previously used at the Mainz neutrino mass experiment, it is now installed at KIT and electrically connected to the retarding potential of the main spectrometer. The stability of the HV is monitored by a comparison with conversion electrons of Kr-83m. Since the MoS is a standalone system and not part of the KATRIN beam line, online monitoring during tritium measurements can be performed. The image was taken from [52].

importance because of the proximity to the tritium endpoint. Due to this properties, Kr-83m is used in three calibrations sources over the whole KATRIN experiment with different source conditions: gaseous, condensed and implanted (see section 3.2). A HV calibration method with gaseous Kr-83m is described in detail in chapter 6.

At the MoS, implanted sources of Rb-83 (the parent isotope of Kr-83m) in a solid body of highly oriented pyrolytic graphite (HOPG) are used [49]. After the decay, the electrons are facing the spectrometer, which also works as a MAC-E filter and an integrated spectrum is recorded. Because of the different energies of the tritium endpoint and the K-32 conversion electrons, the source can be set to a potential of about $-800\,\text{V}$.

The MoS can only be used for the longterm monitoring of relative changes of the retarding potential due to the unknown energy loss of electrons in the solid state body. Over the last years, it could be demonstrated, that ppm-stable and reproducible measurements with the system are possible [50, 36, 33, 51].

2.2.4 Detector

Following the spectrometers, the focal plane detector (FPD) completes the beam
line. Since the energy analysis of the electrons is performed with the main
spectrometer, in principle only a simple electron counter would be required in
order to record the integral spectrum. However, information about the spatial
and temporal distribution of the arriving electrons provide the possibility to
characterize the whole apparatus and even perform non-standard measurements.
One important idea to mention in this context are time-of-flight measurements
[53], [54]. Additionally, a good energy resolution allows systematic studies of
background processes especially in the main spectrometer, since all background
electrons created behind the analyzing plane reach the detector.
Hence, a 90 mm diameter silicon PIN diode with 148 pixels arranged in a
dartboard pattern is installed inside the second of two superconducting magnets
(see figure 2.10). The FPD is divided in 12 rings with twelve and the bullseye
with four pixels. All pixels have the same area. The magnetic field lines, on
which the electrons travel through the main spectrometer and the analyzing
plane, are mapped onto these pixels. Thereby, small inhomogeneities of the
retarding potential can be included in the analysis of the tritium spectrum.
These inhomogeneities are calculated with the KATRIN simulation software
KASSIOPEIA [55] and were also measured during the commissioning phase
of the main spectrometer with an angular-selective photo-electron source (see
section 4.5) [44, 56]. The typical energy resolution of one pixel is about 1.4 keV.
Finally, a post acceleration electrode is installed, which allows an acceleration of
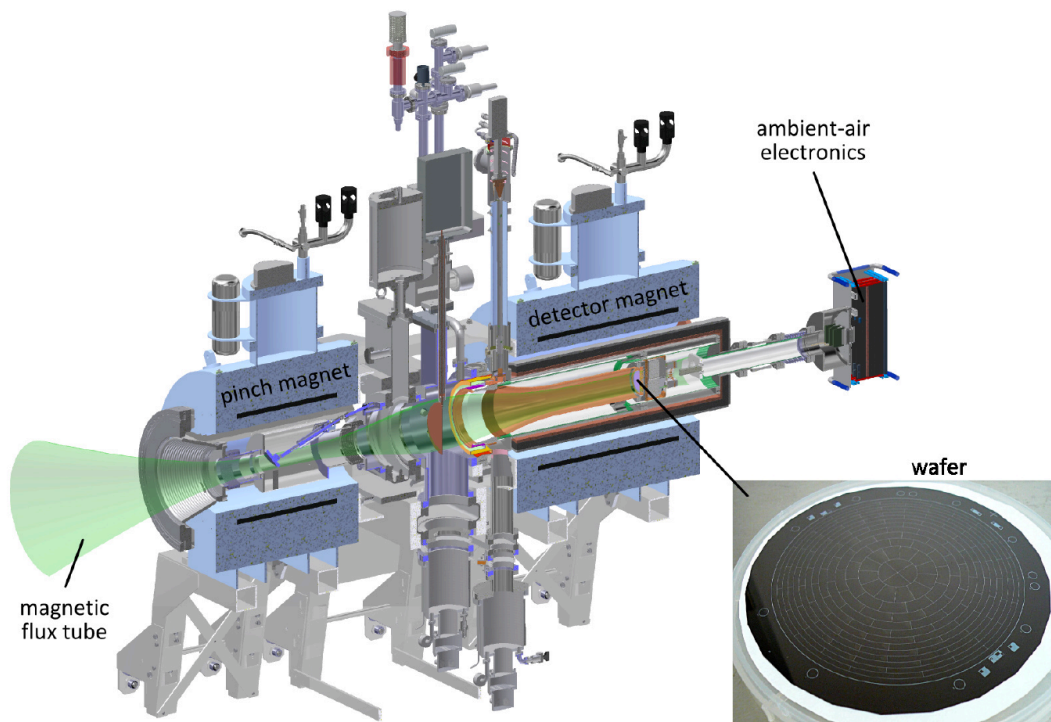the electrons up to 30 kV in order to improve the signal-to-noise ratio.

Figure 2.10: Focal plane detector located inside the detector magnet. Due to the pinch magnet, the field lines coming from the main spectrometer are collimated to an area of approximately $64\,\mathrm{cm}^2$. In the lower right part of the picture the silicon PIN diode wafer with 148 pixels arranged in 12 rings is shown. The image was taken from [57].

SYSTEMATIC UNCERTAINTIES AND ENERGY CALIBRATION AT KATRIN

The sensitivity for the neutrino mass measurement of KATRIN is limited by statistical and systematic uncertainties. The statistical uncertainty depends on the size of the analyzed measurement interval at the tritium β-decay endpoint $E_0 \approx 18.6\,\mathrm{keV}$ and the measurement time duration. For a data taking period of three years and an analysis interval of $[E_0 - 30\,\mathrm{eV} : E_0 + 5\,\mathrm{eV}]$, simulations and calculations ([28, 52]) showed, that a statistical uncertainty of

$$\sigma_{\mathrm{stat}} = 0.018\,\mathrm{eV}^2 \tag{3.1}$$

is expected. Accordingly, the systematic uncertainty has to be equal or smaller $(\sigma_{\mathrm{sys}} \leq \sigma_{\mathrm{stat}})$ in order to reach the best sensitivity for the neutrino mass measurement. The value in equation (3.1) is derived assuming a background rate of $10\,\mathrm{mHz}$. Although commissioning measurements of the main spectrometer showed that the actual background rate is in the order of a few $100\,\mathrm{mHz}$ [30, 37], the overall KATRIN sensitivity is still expected to fulfill the design goal of $0.2\,\mathrm{eV}$. In this chapter, the major sources for the systematic uncertainties are discussed briefly with a focus on the impact of the high-voltage contribution. As the retarding energy is one of the most important parameters of the measurement, the high voltage calibration with different techniques will be discussed subsequently. A detailed overview of the systematic and statistical uncertainties is given in [28].

3.1 Systematic uncertainties and requirements for the HV system

Since the statistical uncertainties are expected to be about $18\,\mathrm{meV}^2$, the systematic uncertainty is desired to be

$$\sigma_{\mathrm{sys}} \leq 0.017\,\mathrm{eV}^2. \tag{3.2}$$

In the evaluation of the systematics in the design phase of KATRIN, five major sources of uncertainties were identified. These contributions are discussed in the following.

Transmission and response function: The analytical transmission function of the main spectrometer describes the transmission probability for electrons coming from the source with a certain energy and starting angle (see section 2.2.1). It depends – among other things – on the magnetic and electric fields in the analyzing plane. Because of the large diameter of the main spectrometer of about $10\,\mathrm{m}$, inhomogeneities in the electric and magnetic fields are expected. Therefore, the transmission conditions for the electrons depend on their trajectory through the vessel. Since the FPD is divided and arranged in 148 pixels (see section 2.2.4), the influence of this effect can be reduced. In order to investigate the transmission function of the main spectrometer, commissioning measurements with an angular selective photo-electron source [56, 44] and a condensed krypton source (see section 3.2.2) were performed. In addition to the transmission properties of the main spectrometer, processes like inelastic scattering of the electrons on molecules in the WGTS have to be considered as well. The energy loss of inelastically scattered electrons is investigated with a mono-energetic photo-electron source installed at the rear wall of the WGTS [32]. The response function of the experiment (see figure 3.1) is given by the convolution of the transmission function and the energy loss function of electrons in the source [58].

Distribution of final states: The released energy of the tritium β-decay is not exclusively distributed between the electron and the antineutrino, but can also be stored in excited states of the daughter molecule $(^3\mathrm{HeT})^+$. Since the first electronic excitation state has an energy of about $27\,\mathrm{eV}$, it is not relevant in the analysis due to the high energy resolution of the main spectrometer and an appropriate interval for the energy analysis. However, rotational and vibrational excited states influence the shape of the spectrum at the endpoint region. In addition, also other molecules like TH and TD have to be taken into account in the analysis, contributing to the systematic uncertainties of the final state distribution [59].
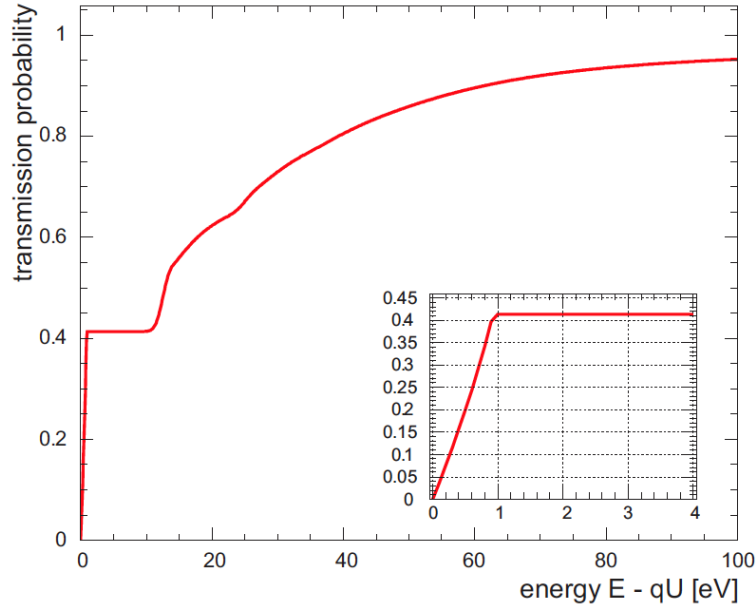
Figure 3.1: Response function for the KATRIN main spectrometer. The transmission probability for isotropically emitted electrons depends on the starting energy E and the retarding energy qU of the spectrometer. The resulting function is a convolution of the transmission function with the energy loss function of electrons in the WGTS. The zoomed picture shows the transmission function of unscattered electrons. The image was taken from [28].

Tritium column density in the WGTS: The column density of tritium in the WGTS determines the decay rate. In order to achieve high statistics, a large decay rate is desired. However, for a large decay rate the amount of tritium inside the WGTS and therefore the column density must be high. Since this is directly correlated with the probability of inelastic scattering for the decay electrons, these two aspects have to be balanced in order to get an optimal count rate for the FPD without loosing to many electrons in scattering processes. One critical parameter for the desired column density is its stability. Unknown fluctuations influence the analysis, yielding a wrong value of the neutrino mass. Since this is an important parameter, regular calibration measurements with the rear section are planned in order to monitor the column density [32]. Furthermore, a Beta Induced X-Ray Spectroscopy (BIXS) [31] method is used to monitor x-rays at the rear wall, providing information about the column density.

Effects from space charging due to ions in the WGTS: Due to the large amount of β-decays, positive and negative charged ions are produced in the WGTS. In addition to different endpoint energies, an accumulation of ions in a certain volume of the WGTS can create a space charge with time dependent electric fields, which influences the endpoint spectrum as well. Since only the endpoint energy of electrons originating from T^- is close to the neutral case

of T_2, the numerous other ions are not relevant regarding the neutrino mass analysis [28].

Uncertainties of the retarding HV: The energy analysis of the decay electrons is done at the main spectrometer with a retarding potential (see sections 2.2.1 and 2.2.2). Fluctuations of the potential difference between the WGTS and the main spectrometer have an influence on the spectrum and therefore need to be measured precisely. Since this parameter is of crucial importance for KATRIN, two independent measurement approaches are used in order to ensure system redundancy. Firstly, the retarding HV is measured directly with two custom-made ultra-precise HV dividers (see section 5.1). Secondly, the HV is compared to the natural standard of mono-energetic conversion electrons from the decay of Kr-83m (see section 3.2.2). Since the endpoint of the tritium-β-decay spectrum is a free fit parameter in the analysis, the absolute value of the HV is of minor importance. However, unknown fluctuations and shifts of the HV during tritium measurement phases would directly affect the neutrino mass analysis as a shift to lower masses.

Fragmented in these five contributions, the uncertainty budget for the single systematic uncertainties is limited to about

$$\sigma_{\text{sys,single}} = 0.0075\,\text{eV}^2. \tag{3.3}$$

Since the focus of this thesis lies on the precision HV system of KATRIN and the calibration of the HV, the last contribution to the systematic uncertainty budget is discussed to a greater extent in this section. Details about the technical aspects and the single components of the HV system are given in the next chapters.

First of all, in principle the general stability of the HV is of minor importance compared to the HV monitoring system. As long as the HV is measured with sufficient precision, longterm drifts or changes can be included in the analysis. However, short-term fluctuations with a frequency of 0.5 Hz or higher can not be measured with the HV dividers and therefore have to be suppressed (see section 4.2).

In order to derive the uncertainty budget for the HV measurement, the influence of a Gaussian fluctuation $f(x)$

$$f(x) = \frac{1}{\sigma\sqrt{2\pi}} e^{\frac{-(x-\mu)^2}{2\sigma^2}} \tag{3.4}$$

of the retarding potential is discussed in the following. Here, σ denotes the standard deviation and μ the expectation value of the Gaussian. This example is already discussed in [28] and [60] with more details.

As described in section 1.5, the spectrum of the β-decay electrons in the endpoint region can be described by

$$\frac{d\dot{N}}{dE} = a \cdot (E_0 - E)\sqrt{(E_0 - E)^2 - m_{\nu_e}^2 c^4} \tag{3.5}$$

with the constant factor a including all non-relevant terms for this example. Since the neutrino mass is small (less than $2\,\text{eV}$), the spectral shape can be approximated by a Taylor expansion around $m_{\nu_e}^2 = 0\,\text{eV}$:

$$\frac{d\dot{N}}{dE} = a \cdot (E_0 - E)^2 - a \cdot \frac{1}{2}m_{\nu_e}^2 + \mathcal{O}(m_{\nu_e}^4) + ... \qquad . \tag{3.6}$$

A convolution of the Gaussian fluctuation with $\mu = 0$ and the spectrum $g(E)$ with a vanishing neutrino mass

$$g(E) = \frac{d\dot{N}}{dE}(m_{\nu_e} = 0) = a \cdot (E_0 - E)^2 \tag{3.7}$$

leads to this expression:

$$f * g(E) = \int_{-\infty}^{\infty} f(x) \cdot g(E - x)dx = a \cdot (E_0 - E)^2 + a \cdot \sigma^2. \tag{3.8}$$

The comparison of equation (3.6) and equation (3.8) leads to

$$m_{\nu_e}^2 c^4 = -2\sigma^2, \tag{3.9}$$

neglecting higher orders of the Taylor expansion. With equation (3.3) and equation (3.9), the upper limit for the systematic uncertainty of the HV fluctuation contribution can then be derived as

$$\sigma \leq 0.06\,\text{eV}. \tag{3.10}$$

Since the tritium-β-decay spectrum endpoint is at around $18.6\,\text{keV}$, the relative uncertainty for the HV measurement has to be below $\frac{0.06\,\text{eV}}{18\,600\,\text{eV}} \approx 3\,\text{ppm}$. This holds for the longterm stability of a KATRIN measurement interval of typically 2 months as well as for short-term uncertainties in the order of seconds or minutes. The challenging short-term issue is discussed in section 4.2 and in more detail in [33]. This thesis focuses on the longterm HV monitoring and stabilization. In the next sections, two different and independent approaches for the calibration of the HV and the energy scale of KATRIN are discussed. In this context, calibrating the HV of KATRIN means the calibration and characterization of the precision HV dividers (see section 5.1), since they are used to measure the retarding potential of the main spectrometer.

At first, the calibration with the nuclear standard of mono-energetic Kr-83m conversion electrons is presented. Subsequently, electrical calibrations with the idea of the traceability to Josephson voltage standards [61] are discussed.

3.2 Calibration with Kr-83m

The nuclear isomer Kr-83m is used in different locations at the KATRIN experiment as mono-energetic electron source in order to test and calibrate the single

components and their overall interaction with the whole beam line. An extensive description of the different sources and their functionality for KATRIN is given in [62]. Before the different source types and their properties are described in section 3.2.2, the general principle of internal conversion and advantages of Kr-83m for KATRIN are discussed briefly in the next section.

3.2.1 Conversion electrons of Kr-83m

When an excited nucleus relaxes into its ground state, the energy difference of the two states can be released via different mechanisms. For energies in the keV range, electromagnetic decays are the ordinary decay channel. A typical example of this process is the emission of photons whose energy correspond to the difference between the two energy levels. When the emission of photons is suppressed due to electromagnetic transition rules, the de-excitation can occur via the emission of an electron from the atomic shell. This process is called internal conversion and the coefficient $\alpha_{\mathbf{IC}}$ is defined as the ratio of the emission rate of electrons $N_{\mathbf{e}}$ and photons N_γ:

$$\alpha_{\mathbf{IC}} = \frac{N_{\mathbf{e}}}{N_\gamma}. \tag{3.11}$$

It depends – among other things – on the multipolarity of the transition and the mass & charge of the decaying nucleus. Depending on the energy of the transition, electrons from different shells can be emitted. The energy distribution $E_{\mathbf{kin}}$ of the emitted electrons is discrete and depends on the energy of the transition E_γ and the atomic binding energy E_{bind}:

$$E_{\mathbf{kin}} = E_\gamma - E_{\mathrm{bind}} + E_{\mathrm{rec}}^\gamma - E_{\mathrm{rec}}^{\mathrm{ce}} + C. \tag{3.12}$$

Depending on the properties of the source (e.g. gaseous or condensed on a substrate), additional correction terms C (work function differences, image charges etc.) occur. Finally, the nuclear recoil energies E_{rec} for the γ and for the conversion electrons have to be considered.
The natural line width Γ of the internal conversion process depends according to the uncertainty relation on the lifetimes of the nuclear transition and the electron vacancy. The integral shape of the conversion electron line can be described by a Lorentz distribution L in the non-relativistic case as

$$L = A \cdot \frac{\Gamma/2}{(E - E_0)^2 + (\Gamma/2)^2} \tag{3.13}$$

with the amplitude A, energy E, and the central line position E_0.
For different applications regarding energy and HV calibration at KATRIN, conversion electron sources are ideal. The most important aspects in this case are the well-known electron energies and sharp line widths in the eV range. Additionally, the half-life is desired to be short enough to provide a sufficiently
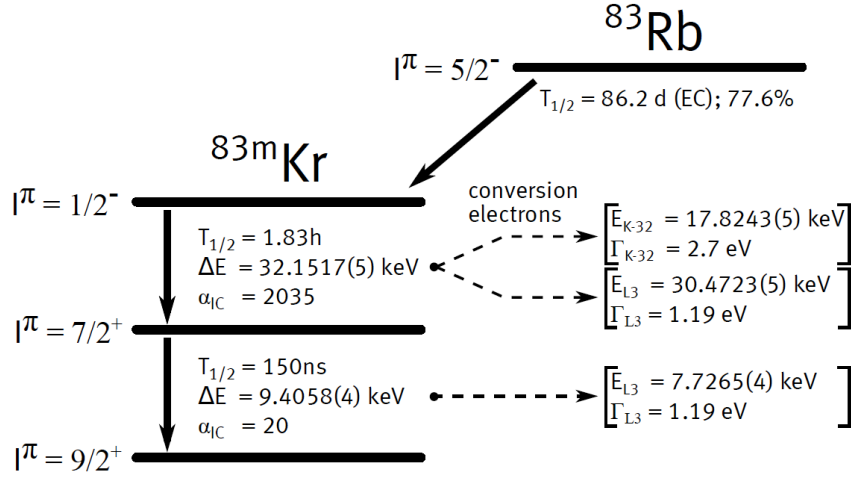
Figure 3.2: Decay scheme of Kr-83m. The mother isotope Rb-83 decays via electron capture to the excited state Kr-83m. Subsequently, two cascaded gamma transitions, which are highly converted into emitting conversion electrons, follow as the isotope decays into the ground state. Depending on the originating shell of the emitted electrons, multiple conversion electron lines with different kinetic energies are possible. The image was taken from [36].

high source activity and prevent a longterm contamination of the system during normal tritium measurement phases. The nuclear isomer Kr-83m fulfills all these requirements, as it provides multiple conversion electron lines in the desired energy range with narrow line widths and sufficiently low half-lives.

The decay scheme of Kr-83m is shown in figure 3.2. It features two cascaded gamma transitions with energies of about $E_{32} = 32\,\text{keV}$ and $E_{9.4} = 9.4\,\text{keV}$, which are highly converted due to the emission of conversion electrons. Featuring a half-life of $1.83\,\text{h}$ for the $32\,\text{keV}$ transition, this isotopes is perfectly applicable for short-term calibration measurements at KATRIN. The mother isotope Rb-83 decays with a probability of $77.6\,\%$ via an electron capture to Kr-83m with a half-life of $86.2\,\text{day}$. The energy range of measurable conversion electrons stretches from about $7\,\text{keV}$ up to $32\,\text{keV}$, depending on the originating shell of the emitted electrons. With kinetic energies of about $17.8\,\text{keV}$ the K-32 line is the closest conversion electron line compared to the tritium endpoint energy. The difference of $800\,\text{eV}$ is small enough so that the electrons can be accelerated with commercial HV supplies with high precision in order to compare the endpoint energy to the K-32 line.

An extensive overview of all conversion electron lines, their intensity, energy and additional information can be found in [63]. The three most important conversion electron lines of Kr-83m for the HV calibration at KATRIN are shown in table 3.1. In combination with the K-32 line, the L_3-32 line can be used to calibrate the HV and the energy scale of KATRIN. The conversion electrons of these two lines originate from the same nuclear transition and only differ in their atomic binding energies, which can be measured by gamma-spectroscopic

Table 3.1: Important conversion electron lines of Kr-83m for the HV calibration at KATRIN. The K-32 line with a kinetic electron energy of about 17.8 keV is highly relevant for calibration purposes since it is close to the tritium endpoint. In combination with the L_3-32 line, additionally systematic effects can be investigated. Finally, the L_3-9.4 line can be used to study linearity effects especially together with the L_3-32 line. The numbers taken from [63].

Line	Kinetic energy (eV)	Width (eV)	Intensity per decay (%)
L_3-9.4	7726.44(60)	1.58(16)	5.72(27)
K-32	17824.23(50)	2.70(6)	24.8(5)
L_3-32	30472.19(50)	1.108(13)	37.8(10)

measurements with high precision. This was investigated firstly with a condensed krypton source (see next section) in [60] and allows ppm-precise calibrations of the KATRIN HV dividers (see chapter 6 for more details). In order to determine the linearity of the system, the L_3-9.4 line can be used. In that case, the binding energy for electrons originating from the L-shell is the same, whereas the energy of the gamma transition differs. Therefore, effects that are independent of the binding energy, can be examined [50].

3.2.2 Kr-83m at KATRIN

Due to its versatile application area and advantages for KATRIN, multiple sources of Kr-83m in different configurations and locations are used across the experimental setup. The positions of three sources used at KATRIN are shown in figure 3.3. This section gives a brief overview of the different sources regarding their properties and advantages. An extensive description and (first) measurements are presented in [48, 62, 64].
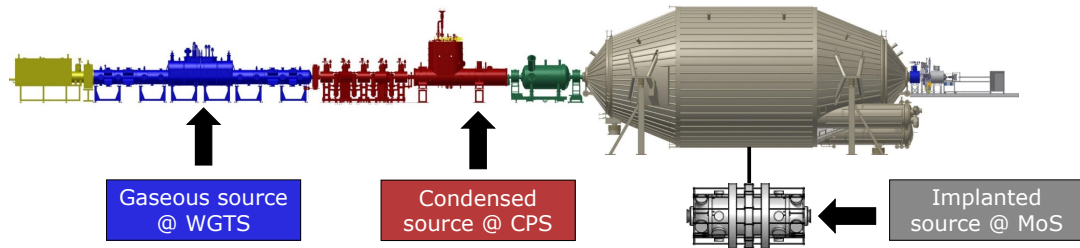

Figure 3.3: Overview of the KATRIN beam line and the positions of the three different Kr-83m calibration sources.

Implanted source at the monitor spectrometer (SKrS): The former spectrometer of the Mainz neutrino mass experiment is used at KATRIN as a monitoring spectrometer (see section 2.2.3). Here, an implanted solid state source for the HV calibration is installed, which allows the monitoring of line positions in parallel to the normal KATRIN tritium operation. Because of its short half life of 1.83 h, Kr-83m can not be implanted directly into a solid state body. Hence, the mother isotope ^{83}Rb with a half life of 86.2 days is used as a generator for Kr-83m in terms of an implanted source. First and extensive studies with this system were performed in the last years and are presented in [50, 36, 51]. The production methodology of these sources (e.g. the implantation energy of the Rb into the solid) and different source materials were tested in [49].

The main advantage of this source is the possibility of an online monitoring, since – in contrast to the other two sources – it can be operated in parallel to normal tritium runs at KATRIN. Furthermore, the comparably simple operation of this kind of source is advantageous: it does not require cryogenic temperatures and is robust against a change of vacuum conditions.

On the other hand, it is not part of the KATRIN beam line. Therefore, it is not sensitive to effects only influencing the beam line, e.g. changes in the work function of the main spectrometer. Since the conversion electrons lose energy when they leave the solid body, e.g. due to inelastic scattering or an imprecisely known work function of the source material, the line position determined with the monitor spectrometer can not be used for an absolute calibration of the HV. However, when the environmental conditions are constant, relative changes on ppm-level can be monitored in order to detect possible shifts and changes of the HV system and the retarding potential of the MS.

Condensed source installed at the CPS (CKrS): At the end of the CPS, directly in front of the pre-spectrometer, the condensed Kr-83m source (CKrS) is installed. A detailed description of the setup and the commissioning of the system in 2017 is given in [37]. Kr-83m is frozen onto a HOPG substrate at cryogenic temperatures of about 25 K. During the normal KATRIN operation, the substrate is located in a vacuum chamber connected to the CPS. For calibration measurements it can be moved into the beam tube by a movable mounting structure. A parallel operation to the standard tritium measurements is not possible.

The quadratic substrate itself has small dimensions of 20 mm×20 mm compared to the circumference of the beam line, allowing a scan of arbitrary areas of the flux tube corresponding to different pixels of the FPD. The main advantage of this source is that transmission properties of the main spectrometer can be investigated directly, because it is located in the KATRIN beam line.

Since the kinetic energy of the emitted conversion electrons of this source highly depends on the surrounding vacuum conditions and cleanliness of the substrate, these parameters have to be monitored precisely. The film thickness of the

frozen Kr-83m is measured with precision laser ellipsometry [65, 36, 37, 66]. Another advantage of this kind of source compared to the implanted one is that the process of film preparations for (sub-)mono-layers of Kr-83m is highly reproducible, providing the possibility of stable and reproducible measurements of the line positions.

On the other hand, the energy loss of the electrons when they leave the substrate is not known precisely. Furthermore, their absolute kinetic energy is influenced by image charge effects (see [60]). Hence, an absolute calibration of the HV with this system is also not possible with the required level of precision of 3 ppm. However, by measuring different conversion electron lines, the linearity of the HV system can be investigated. This was performed firstly in [60] using the M_1-9.4, K-32 and L_3-32 lines with the CKrS in an earlier stage at the setup of the Mainz neutrino mass experiment. The sensitivity of these measurements was limited to the 100 meV level. A similar idea of the HV calibration by measuring different conversion electrons lines with the gaseous source (see next paragraph) was developed within this thesis and is discussed in chapter 6.

During the commissioning phase of this source in Juli 2017, among other things multiple test measurements with different configurations of the HV system were performed within this work. An overview of these measurements is given in section 6.5.

Gaseous source in the WGTS (GKrS):   The WGTS is designed in order to provide the tritium for KATRIN. However, instead also gaseous Kr-83m can be injected into the system for calibration measurements. Details about the setup are discussed in [51].

Since the freeze-out temperature of krypton is much higher compared to tritium (about 100 K at pressures below 100 mbar [67]), the WGTS has to be warmed up for this operation mode. In addition to this requirement, also multiple other working parameters of the WGTS are different, depending on the gas filling of the system. This means, that the operation of the gaseous Kr-83m source in parallel to the tritium measurements is not possible at 30 K. Therefore, it is required to operate the WGTS at temperatures above 100 K in order to allow combined measurements of Kr-83m and tritium. However, KATRIN schedules maintenance breaks after a measurement phase every 2 months, offering the possibility for calibration measurements with the system.

The main advantage of this source compared to the other two ones is that no surface effects or energy losses in a solid body influence the kinetic energy of the electrons. Although inelastic scattering with krypton atoms is possible, the probability is comparably small because of the low column density and gas pressure of krypton inside the WGTS. Hence, the kinetic energy of the electrons is described by equation (3.12) without further corrections.

One main topic of this thesis is the absolute calibration of the HV system with Kr-83m conversion electrons. Up to now, only the gaseous source provides the possibility to calibrate the HV dividers, which are used to measure the retarding

potential with the required precision on the ppm-level. In chapter 6, the newly developed calibration method using the GKrS and measurements which were performed within this work are discussed in detail.

3.3 Electrical calibration

A different and independent approach in order to calibrate the HV system at KATRIN is given by electrical calibrations. Since the HV of the MS is measured with high-voltage dividers, the calibration of their scale factors has to be performed regularly. This is generally done by connecting the HV divider to a well known HV source U_{input} and measuring the output voltage U_{output}, since the scale factor is defined as ratio of U_{input} and U_{output} (see section 5.1). In order to calibrate a HV divider to the ppm-level, both voltages have to be determined with this level of precision.

For U_{input}, which is usually in the range of kV and higher, this poses a problem: to measure such high voltages with ppm-precision, HV dividers are needed, scaling down the voltage into the optimal working range of digital voltmeters (DVMs) below 20 V. This means, that reference HV dividers with well-known scale factors have to be used, in order to calibrate the KATRIN dividers with the required precision. Section 5.3 gives an overview of standard calibration measurements using reference dividers, which were performed over the last years. In contrast to the calibration possibilities of nuclear standards with energies in the keV range discussed in the previous section, the traceability problem of high voltages arises from the limited magnitude of voltage standards, which are usually in the range of 10 V or below. A detailed discussion of this challenge is presented in this section.

In metrology, the measurement of each physical quantity is traced back to its corresponding primary SI standard (see figure 3.4). Metrology laboratories like Physikalisch-Technische Bundesanstalt (PTB) or National Institute of Standards and Technology (NIST) are responsible for providing secondary and/ or working standards (and nowadays in some cases also primary standards), which are calibrated with reference to a primary standard. In the right part of figure 3.4, the calibration chain for voltage measurements at KATRIN is shown. The standard known with highest precision is given by the Josephson effect [68], a quantum mechanical phenomenon, where small voltages in the (sub)mV range can be created with relative uncertainties in the order of $\leq 10^{-10}$. By connecting thousands of so-called Josephson Junctions, DC voltages of about 10 V can be generated, forming a Josephson voltage standard [61].

The next step are commercially available solid-state Zener reference standards (e.g. Fluke 732A(B) used at KATRIN), which provide a longterm stability of their generated 10 V output voltage on the sub-ppm level over several years. As the manufacturer specifies the uncertainty rather conservative with 6 ppm
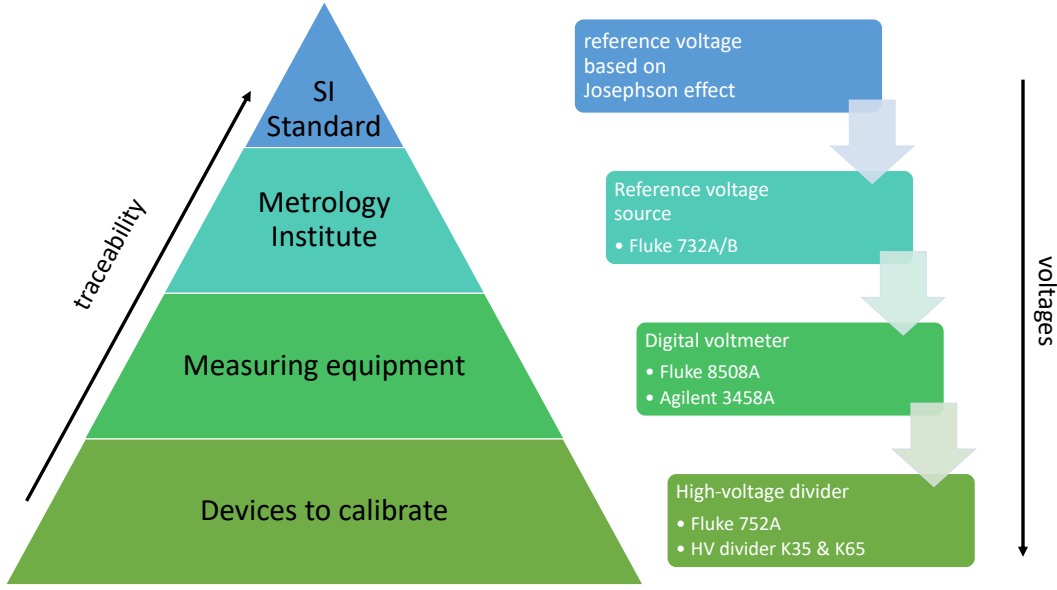
Figure 3.4: The principle of traceability. Left: the SI standard of a physical quantity is handled by metrology institutes, which calibrate (commercial) reference sources. With these, measuring equipment and calibration devices can be calibrated. For each step in the calibration chain additional uncertainties arise. The right side shows the exemplary chain for the HV equipment used at KATRIN. The SI standard is the reference voltage based on the Josephson effect (usually in the range of $1\,\mathrm{V}$ to $10\,\mathrm{V}$), which is used at the PTB in order to calibrate primary voltage standards like $10\,\mathrm{V}$ reference sources. With these devices, precision DVMs can be calibrated in their most precise range of up to $20\,\mathrm{V}$. With the precision DVMs, secondary devices, that are directly connected to HV (like HV dividers) can be calibrated. For each step in this chain, higher voltages can be reached.

for $1\,\mathrm{year}$ [69], an investigation regarding the longterm stability was performed in the context of this thesis. For this purpose, calibration measurements of a Fluke 732A reference voltage source over the last years performed by PTB were analyzed. The German national metrology institute provides the service to calibrate commercial voltage standards with reference to the Josephson standard. Figure 3.5 shows the determined values since the first calibration in 2005. Assuming a time (t) dependent drift d, the data was fitted with MINUIT [70] by

$$f(t) = U_0 + d \cdot t \tag{3.14}$$

via χ^2 minimization. Here, the quadratic sum

$$\chi^2 = \sum_i \frac{(y_i - f_{\mathrm{model}})^2}{\Delta y_i^2} \tag{3.15}$$

of deviations between the data points y_i and the fit model f_{model} normalized to the uncertainties Δy_i is minimized. In this context, the so-called *reduced* $\chi^2 := \chi^2_{\mathrm{red}}$

defined as

$$\chi^2_{\text{red}} = \frac{\chi^2}{Ndof} \tag{3.16}$$

is a valuable indicator, if the (fit) model describes the data well ($\chi^2_{\text{red}} \approx 1$). Here, the parameter $Ndof$ describes the number of degrees of freedom

$$ndof = n_{\text{data}} - n_{\text{fitpar}} \tag{3.17}$$

with the number of data points n_{data} and the number of fit parameters n_{fitpar}. In their calibration report, the PTB specifies the standard deviation of the device during the measurement and a one year transfer uncertainty of usually 2 ppm, which is not based on the measurements. Therefore, the standard deviation – typically below 1 µV (0.1 ppm) – was used as uncertainty for every data point in figure 3.5. This yielded a reduced χ^2 of $\chi^2_{\text{red}} = 23.6/3 = 7.9$, indicating that the assumed uncertainties are to small. Hence, the uncertainties were scaled with $\sqrt{\chi^2_{\text{red}}}$, such that the quadratic deviation per number degrees of freedom is equal to one. The resulting uncertainties of about 0.28 ppm for each calibration are shown in the plot. The fit yields a drift of 0.31(4) ppm year^{-1}, demonstrating, that the stability of the devices can be assumed to be more than an order of magnitude better than specified by the manufacturer. At KATRIN, a total number of eight commercial reference sources (4×Fluke 732A and 4×Fluke 732B) are used, which allows crosscheck measurements and ensures system redundancy and security.

With these 10 V sources precision digital voltmeters can be calibrated, which are used to measure voltages up to 20 V directly to the (sub)ppm-level. The manufacturer specifications for the uncertainties of the DVMs are also assumed to be rather conservative, since they have to cover the usage in standard laboratory environments, where no reference voltage sources are available. This was investigated similarly to the previously discussed analysis.
At KATRIN, three different DVMs are used for precision measurements: Fluke 8508A, Agilent 3458A and Keysight 3458A. In order to determine their 24 h uncertainty, the devices were connected a Fluke 732A 10 V reference source, measuring the output voltage continuously over about 20 days. The measurements were divided into 24 h bins and for each day the standard deviation σ_i was calculated. Finally, the average of σ_i over the whole measurement time was determined, yielding $\overline{\sigma}$ as relative uncertainty of about 0.1 ppm (Fluke) and 0.2 ppm (Agilent & Keysight)[1]. Unless otherwise stated, these values are assumed for DVM uncertainties in the remaining part of this thesis.
With calibrated DVMs, in the next step the HV dividers can be calibrated, which is discussed in detail in section 5.3. With this traceable calibration chain, absolute calibration measurements of the HV dividers on the ppm-level could be demonstrated over the last years. In the last step, HV dividers are used to calibrate the energy scale of KATRIN by measuring the retarding potential of

---

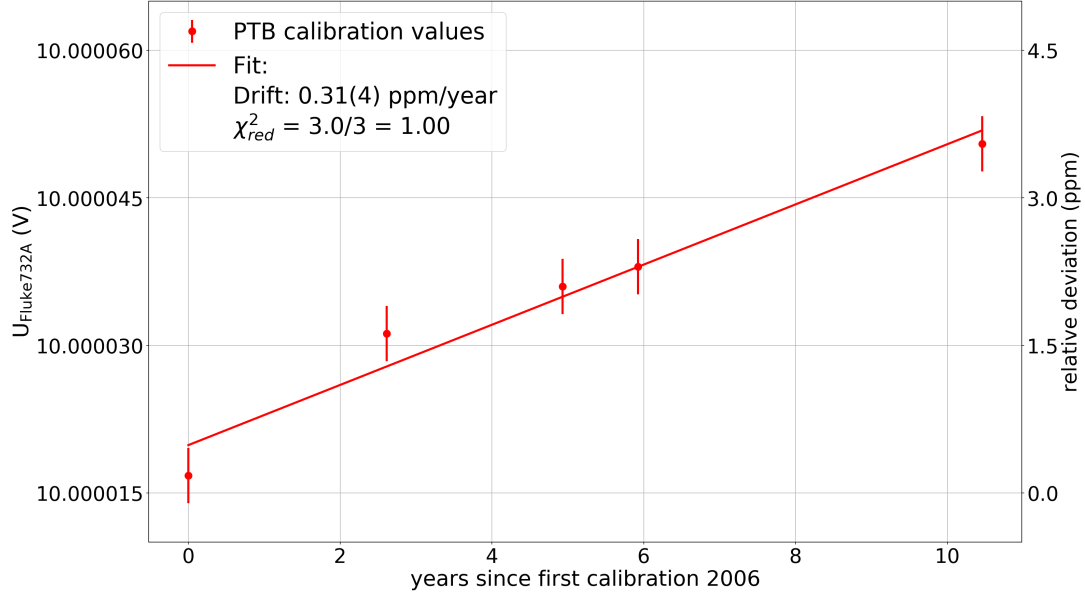[1]These values are valid for measurements <20 V at $2 \cdot \sigma$.

Figure 3.5: Calibration values of a KATRIN voltage source (Fluke 732A) obtained by PTB measurements over the last years. The uncertainties of the single calibration values are scaled such that $\chi^2_{\mathrm{red}} = 1$ (see text).

the main spectrometer.

In order to monitor the longterm behavior and to ensure the functionality of the HV monitoring system, regular calibration measurements of the mentioned devices were performed in the past and have to be continued in the future as presented in the following paragraphs.

The 10 V reference sources have to be calibrated at a metrology institute like PTB annually. The procedure to calibrate the DVMs is easy to handle and can be performed on site on a daily or weekly basis. Here, the devices have to be connected to a calibrated 10 V reference source and a correction factor accounting for the linearity of the device has to be determined, which is then stored in the KATRIN calibration database [52].

The HV dividers showed sub-ppm-stability over the last years [71, 72]. However, at least a monthly calibration of the devices is recommended in order to monitor the integrity and stability of the scale factors.

Although the calibration measurements presented in section 5.3 indicate that the KATRIN HV dividers fulfill the requirements regarding the uncertainty of the HV measurement, a method completely traceable over the whole voltage range of the dividers to 10 V standards without assumptions was not possible with these methods. The main problem in this case is the voltage dependency of HV dividers, which was neglected since commercial reference dividers are only available up to voltages of 1 kV.

In the context of this thesis, a novel absolute calibration method with ppm-precision was developed, which overcomes these problems. A detailed discussion of this method is given in chapter 5.

Compared to the calibration methods with the different Kr-83m sources described in the previous section, the electrical calibration has multiple advantages. For the absolute calibration of the HV dividers the only competitive Kr-83m source is the gaseous one. Here, uncertainties of about 5 ppm stand in contrast to 1 ppm for the electrical calibration. However, relative long-term drifts can be measured with the monitor spectrometer with ppm-precision [48].

Another major advantage is, that the electrical calibrations can be performed independently during the tritium measurements, since two redundant HV dividers are available at KATRIN. While one is calibrated, the other one can be used to measure the retarding potential and vice versa.

However, both approaches for the HV calibration are important for KATRIN, as they are used to crosscheck each other and guarantee system redundancy.

SETUP AND PERFORMANCE OF THE KATRIN HV SYSTEM

At KATRIN, many parts of the experimental setup require high voltage. In the first instance, the retarding potentials for all three spectrometers have to be created, maintained and monitored, in some extent with ppm-precision. Especially the main spectrometer poses a challenge, since it is operated at $-18.6\,\mathrm{kV}$ and used to scan the tritium spectrum endpoint region. As described in section 2.2.2, a complex wire electrode system with up to 44 individual potentials has to be handled. Also other experimental components work with HV, as shown in table 4.1.

These high voltages have different requirements regarding absolute values, stability and high-frequent noise. In addition to the creation and distribution, the HV also has to be measured with ppm-precision in many cases. The direct measurement is done with two custom-made ultra-precise high-voltage dividers, which are discussed in more detail in the next chapter. Additionally, the monitor spectrometer is used as a redundant monitoring system.

In this chapter, the HV system of KATRIN is described with a focus on the complex parts of the spectrometer section. Since an extensive overview of the whole system and details about single components are given in [60, 73, 36, 47, 33], in this work only the basics of the setup and the contributions in the context of this thesis are discussed. Furthermore, during a commissioning phase early 2017, important performance test measurements could be carried out at the main spectrometer. The results and analyses of this campaign are presented in the next sections.

Table 4.1: Overview of high voltages used at KATRIN. For different components of the experimental setup, individual high voltages with corresponding requirements are needed. The most critical parameter is the retarding potential applied to the main and monitor spectrometer, which has to be stabilized on the 20 mV level, especially regarding high-frequent (HF) noise. The rear section features an electron source, which also requires precision HV. It can be operated in standalone mode and coupled to the main spectrometer HV (like the MoS). The HV stability for the PS and the FPD are uncritical. The CKrS can be operated on HV, which requires also a precision on the 20 mV level. However, since here required absolute voltage are limited to 1 kV, only a relative precision on the 10^{-5} scale is required. This is possible with commercial devices.

Parameter	RS	CKrS	PS	MS and MoS	FPD
Voltage	-35 kV	$\pm$ 1 kV	-35 kV	-35 kV	25 kV
Stability	$\pm$ 20 mV	$\pm$ 20 mV	uncritical	$\pm$ 20 mV	uncritical
HF noise	compensated	uncritical	uncritical	compensated	uncritical

4.1 Main spectrometer

As explained in section 3.1, the retarding potential of the main spectrometer is a crucial parameter for the measurement of the neutrino mass. Before the electrical setup is discussed, a brief overview of the mechanical setup is presented in the next section in order to motivate the requirements and complexity of the system.

4.1.1 Wire electrode system

The retarding potential of the main spectrometer is created by applying high voltage to the spectrometer vessel. In order to fine tune the shape of the electrical field inside, the inner surface of the main spectrometer is covered with an electrically isolated two layer wire electrode system (IE). This feature is also an effective countermeasure against electrons coming from the vessel walls - e.g. created by cosmic muons - which would create background at the FPD. This process is shown schematically in figure 4.1 a).

Details about the setup are given in [74] and measurements regarding the background reduction in the one- and two-wire-layer mode are presented in [37]. Figure 4.1 b) shows a 3D model of a single module of the overall 248 segments, which are installed inside the MS. They are arranged in 15 rings (ring 2 - 16), departed into two dipole halves. Individual potentials can be applied to each ring, half and layer. The central part of the MS consists of five rings (ring 7 - 11), which are connected intentionally in order to guarantee a homogeneous electrical field in the analyzing plane. The complete system is designed in order to be operated with up to 44 different voltages.
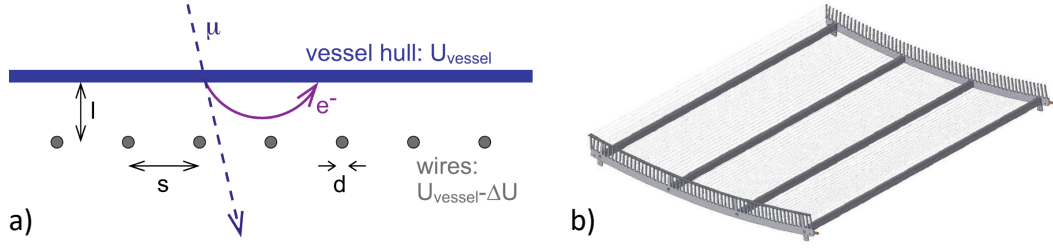
Figure 4.1: Wire electrode of the main spectrometer. a) Functional principle of the system for the one wire layer case. Free electrons created by cosmic muons hitting the vessel, are reflected due to a negative potential applied to the wires with the distance l to the wall. Each wire has a diameter d and distance s to its neighbour. b) CAD-drawing of a single module of the wire electrode system. The two layers are electrically isolated and can be operated on different potentials. Images taken from [37] (a) and [75] (b).

However, caused by several baking processes of the main spectrometer, some parts of the wire electrode system are short circuited, impairing its functionality as shown in figure 4.2. These short circuits only affect wire layers of one single ring, meaning that all 11 rings (counting the central segment as one part) on both dipole halves can be operated individually, but the two layer mode is not possible for all rings. For example, the central rings 7 to 11 of the east side of the MS are short circuited regarding inner and outer wire layer, which means that only a single potential can be applied. The influence of this impairment for KATRIN is investigated and discussed in [37].

For this designed setup of the wire electrode, the HV system requires up to 44 different created voltages additionally to the HV of the MS vessel itself. Since the wire electrode is important for the creation of a homogeneous retarding potential, its integrity is of crucial importance. In [47], a monitoring system based on capacitance measurements was developed and tested. Additionally, an angular selective photo-electron source, which was connected to the main spectrometer during commissioning measurements (see section 4.5), was used in order to check the integrity of the system in 2014.
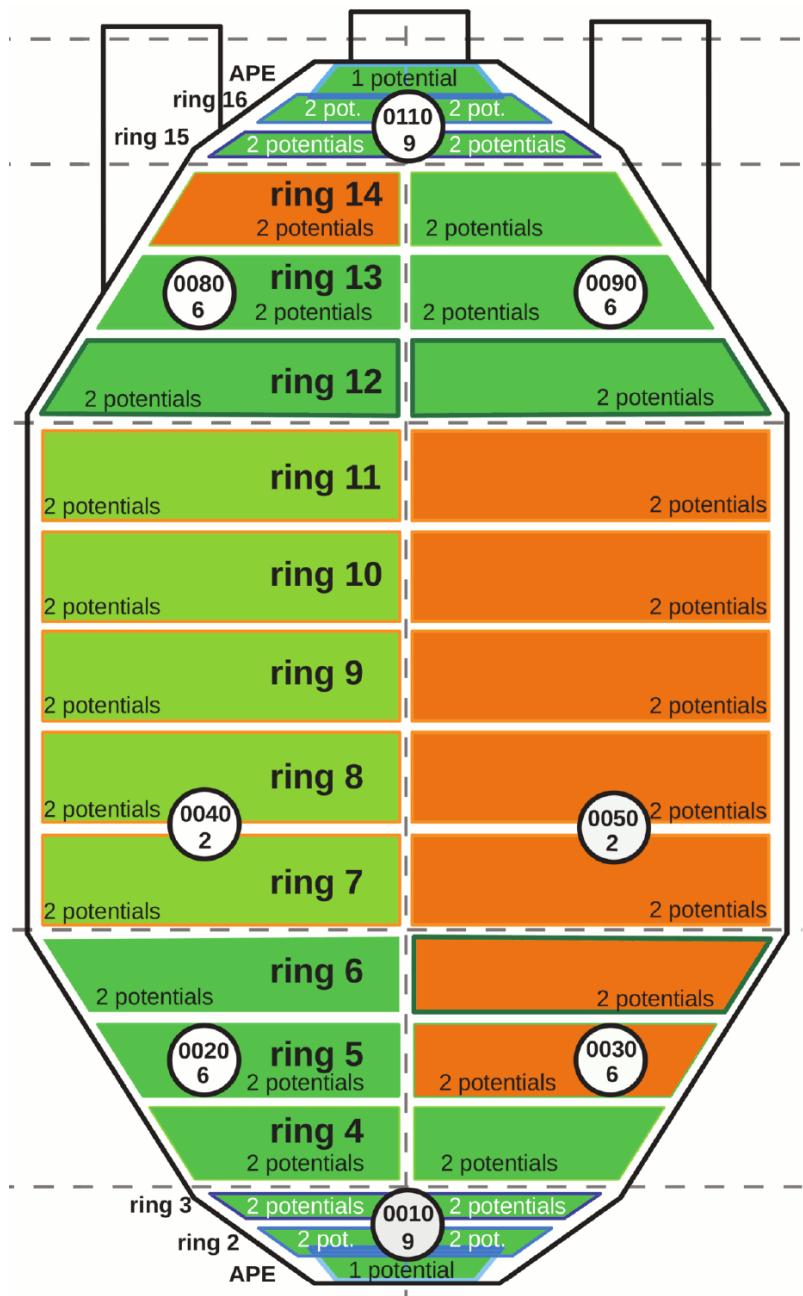
Figure 4.2: Overview of the electrical potentials which can be applied to the wire electrode system of the MS. In this view, at the top side of the spectrometer (north) the FPD is following. Overall 15 rings, departed into two dipole halves and two wire layers are available. The rings of the central part (7 to 11) are connected intentionally. Because of damages to the system due to baking processes of the MS [37], some wire layers are short circuited and can not be operated individually anymore. The affected rings are marked in orange. The image was taken from [37].

4.1.2 HV distribution

The KATRIN HV system consists of several voltage supplies and DVMs in order to create and measure the retarding potential of the main spectrometer (see figure 4.3):

- **The main HV supply** creates the basic voltage of $-18.4\,\text{kV}$ (up to $-35\,\text{kV}$) which is connected to the vessel of the MS and serves as the reference potential of the HV distribution rack, where all other power supplies are located. Multiple devices are available at KATRIN for this task. In order to reduce high-frequent (HF) noise and AC fluctuations of the HV, an active post regulation system is used (see section 4.2).

- **The IE common HV supply** creates a negative offset of usually $-200\,\text{V}$ (max. $-2\,\text{kV}$) for the whole wire electrode, resulting in an absolute retarding potential of $-18.6\,\text{kV}$. Since the analyzing plane (see section 2.2.1) is created by the most negative potential in the center of the MS, the inner wire layer of the central part of the IE system is hardwired to this potential.

- **Two dipole supplies** in combination with a relay create a fast switching ($\mathcal{O}(ms)$) dipole voltage of up to $-1\,\text{kV}$ for one side of the wire electrode (east and/or west). This feature can be used in order to reduce background caused by magnetically trapped charged particles in the MS, which are removed from the system with an $E \times B$ drift. The HV supplies are disabled in the standard measurement mode (e.g. during single runs of tritium measurements) and can be activated in between runs in order to remove stored particles.

- **Multiple offset supplies** create a positive voltage up to $500\,\text{V}$ on top of the IE common potential for single channels of the wire electrode system. The configuration can be arranged by the so-called patch panels. Each of this matrices with 23 rows and columns (one for the east and one for the west dipole) connects the 22 offset supplies with the 22 isolated parts of the wire electrode (see previous section). By this arrangement, all elements of the IE can be operated on individual or common potentials and any arbitrary configuration.

In principle, the system merely requires a ppm-precise monitoring of the high voltage. However, in order to simplify the analysis and for practical reasons it is also desired, that the set points and absolute values of the applied HV can be provided with ppm-precision. For the IE common and offset supplies, this does not pose a problem since the absolute values of the HV are in the $1\,\text{kV}$ range or below. Such devices with uncertainties in the $10\,\text{mV}$ range or better are commercially available. For the main HV supply this requirement is challenging, since the absolute value is much higher. A custom product fulfilling these specifications was developed by the manufacturer FuG (HCP 70M-35000), which can create voltages up to $-35\,\text{kV}$ with a stability of $2\,\text{ppm}$ over $8\,\text{h}$ [76].
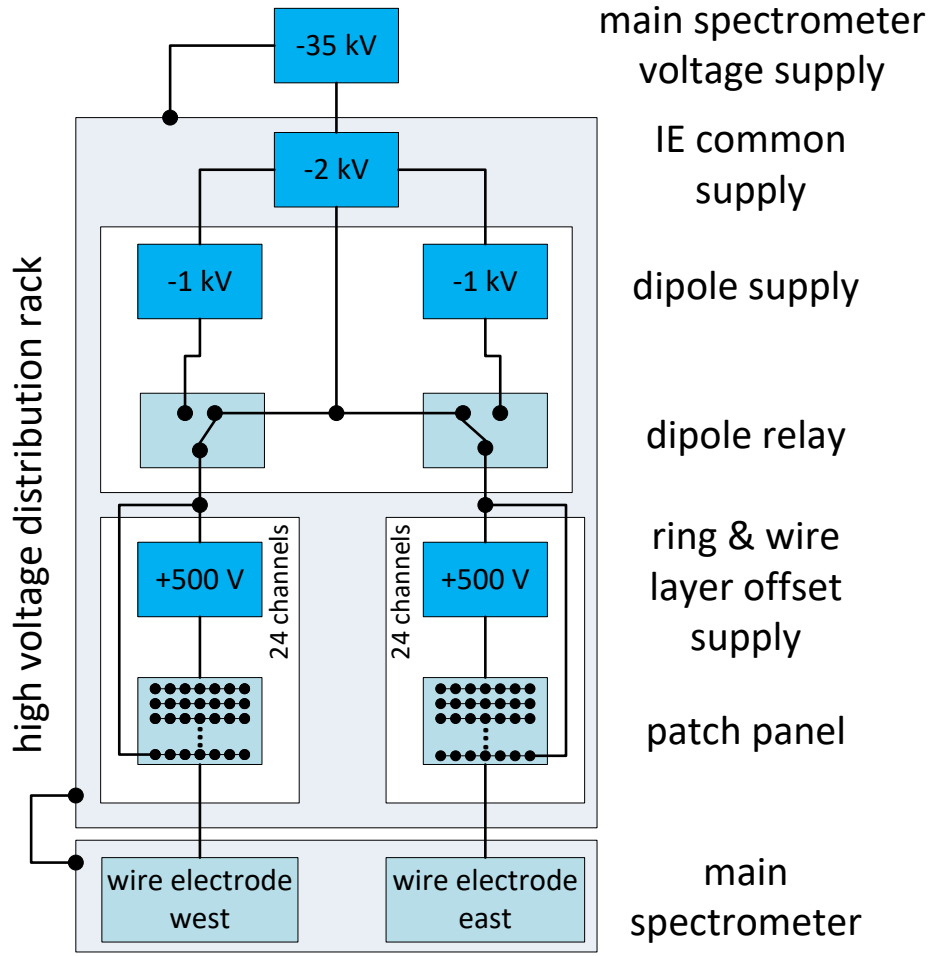
Figure 4.3: Simplified schematic overview of the HV system of the MS. The main HV supply creates a voltage up to $-35\,\text{kV}$, which is distributed to the main spectrometer vessel and the HV distribution rack. Here, an additional common IE HV supply is used in order to create a negative offset potential for the wire electrode. With dipole supplies and relays, each part of the IE dipole (east and west) can be loaded with fast switching negative voltages in order to remove stored charged particles. For the 22 isolated elements of the IE of each dipole additionally 24 channels of positive offset supplies are available. The distribution is done with the patch panel. The IE common HV is also connected to the patch panel in order to allow a direct connection of the wire electrode to this potential.

However, when the post regulation system is running, the stability of the used HV supply is not important, since the HV is regulated by an active control circuit (see section 4.2).

For the analysis of tritium measurement runs, the most important value is the potential in the analyzing plane, which is created by the main HV supply and IE common. Hence, this combined potential is measured with the precision HV dividers (K35 and K65, see section 5.3) and DVMs via a direct connection.

Additionally, this potential is distributed to the MoS, which runs in parallel to the tritium measurements with a Kr-83m source in order to monitor the HV. The basic system was tested successfully in commissioning phases of the spectrometer detector section [77] and during the first light measurement campaign [62]. Since precision HV was not required during these measurements, the standard voltage measurement was done via the internal readout of the HV supplies. In the context of this thesis, for the first time precision measurements on a large scale were performed, investigating the performance and stability of the precision HV system. The performed measurements and their results are presented in the next sections.

4.1.3 Stability measurement

During a HV commissioning phase in April 2017, measurements were performed in order to test the capabilities of the precision HV system at KATRIN. Although the single components (e.g. the HV dividers) were tested and calibrated regularly over the last years, this was the first time the complex system was operated with dedicated measurement time with respect to precision HV comparably to tritium measurements. As part of the commissioning of the whole HV system, an important investigation was the test of the longterm stability. During previous commissioning phases, only stability measurements with short time intervals in the order of minutes were performed [33].
The setup of the first longterm precision measurements was:

- the **precision HV supply** FuG HCP 70M-35000 was connected to the main spectrometer, creating a HV of $U_{\mathrm{MS}} = -18.6\,\mathrm{kV}$

- the IE common and offset HV supplies were short circuited during the measurements in order to investigate the performance of the main HV supply

- the post regulation system was not active (see next section)

- the K35 and the MoS were connected to the MS.

With this configuration, the stability of the HV was measured with a DVM U_{DVM} connected to the K35 over 15 h. Figure 4.4 shows the calculated absolute voltage

$$U_{\mathrm{MS}} = M_{\mathrm{K35}} \cdot U_{\mathrm{DVM}}, \tag{4.1}$$

assuming a scale factor of $M_{\mathrm{K35}} = 1972.4531$. This was determined at the last calibration of the HV divider in 2013 at PTB [47]. Over the whole measurement time, the system shows constant drifts on the ppm-level in the order of hours. Over the first 8 h, a constant drift of 2 ppm can be observed in agreement with the manufacturer information regarding the stability of the HV supply. The short-term stability of the system is shown in the enlarged view of figure 4.4. Here, a time scale of only about 12 min is investigated extracted from the longterm
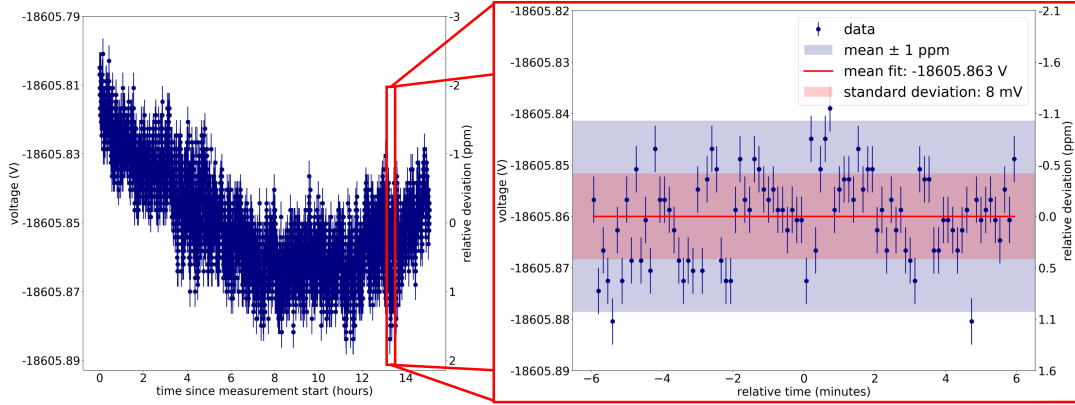
Figure 4.4: Longterm stability of the main spectrometer HV system measured with the K35 HV divider. A HV of $-18.6\,\text{kV}$ was created with the precision HV supply. The absolute value of the HV was determined with the calibrated precision DVM using the K35 HV divider (the assumed scale factor was 1972.4531). The post regulation system was not active during the measurement. For the uncertainties only the contribution of the DVM was included, since the uncertainty of the scale factor of the HV divider is assumed to be stable over such a time period (see section 5.3). Left: Measured retarding potential of the MS over 15 h. Within the whole measurement time, drifts on the ppm-level can be observed, which are caused by the precision HV supply. Right: Enlarged view of an exemplary 12 min measured interval within the longterm measurement. The standard deviation of $8\,\text{mV}$ is below 1 ppm. For the whole measurement, the stability of the HV system outperforms the KATRIN limitations of 3 ppm. Note that the red frame should only illustrate the section of the short-term measurement which was extracted from the whole data and is not true to scale.

measurement data. The scattering of the HV is below $10\,\text{mV}$ (standard deviation $\sigma = 8\,\text{mV}$), without a clear drift of the system. This time interval was chosen, because for the final tritium measurement runs the time for each voltage will be in the order of 10 min. This result demonstrates, that the HV system is stable regarding the creation and measurement of the retarding potential on this time scale of minutes to hours, outperforming the KATRIN specifications of 3 ppm. However, with the K35 and the precision DVM only the DC part of the retarding potential can be measured, since the DVM integrates (depending on the desired precision) up to $8\,\text{s}$ for one measurement. This means, that HF noises with frequencies of $1\,\text{Hz}$ and higher can not be investigated with this measurement system. For the suppression and analysis of AC fluctuations of the retarding potential the post regulation system is installed, which is discussed in the next section.

The stability of the system on times scales of weeks and months is depending on the calibration of the HV dividers. This issue is treated in the following chapters of the thesis.

In order to analyze the stability of the HV system on smaller time scales systematically, the above mentioned longterm measurement was divided into 15 segments of 1 h each. Since during the tritium measurements usually all sub-runs (a tritium measurement run consists of several sub-runs for the individual retarding potentials) are in the order of 10 min or shorter, this segmentation appears as a reasonable conservative approach (the short-term stability was already shown in figure 4.4 to be sufficient at the 10 min scale). For each interval, the corresponding mean value and standard deviation was calculated, which is shown in figure 4.5 a) with the red points. For clarity reasons, the uncertainties of the longterm measurement data points were set to zero. The calculated mean values for each of the 15 intervals feature the respective standard deviation as uncertainty.

For all data points within their corresponding measurement hour the relative deviation from the mean value was calculated. Figure 4.5 b) shows the histogram which contains all deviations over the complete measurement time of 15 h.

The data points are normally distributed and can be described by a Gaussian

$$f(x) = \frac{A}{\sqrt{2\pi\sigma^2}} \cdot e^{-\frac{(x-\mu)^2}{2\sigma^2}} \tag{4.2}$$

with the Amplitude A, width σ and mean value μ. The small standard deviation of about $\sigma = 0.4\,\mathrm{ppm}$ is an indicator for the stability of the system, showing that the spread of the measured voltages is in the sub-ppm-range. The mean value
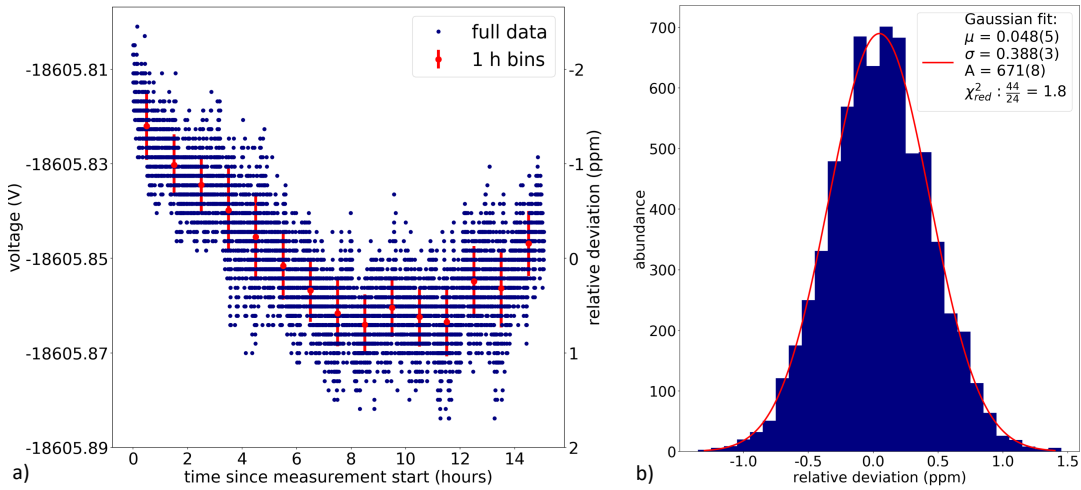

Figure 4.5: Analysis of 1 h intervals of the longterm measurement shown in figure 4.4. a) The whole data was divided into 15 segments of 1 h each. The red points show the mean values calculated for each interval. The uncertainties of the mean values are given by the standard deviation. For clarity, the uncertainties of the blue data points are hidden. b) For each 1 h interval, the relative deviation of the data from the mean value was calculated and filled into the histogram. The bin size was set to 0.1 ppm, corresponding to the resolution of the DVM. The data is normally distributed and the Gaussian fit shows a small standard deviation of only $\sigma = 0.4\,\mathrm{ppm}$.

of 0.048(5) ppm is not compatible with 0 within the uncertainties. Since on the main spectrometer high-voltage potential multiple HV supplies and other devices (e.g. large turbomolecular pumps and isolating transformers) are operated, the distribution of data points is not expected to be completely Gaussian, which explains the sub-ppm-shift of μ. This can also be seen by the comparably large value of $\chi^2_{\mathrm{red}} = 1.8$. However, one can conclude from this analysis, that the precision HV system maintenance and monitoring outperforms the KATRIN requirements.

4.2 Post regulation system

The 3 ppm limitation for uncertainties of the retarding potential (see section 3.1) holds for longer measurement intervals like described in the previous section as well as for short time scales. The long periods of several seconds and more are monitored with the precision HV dividers and DVMs. However, although the HV is created with a specially designed precision HV supply, HF noise and AC fluctuations of the system are expected. These can originate from the HV supply or couple into the system via the main spectrometer, which works to some extent as an electromagnetic antenna. Furthermore, several electrical devices (e.g. turbomolecular pumps or HV supplies) are operated on the potential of the vessel, which are expected to create HF disturbances of the retarding potential. In order to attenuate the AC part, two counteractions are pursued.

Firstly, three HV capacitors were installed at the pre-spectrometer side of the MS (see the picture in figure 4.6). They connect the MS vessel with ground potential via a capacitance of $C = 7\,\mathrm{nF}$ for each element. As the electrical reactance of a capacitor X_{C} scales with the inverse of the frequency f

$$X_{\mathrm{C}} = \frac{1}{2\pi f C},\tag{4.3}$$

HF noise of the retarding HV in the MHz range or higher gets diverted to ground potential. The theoretical reactance of the three parallel HV capacitors is shown in the right part of figure 4.6. While the resistance for DC and low frequent noises is in the MΩ range and higher, $>$MHz AC fluctuations of the retarding potential are minimized by the low impedance of the capacitors at these frequencies.

Secondly, for the range of DC up to 1 MHz fluctuations an active post regulation (PR) is used. This system was designed and built by S. Wüstling[1]. First commissioning measurements and a detailed discussion about the influences of HF noises on measurements with the main spectrometer at KATRIN are discussed in [33]. In the next sections, the setup of the system and longterm stability measurements performed in the context of this thesis are presented.

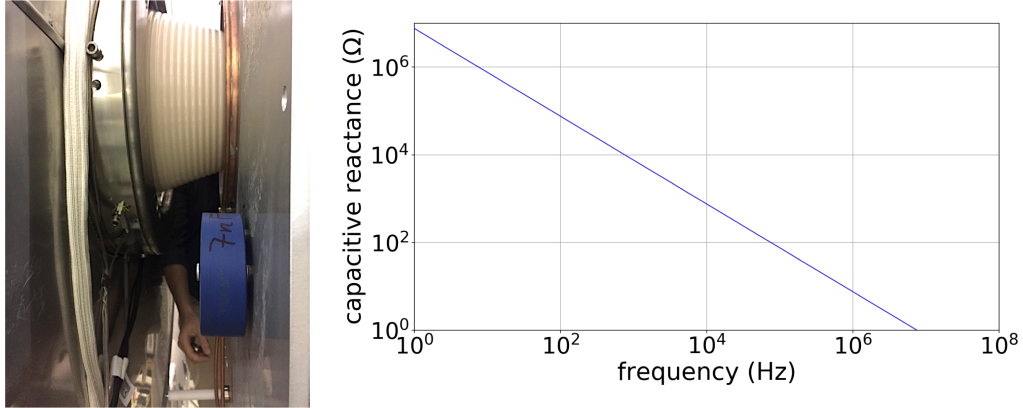[1]Karlsruher Institut für Technologie, Institut für Prozessdatenverarbeitung

Figure 4.6: Left: Picture of one of the three installed HV capacitors (blue) between the MS (right) and the PS (left). In the middle of both spectrometers, the ceramic insulator can be seen. The three capacitors are installed symmetrically around the ceramic insulator. Right: Theoretical reactance of a parallel connection of three capacitors with 7 nF each. The impedance scales with the inverse of the frequency and drops over several orders of magnitude for a range of 1 Hz to MHz and higher.

4.2.1 General concept

In order to reduce the AC part of the retarding potential up to frequencies of 1 MHz, an active regulation system (post regulation) based on a triode shunt is used. The schematic overview of the system is shown in figure 4.7. The general idea of this regulation is to create a low impedance path for HF noise, which can be controlled in dependence of the measured fluctuations of the MS retarding potential.

The main HV supply gets a set-point from the SlowControl system (SCS) and creates the retarding potential, which features an unknown extent of fluctuations. The high-frequent part above 1 MHz gets diverted to the ground potential of the beam tube (at the source side of the spectrometer) by the HV capacitors. Simultaneously, the noise amplitude is measured with a so-called ripple probe, connected and located also at the same side of the MS. The amplified HF noise is then fed into the post regulator, which controls the triode shunt in order to smoothen the MS retarding potential. The simplified working mechanism of the triode shunt can in principle be described by two electrodes (the main spectrometer and ground potential) with a grid in-between. The current from the cathode to the anode can be controlled by the voltage difference between the grid and the cathode. In the case of the MS, the controllable shunt current has to be between 0 and 1 mA.

The post regulator also requires a DC path, where the actual applied HV is compared to the set value. In order to measure the HV DC value, an additional auxiliary HV divider is used, installed next to the HV distribution rack at the
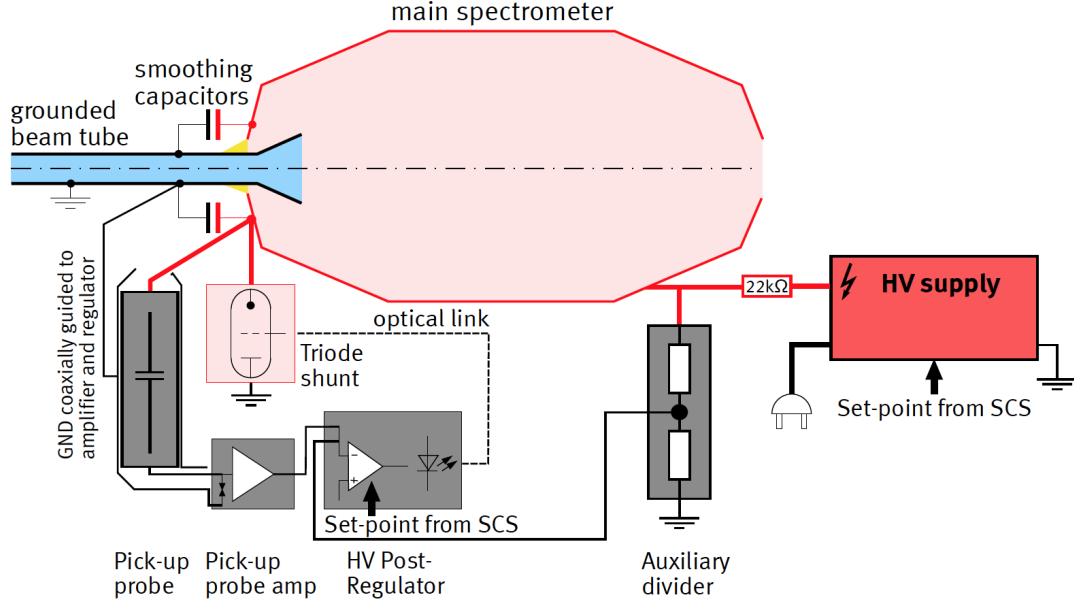
Figure 4.7: Schematic overview of the post regulation system. The AC part of the retarding potential is measured with a pick-up ripple probe and amplified fed into a post regulator, which controls the triode shunt in order to smoothen the retarding potential. An auxiliary HV divider is used to measure the DC component. The actual HV applied to the MS (which is created by a HV supply) is compared to a set-value and the difference is compensated by the PR, allowing HV adjustments in the order of 10 V. Details about the working principle are given in [33]. An important key factor for the stable operation of the shunt regulator is a $22\,\text{k}\Omega$ resistance in series connection between the MS and the main HV supply. The image was taken from [36].

basement of the MS. With the post regulation system not only HF noise can be reduced, but also the DC value of the retarding potential can be adjusted up to about 15 V. This means, that the actual HV of the MS is not directly controlled by the set value of the main HV supply, but by the set value of the post regulation. If the difference of both set values exceeds the working range of the post regulation, the active AC compensation is not working and the system notifies the operator by status indicators. Details on the software control of the system within the KATRIN SCS are given in [78].

The ripple probe of the post regulation system can be used in order to measure the HF noise of the retarding potential directly with an oscilloscope. An exemplary measurement, performed during the HV commissioning phase, is presented in figure 4.8. Here, two measurements are shown: one with (blue) and one without (red) active post regulation.

It could be demonstrated, that the sinusoidal noise with a frequency of 50 Hz was reduced by more than one order of magnitude to values below 20 mV, corresponding to 1 ppm at $-18.6\,\text{kV}$. This outperforms the KATRIN limitations
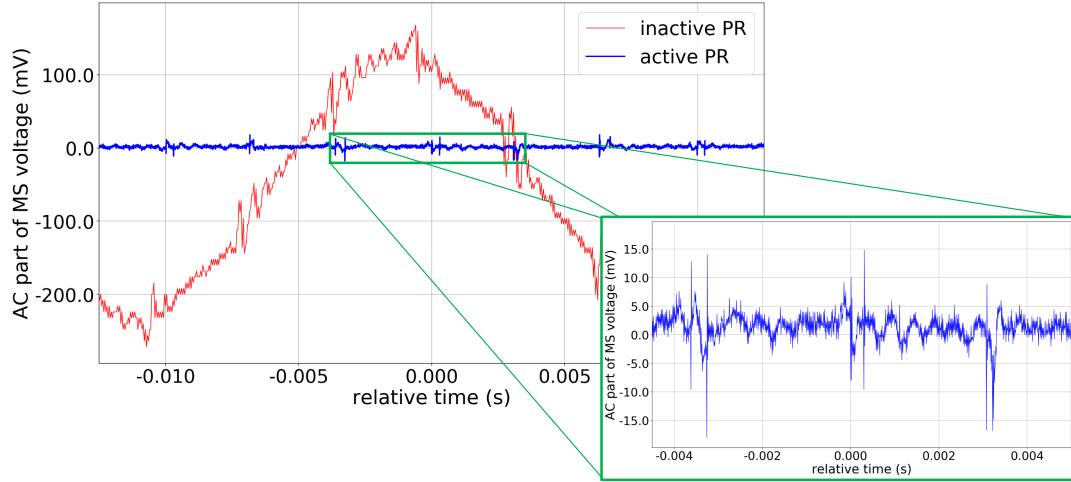
Figure 4.8: Comparison of the AC part of the MS retarding potential with and without active post regulation. Without PR, a sinusoidal ripple with $\mathcal{O}(100\,\text{mV})$ amplitude and a frequency of about 50 Hz is observed. When the post regulation system is active, the ripple is reduced by more than one order of magnitude to values below 20 mV (see enlarged plot).

of 3 ppm. In order to be functional for voltages up to $-35\,\text{kV}$, the post regulation system was upgraded after the commissioning phase. These results are in agreement with previous measurements in [33], where comparable tests with a slightly different setup were performed.

The AC ripple (without active PR) was measured for different HV. It showed a voltage dependent behavior with an increase at higher retarding potentials and a maximal value of about $420\,\text{mV}_{\text{pp}}$ at $-35\,\text{kV}$. The values of the corresponding voltages are specified for the respective measurements in chapter 6.

4.2.2 DC stability measurements

Since the PR system is also used in order to adjust the DC values of the MS retarding potential, the longterm stability was investigated during the HV commissioning phase analog to the measurements presented in section 4.1.3. The DC stability of the retarding potential, achieved with active PR, is mainly dependent on the stability and drift of the auxiliary HV divider.

Figure 4.9 shows a longterm measurement of the HV with active post regulation. The setup for the measurements was:

- a power supply was connected to the main spectrometer, creating a HV of $-18.6\,\text{kV}$; it is not necessary to use the precision HV supply in this configuration, since the absolute value and set point of the retarding potential are controlled by the post regulation

- the IE common and offset HV supplies were short circuited during the measurements

- the post regulation system was active

- the K35 and the MoS were connected to the MS.

A similar trend as in the measurement without active post regulation can be observed, although the absolute longterm spread of the HV is higher (about 10 ppm compared to 3 ppm). For the exemplary short-term measurement extracted from the 14 h, also a similar behavior can be observed. Here, the standard deviation is slightly higher compared to the measurement with the precision HV supply and inactive post regulation (14 mV vs. 8 mV). However, related to the KATRIN limitation of 60 mV, this result is satisfying, since it outperforms the requirements.

For this measurement the same longterm stability analysis as for the precision HV supply was performed, which is shown in figure 4.10. The measurement time was divided into 14 segments with 1 h each. The red points indicate the mean values and the uncertainties are given by the standard deviation of each
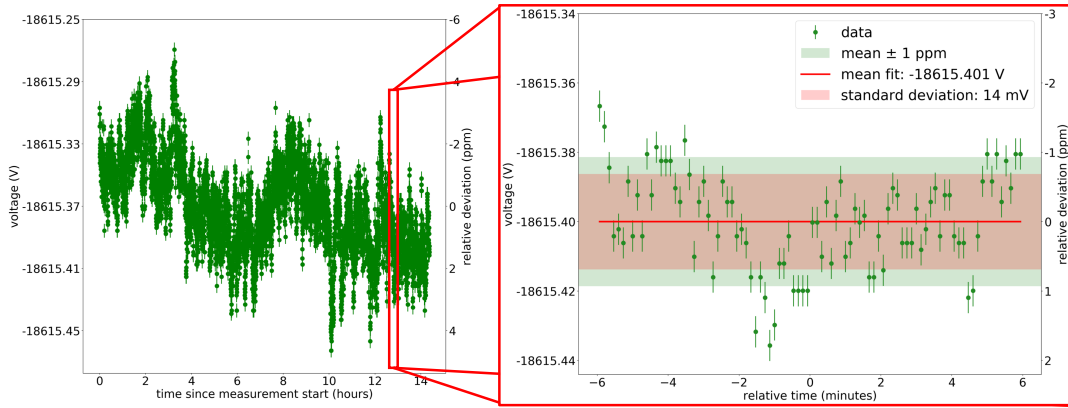

Figure 4.9: Longterm stability of the main spectrometer HV system measured with the K35 HV divider. The HV of $-18.6\,\text{kV}$ was created with a HV supply and actively smoothened by the post regulation. The absolute value of the HV was determined with the calibrated precision DVM using the K35 HV divider (the assumed scale factor was 1972.4531). For the uncertainties only the contribution of the DVM was included, since the uncertainty of the scale factor of the HV divider is assumed to be stable over such a time period (see section 5.3). Left: Measured retarding potential of the MS over 14 h. Within the whole measurement time drifts on the ppm-level can be observed, caused by the auxiliary HV divider of the post regulation system. Right: Enlarged view of an exemplary 12 min measured interval within the longterm measurement. The standard deviation is below 1 ppm. For the whole measurement the stability of the HV system outperforms the KATRIN limitations of 3 ppm. Note, that the red frame should only illustrate the section of the short-term measurement extracted from the whole data and is not true to scale.

time interval. Examining the relative deviation of the data for each hour to their mean value, the histogram in figure 4.10 b) shows that the data points are normally distributed in this analysis. Here, the standard deviation of about 1.0 ppm is almost a factor of 3 higher compared to the measurement presented in section 4.1.3. In addition to the standard devices, in this measurement also the active post regulation system was operated on HV. As this active control system smoothens the AC contribution and also changes the DC part of the HV – highly depending on the stability of the PR auxiliary HV divider – even larger deviations from an ideal Gaussian shape are expected. This can be seen by the $\chi^2_{\mathrm{red}} = 1.9$ value and again by the shift of μ. However, this also outperforms the KATRIN requirements.

It can be concluded, that the performance test measurements of the HV commissioning phase demonstrated, that with the two discussed configurations (precision HV supply and inactive PR & arbitrary HV supply and active PR) the KATRIN requirements regarding short- and longterm stability can be outperformed. Since in the first configuration HF noise, which can not be detected with the HV dividers and precision DVMs, is not compensated, the measurement mode with an active post regulation is used for the normal KATRIN operation. Here, the precision HV supply in principle is not required, because the stability is limited by the auxiliary HV divider of the post regulation system.
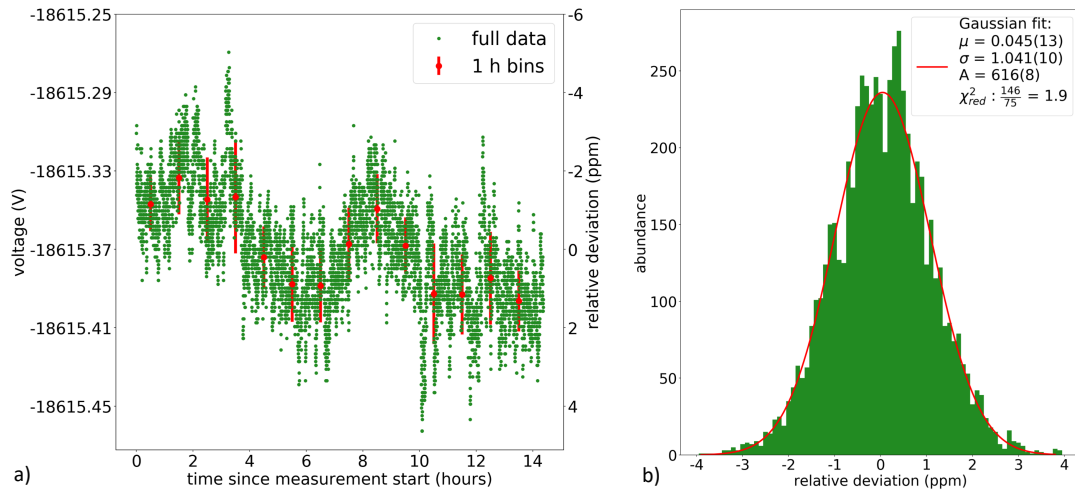

Figure 4.10: Analysis of 1 h intervals of the longterm measurement shown in figure 4.9. a) The whole data was divided into 14 segments of 1 h. The red points show the mean values calculated for each interval. The uncertainties of the mean values are given by the standard deviation. For clarity, the uncertainties of the green data points are hidden. b) For each 1 h interval the relative deviation of the data from the mean value was calculated and filled into the histogram. The bin size was set to 0.1 ppm corresponding to the resolution of the DVM. The data is normally distributed and the Gaussian fit shows a small standard deviation of $\sigma = 1.0$ ppm.

Finally, it is important to mention that for KATRIN in the first instance the uncertainty of the HV measurement needs to be precise on the ppm-level. The creation and stability of the actual retarding potential (on the $>10\,\mathrm{s}$ time scale) are not as critical, since they are measured with the HV dividers.

4.3 Fast voltage measurement system

Since the WGTS will be operated on ground potential, the scan of the tritium spectrum has to be performed by varying the retarding potential of the main spectrometer. This requires voltage measurements in the range of $-18.6\,\mathrm{kV} \pm 500\,\mathrm{V}$ on a time scale in the order of seconds and minutes. Figure 4.11 shows a schematic overview of the electrical setup for this standard measurement mode. The HV supply creates the MS retarding potential U_MS, which is used to scan around the tritium end point at -18.6 kV with several minutes for each voltage. In order to simplify the illustration, U_MS contains all HV supplies, which are used to create the MS retarding potential (main and IE common HV supply) with active post regulation. The HV is measured directly with the K35 (or K65) HV divider and a precision DVM (U_K35). The precision DVMs integrate over about $10\,\mathrm{s}$ in order to achieve a relative uncertainty in the 10^{-7} range for the voltage measurement. This limits the minimal length of a measurement interval for a sub-run with a specific voltage to $>30\,\mathrm{s}$, since the HV should be monitored over multiple DVM measurement points in order to check the stability. Furthermore, valuable measurement time gets lost, since a sub-run only starts after the retarding potential is stable on the ppm-level, measured with the HV
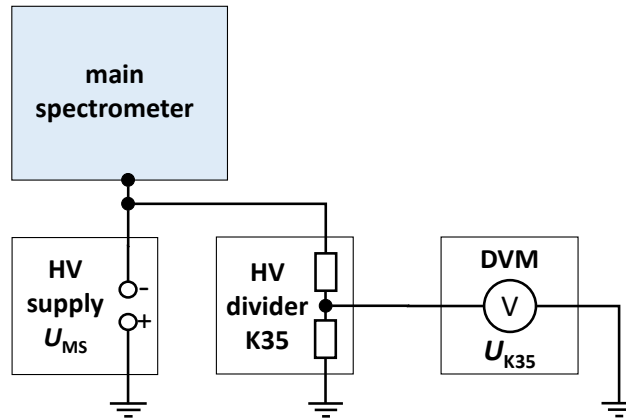

Figure 4.11: Simplified schematic overview of the HV components for the standard tritium measurement mode at KATRIN. A HV supply creates the retarding potential U_MS of the main spectrometer, which is also distributed to the K35 HV divider and measured with a precision DVM. In order to scan the tritium endpoint region, U_MS is varied. In this configuration, the ppm-precise HV measurement takes several seconds, since it is limited by the integration time of the precision DVM.

divider and precision DVM. During discussions of the optimal measurement time distribution for the tritium measurements within the collaboration, the question arose, if this interval could be reduced. In the context of this thesis, a solution of this challenge was developed and tested, presented in the next subsections.

4.3.1 Idea

The general idea of the new concept is to divide the voltage measurement of the retarding potential into two steps:

- a static HV of $U_{\mathrm{ref}} = -18.6\,\mathrm{kV}$ is created with the precision HV supply and measured with one of the KATRIN HV dividers; this HV is isolated from the MS and used as a reference potential

- the fast changing HV of $U_{\mathrm{MS}} = -18.6\,\mathrm{kV} \pm 500\,\mathrm{V}$ is created with a second HV supply and the usual components of the HV system (including the post regulation) located in the HV distribution rack; the difference of this two voltages is measured with a fast DVM, using only an integration interval on a sub-second time scale for each voltage measurement.

The schematic overview of this setup is shown in figure 4.12. A standard HV supply and the active post regulation system create the vessel potential, which is used to scan around the tritium end point at $-18.6\,\mathrm{kV}$ with several seconds for each voltage. The reference potential, created by the independent precision HV supply, is measured with the K35 (K65) HV divider and a precision DVM (e.g. Fluke 8508A 8.5 digits). The difference between both potentials is measured with the faster DVM U_{diff} (e.g. Fluke 8846A 6.5 digits), which has integration times of only $0.3\,\mathrm{s}$. Since the voltage difference of the main spectrometer and the reference potential is smaller than $1\,\mathrm{kV}$, the resolution of a comparably fast measuring DVM is high enough in order to measure on the mV level and to stay below the limit of $60\,\mathrm{mV}$. In this configuration the post regulation system is used to scan the spectrum by changing U_{MS} with small voltage steps. The DVM that measures the voltage difference has to be operated on top of the reference potential inside a HV cage (see next subsection). In order to determine the retarding potential U_{MS}, both measured voltages have to be added, leading to a slightly increased uncertainty, since the voltage determination now consists of two separate measurements and therefore, the uncertainties have to be summed quadratically:

$$U_{\mathrm{MS}} = U_{\mathrm{ref}} + U_{\mathrm{dif}} \tag{4.4}$$

$$\Delta U_{\mathrm{MS}} = \sqrt{(\Delta U_{\mathrm{ref}})^2 + (\Delta U_{\mathrm{diff}})^2}. \tag{4.5}$$

The system was installed at the MS and tested for the first time during the HV commissioning measurement phase. The technical realization of the system is described in the next subsection. Subsequently, test measurements are presented
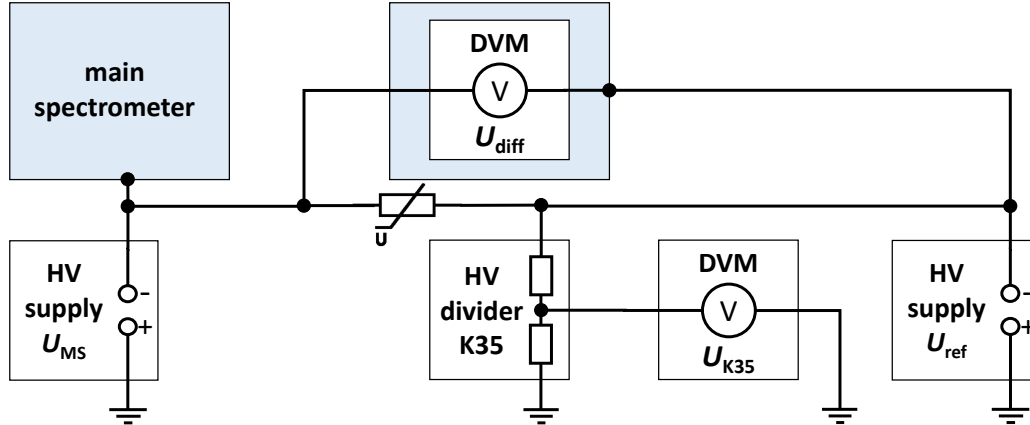
Figure 4.12: Simplified schematic overview of the HV components for the fast measurement mode. The retarding potential of the main spectrometer U_{MS}, which is varied in order to scan the tritium endpoint, is created by a HV supply. Independently, a precision HV supply creates a second, constant HV. This reference potential is measured with the K35 HV divider and a precision DVM. Inside a HV cage (blue area), a faster DVM with less resolution measures the difference of the two potentials, which is below 1 kV. In order to protect the fast DVM against too high voltage differences (above 1 kV), a voltage dependent resistance (VDR) is installed parallel to the DVM between the two potentials.

in section 4.3.3. Especially the post regulation HV adjustment system and the influence of U_{MS} voltage changes on U_{ref} were investigated.

4.3.2 Technical realization

Two HV supplies are required for the fast HV measurement mode. For the main spectrometer, the standard setup of the HV system is used as described in section 4.1.2. As mentioned above, a precision HV supply is not needed, since the post regulation system controls the actual applied voltage (see section 4.2) and sets different voltages. The reference potential has to be constant and stable on the ppm-level for timescales in the order of minutes. The measurements presented in section 4.1.3 demonstrated that the precision HV supply FuG HCP 70M-35000 is suitable for this task.

In order to operate the fast DVM Fluke 8846A for the difference measurement on the reference potential, a HV cage was designed and built in cooperation with C. Huhmann[2]. Figure 4.13 shows a picture of the cage after it was installed at the basement of the main spectrometer. The outer cage serves as protection against contact, since the inner cage is operated with voltages up to -35 kV. The K35 HV divider in combination with a precision DVM (Fluke 8508A) was used in order to measure the reference potential. From the HV distribution rack, a wire

[2]Institut für Kernphysik, Westfälische Wilhelms-Universität Münster

Figure 4.13: Picture of the HV cage installed at the basement of the main spectrometer. To the isolated inner cage a HV of up to $-35\,\text{kV}$ can be applied. The devices inside can be operated at this potential and are supplied with power by an isolating transformer, located at the basement. The outer cage is grounded and serves as protection against contact.

with the IE common potential was installed to the cage, such that the difference of the two potentials can be measured with the DVM, which was operated and read out via an optical fiber. The devices inside the HV cage were supplied with power by an isolating transformer (Tauscher TRGTEP 3000VA), installed at the basement of the inner cage.

In order to protect the DVM against too high voltage differences, a standard voltage dependent resistor (VDR) with a varistor voltage of $895\,\text{V}$ was installed between the two inputs of the DVM.

4.3.3 Test measurements in combination with post regulation

Since the standard HV measurement configuration of the precision HV monitoring system is limited to time scales above $10\,\text{s}$ by the KATRIN HV dividers and precision DVMs, the short-term performance of the post regulation system could

not be examined in this setup. With the fast HV measurement mode, for the first time a tool for ppm-precise measurements was available, providing the possibility to investigate that time scale. This is especially important in order to answer the question about the minimal required length of measurement runs (regarding the HV point of view). Additionally, the behavior of the post regulation, when it changes the retarding potential, can be recorded and analyzed with a frequency of about 3 Hz.

Figure 4.14 shows three exemplary measurements, where the MS retarding potential was changed with the PR by 1 V, 5 V and 10 V. Higher voltage changes can not be performed directly with the PR and have to be done with the main HV supply of the MS.
It was analyzed, after what time period the PR stabilizes the newly adjusted voltage to the ppm-level ($< 20 \, \mathrm{mV}$). The uncertainties in figure 4.14 only contain the contribution of the fast DVM, which is below 1 mV in this measurement range and therefore not visible:

$$\Delta U_{\mathrm{diff}} = 0.0013 \, \%(\text{measurement}) + 0.0004 \, \%(\text{range})^3 < 1 \, \mathrm{mV}. \qquad (4.6)$$

The contribution from the reference potential is neglected, since the relative and not the absolute voltage is investigated and U_{ref} stayed constant during the measurements. The influence of HV changes with the post regulation on the reference potential is discussed later in this subsection.
The general progression after the new set-point was defined by the SCS is similar for all three voltage steps. After an initial steep rise, the retarding potential exceeds the new set voltage by about 10 % and then slowly approaches the stable value after approximately 5 s. The time when a stability of 20 mV is reached depends on the amplitude of the step, increasing with larger voltage changes. The overall uncertainty of the absolute HV value is according to equation (4.5) a sum of the single uncertainties of both DVM. Since the contribution of the fast DVM is negligible small, the dominant factor comes from the precision measurement of the reference potential with the K35. Here, uncertainties of about 1 ppm for the scale factor (see section 5.3) and 0.1 ppm for the precision DVM can be assumed.
This measurements proof, that the method of the fast measurement mode works and can be used at KATRIN within the limitations for the uncertainty of the HV system. The minimal waiting time before a new (ppm-stabilized) measurement can start could be determined to be about 5 s, depending on the voltage step-size. For the sub-run length, time periods of below 10 s with a sufficient number of data points can be chosen, since the integration time of the fast DVM is about 0.3 s. This is a significant improvement compared to the $>30 \, \mathrm{s}$ intervals in the standard mode, considering that one tritium measurement run consists of multiple voltage steps.

---

[3]The values are obtained from the manufacturers manual for the 10 V range for 24 h.
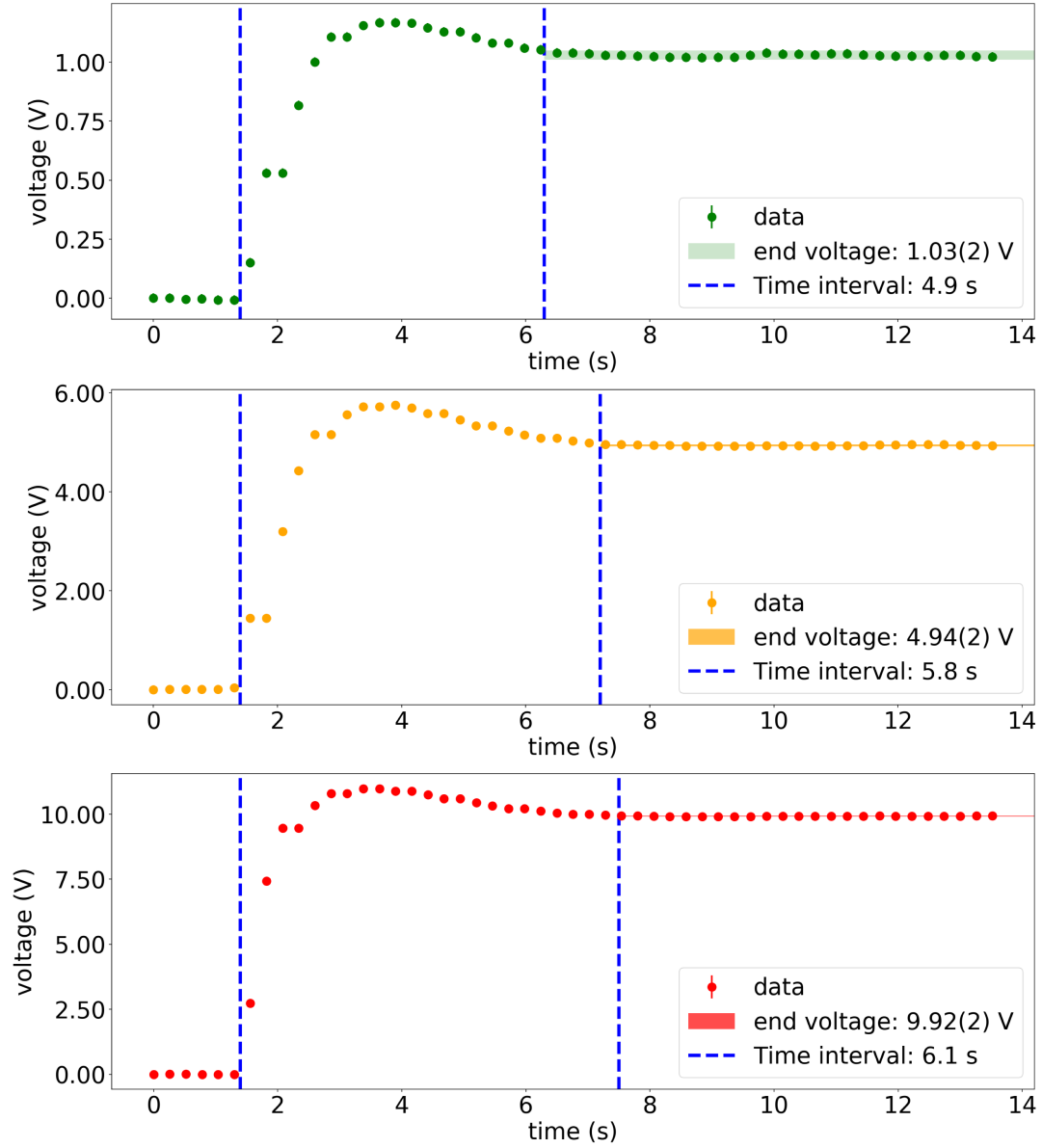
Figure 4.14: Difference voltage measurements between the MS HV and the reference potential with the fast measurement mode. The retarding potential of the MS was changed by the post regulation by different amplitudes. The system is stabilized about 5 s after the HV change, depending on the amplitude of the step.

However, there is a possibility for even faster changes of the retarding potential by the post regulation system. It features an input channel, where an arbitrary HF signal can be fed into the system, which is directly passed to the MS. The motivation for this channel was the idea to investigate influences of HF noise of the retarding potential for the transmission function of the MS. Measurements and the analysis regarding this investigation are presented in [33].

With an arbitrary function generator (AFG), a fast voltage step in the order
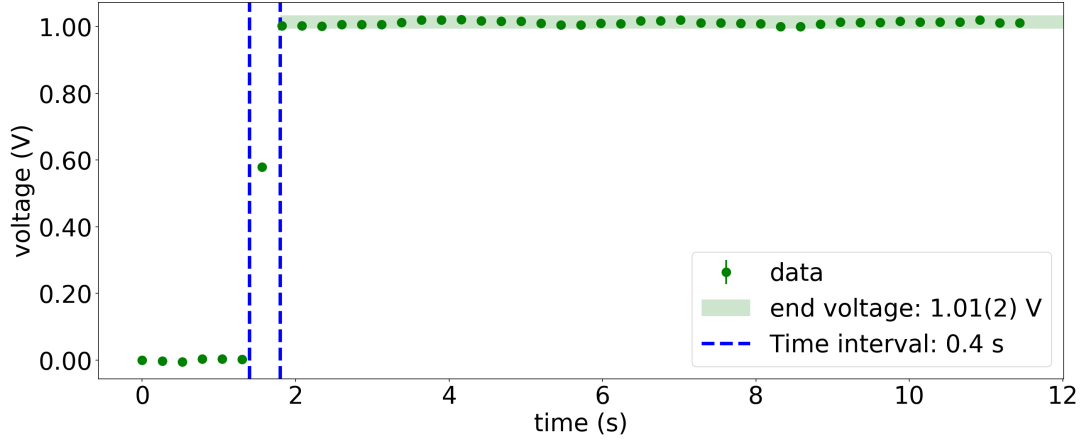
Figure 4.15: Difference voltage measurement for a voltage step performed with the direct input channel of the PR and a AFG. In this configuration, the retarding potential of the MS can be changed by up to 1 V on a sub-second time scale with ppm-precision.

of milli-seconds can be injected to this channel. The post regulation directly translates this into a HV change of the same amplitude for the MS HV. The maximum applicable voltage for this configuration is 1 V. Figure 4.15 shows an exemplary measurement, where it was investigated after what time the MS HV is stable to the ppm-level in this mode. With the fast measurement setup, the time could be determined to about 0.4 s, which is an improvement of about one order of magnitude compared to the standard time the PR needs to change and stabilize the voltage. If there would be any future applications at KATRIN for sub-second HV changes, it can be realized by this configuration. However, since this is limited to 1 V steps, it is not reasonable for the standard tritium measurement mode.

Finally, it was investigated if and to what amount HV changes of the post regulation influence the reference potential in this fast measurement mode. Therefore, the high voltage of the MS was changed periodically by 10 V with the PR. In order to investigate the short-term influences of these HV changes on the reference potential, a second fast DVM of type Fluke 8846A was used in combination with the K35, because of the large integration time of the precision DVM. The result of this measurement is shown in figure 4.16. On the left y-axis in green, the difference voltage between reference and MS potential is shown. The blue data and the right y-axis show the reference potential, measured with the K35 and the second fast DVM. Every time, when the HV of the MS is decreased by 10 V with the PR (which can be seen with the green data points), the reference potential decreases about 2 ppm to 4 ppm, and when the HV is increased, a corresponding increase of the reference potential can be observed. Since the two separate high voltages are coupled via the input resistance of the DVM, an interference to some extent was expected. Even if the effect is only on the ppm-level, it has to be taken into account when the fast measurement mode is considered for
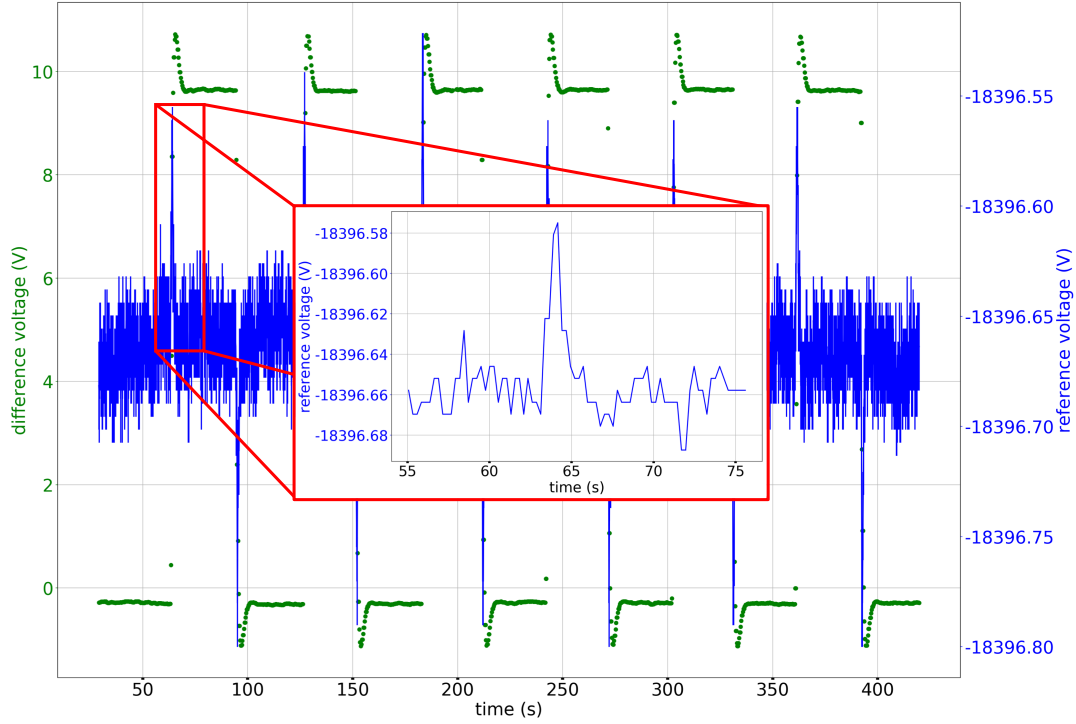
Figure 4.16: Influence of HV changes with the PR system on the reference potential in the fast measurement mode. The green data points and the left y-axis show the difference voltage between MS and the reference potential, measured with the fast DVM. On the right y-axis in blue the reference potential measured with the K35 and the precision DVM is shown. When the HV of the MS is changed, the reference potential is influenced on the ppm-level. For the HV measurement of the reference voltage, an uncertainty of $20\,\mathrm{mV}$ ($1\,\mathrm{ppm}$) was assumed. The enlarged image in the center of the plot shows one of the steps for the reference potential. For clarity, here the uncertainty of the HV measurement is not shown.

measurements at KATRIN. However, as shown in the enlarged image in figure 4.16, the length of this effect is smaller than $5\,\mathrm{s}$. Since in the standard mode the post regulation itself needs $>5\,\mathrm{s}$ to stabilize the HV to the ppm level, this process is negligible, since the measurement only starts when the HV is stabilized.

To conclude, it could be demonstrated, that the newly developed method and installed setup for a fast ppm-precise measurement of the retarding potential of the main spectrometer works and fulfills the KATRIN requirements regarding the HV uncertainty. Furthermore, for the first time working characteristics of the post regulation system regarding time constants for HV changes could be investigated. This fast measurement method improves the time needed for a ppm-precise HV determination by one order of magnitude compared to the standard mode.

During a Kr-83m measurement campaign in 2017, first measurements with this method were performed as presented in section 6.5.

4.4 Pre-spectrometer

The pre-spectrometer is used in order to cut off the low-energy part of the tritium-β-decay electrons. The full amount of the decay electrons could create additional background, if they would reach the MS. Therefore, it is operated at HV a few 100 V below the tritium endpoint, reflecting most of the electrons before they reach the MS. Because of the configuration of two cascaded MAC-E-filters with a grounded element of the beam line in between, electrons can be captured in this Penning-Trap system. Since this can lead to discharges that could damage the HV system of both spectrometers, active countermeasures are taken, in order to avoid the filling of the trap. Multiple movable rods (so-called Anti-Penning wipers) are installed between the two spectrometers, which can be moved inside the beam line. The trapped electrons hit the rods and are removed from the trap. Details about this system are given in [66].

Since no precision measurements are performed with the PS, a standard HV supply is used in order to create its retarding potential, which is applied to the vessel. Commissioning measurements of the setup are presented in [79].

Just like the MS, the inner surface of the PS is covered with a wire electrode system. Here, only four elements can be operated at different potentials: the up- and downstream cones and in the central part the east and west dipole electrodes. In addition to the basic HV supply of the PS, the inner electrode can be operated on a more negative potential, created with offset HV supplies (type ISEG NHQ 205M) for voltages up to 5 kV. Overall, two devices are available with 2x2 channels.

In the context of this thesis and in cooperation with [33], a simple patch panel was designed and installed at the PS in order to connect the electrodes to the different HV channels. Figure 4.17 shows two pictures of the patch panel and the HV supplies installed in a crate directly next to the pre-spectrometer. With the patch panel it is possible to connect all four electrodes of the PS to the same HV supply or vessel potential. Furthermore, any arbitrary configuration, including individual offsets for every electrode, are possible.

4.5 Miscellaneous

There are other components of the HV system at KATRIN, which were used in previous measurements in the past, or which are not part of the main topic of this thesis. These components, that are not primarily related to the KATRIN precision HV measurement system for tritium runs, are discussed briefly in this section.
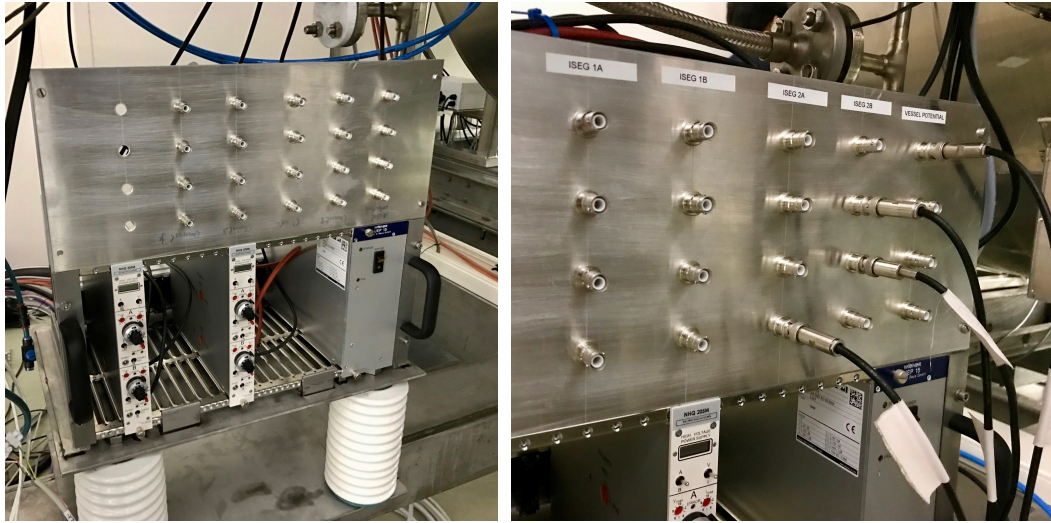
Figure 4.17: Pictures of the built and installed patch panel and HV offset supplies of the pre-spectrometer. As the system is operated on HV potential, it is mounted on isolating ceramic pillars.

Angular selective photo-electron source: In order to investigate the transmission properties of the MS during the second commissioning phase of SDS in 2014, an angular selective, mono-energetic photo-electron source ("e-gun") was used. This apparatus was developed and built in Münster and tested at the monitor spectrometer before it was mounted directly to the MS on the pre-spectrometer side, when the PS and MS were not connected. In this work, only the HV system for the e-gun is discussed. The mechanical design and measurements with the apparatus are presented in [44] and [56].

The basic idea of the setup is to create mono-energetic photo-electrons by guiding light onto a metallic surface (e.g. a silver plated stainless steel holder). To the metallic surface high voltage is applied, in order to match the kinetic energy of the electrons released by the photo-electric effect with the retarding energy of the MAC-E-filter. A second acceleration electrode with a $+5\,\mathrm{kV}$ more positive potential compared to the metallic surface is used to guide the electrons towards the MS and FPD. In order to investigate the transmission function of the MS, the e-gun HV has to cover a range of $\pm$ a few volt around a fixed retarding potential.

This means that in order to minimize uncertainties in the HV measurement and to avoid the problem of HV fluctuations between the e-gun and the main spectrometer, the MS HV is used directly as acceleration voltage for the e-gun. With an additional HV supply operated on this HV the scanning around the retarding potential can be realized. Figure 4.18 shows the schematic overview of the HV setup of the e-gun for the test measurements at the monitor spectrometer. The setup is comparable to the one used at the MS. The main HV for the MoS is distributed to a cage operated on HV potential. Here, the offset voltage, needed to measure the transmission function, is created in two steps, since only HV

supplies with fixed polarity were available. A battery pack generates a constant offset of $+90\,$V compared to the retarding potential. With an additional HV supply in series, negative offsets of up to -1250 V can be created, such that overall a range of -1160 V to $+90\,$V around the retarding potential is covered.

Two wires with this created HV are guided through a so-called splitter box to the e-gun. The box can be used in order to separate the e-gun from the MS HV, e.g. if background measurements are planned and the e-gun is not needed. Finally, with a third HV supply the constant offset voltage of $+5\,$kV is created for one of the two wires.

After successful measurements with this system, which are published in [56], the e-gun was dismounted from the MS and the PS was connected.

Rear section: At the rear section of KATRIN, an additional photo-electron source is installed. Among other things, it is used in order to measure the energy loss of electrons in the WGTS. The general HV concept of the RS e-gun is similar to the one which is described above for the MS. The vessel HV is looped through the experimental hall via a wire from the main spectrometer to the end of the WGTS in the basement, where the RS e-gun HV cage is installed. Since in this case the vessel and not the about 200 V more negative inner electrode potential is used, only one HV supply with a fixed negative polarity can be used. Details about the setup and measurements will be presented in [78].

Condensed krypton source: As described in section 3.2.2, the condensed source of Kr-83m is used in order to investigate transmission properties of the main spectrometer by measuring the well known conversion line of electrons emitted from the K-shell. Their kinetic energy of 17.8 keV is close to the tritium endpoint of 18.6 keV. The difference of 800 eV can be bypassed by accelerating the electrons with an acceleration voltage of 800 V. This is also implemented at the monitor spectrometer, where the implanted source can be set on high voltage.

Similarly, the cryostat and the substrate of the CKrS can be operated with voltages up to the kV range [37]. Since the relative precision of a post acceleration below 1 kV is for 60 mV only on the 10^{-4} level, commercial HV supplies and DVMs (e.g. MCP 14-1250 and Fluke 8846A) can be used in order to determine the voltage.

An advantage of this setup with an adjustable source potential is that the conversion electron line can be scanned for a fixed retarding potential by varying the source voltage.
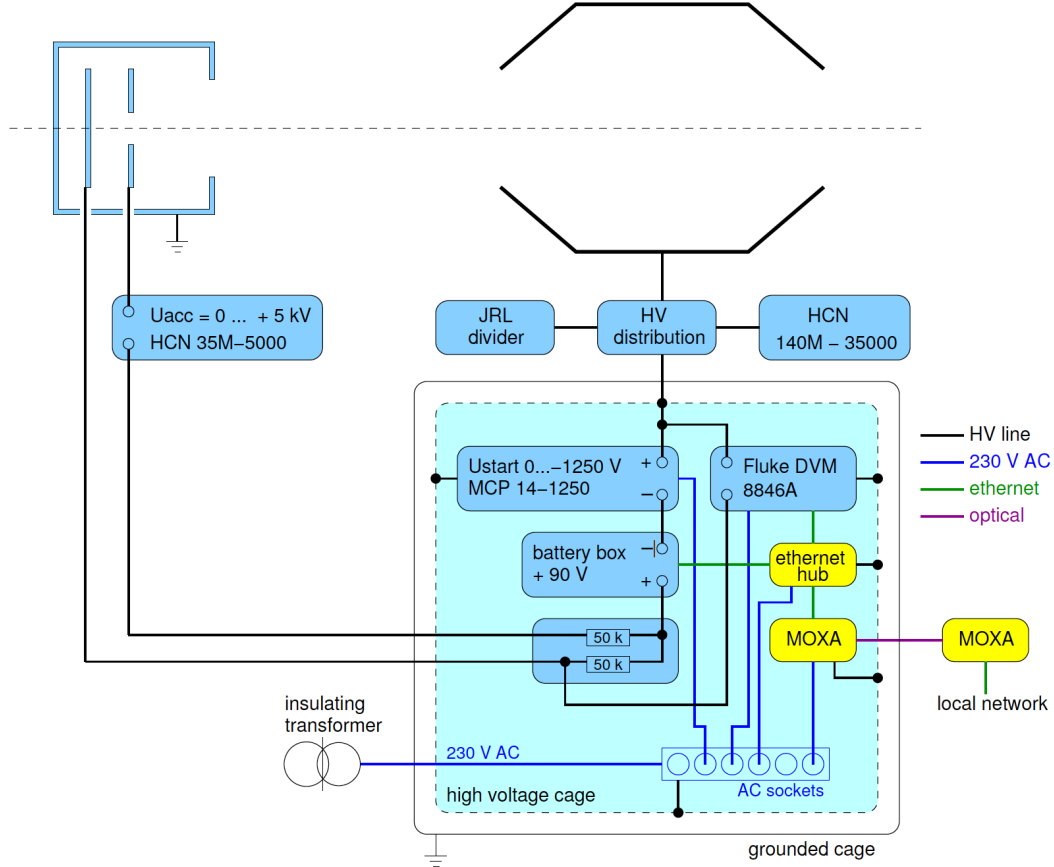
Figure 4.18: Schematic overview of the HV connection scheme for the e-gun at the monitor spectrometer. The HV of the retarding potential is created by a HV supply and distributed to the MoS vessel and a cage operated on HV potential. Here, an additional offset voltage is created by the HV supply MCP 14-1250. Since with this device only negative voltages can be provided, a battery is used in oder to create an additional offset of +90 V. This way, both polarities compared to the retarding potential can be approached. The e-gun requires two HV potentials. The first one is directly coming from the HV cage and distributed to the e-gun. The offset compared to the MS HV is measured with a Fluke 8846A DVM. The second one needs a positive constant offset of 5 kV, which is created with another HV supply (HCN 35M-5000). The image was taken from [80].

NOVEL ABSOLUTE CALIBRATION METHOD FOR PRECISION HV DIVIDERS

At KATRIN, high voltages up to $-35\,\mathrm{kV}$ need to be measured with a precision of $3\,\mathrm{ppm}$ over a measurement period of $2\,\mathrm{months}$. For this application, no commercial HV dividers are available with the required precision. Therefore, the two ultra-precise HV dividers K35 and K65 were developed and built [71, 72] in cooperation with the PTB, according to the model of the MT100, which is one of the most precise and stable voltage dividers in the world [81].

One key aspect for the operation of precision HV dividers are regular calibration measurements. In the past, multiple procedures were developed and demonstrated the possibility of ppm-precise calibrations of the scale factor, the characteristic observable of a HV divider. However, these methods are only applicable at metrology institutes or are limited to small voltages of $\leq 1\,\mathrm{kV}$. In the context of this thesis, a novel absolute calibration method was developed, which overcomes these disadvantages. The basic idea is to determine a differential scale factor directly measured at high voltages, which is used to determine the real scale factor.

The new calibration method can be performed with commercial equipment. Hence, it offers a wide range of applications in science for precision HV measurements, e.g. for defining the kinetic energy of electrons in an electron cooler at storage rings [82] or for the precise determination of the energy of electrons in electrostatic retarding spectrometers or other analyzers [83, 84, 39]. The scope of

applications is not limited to the KATRIN experiment or fundamental research
in general, but is also important for high-voltage direct current (HVDC) electric
power transmission systems, which are currently discussed and planned as part
of the "energy transition" in many countries [85, 86, 87, 88, 89].

Before the novel calibration method is discussed, this chapter gives a general
overview of the KATRIN HV dividers. Since details about the design and setup
are presented in [71, 72], only a brief summary of these topics is discussed.
In 2015, the K65 showed instabilities during calibration measurements. The
investigation of these problems and the repair & upgrade of the HV divider are
presented in section 5.2. Subsequently, former calibration methods and results
over the last years are discussed, before the newly developed absolute calibration
method is presented. Although the discussion is focused on the K35 and K65
and their measurements, the novel method can be applied to other precision HV
dividers, as demonstrated in section 5.7 with the G35 HV divider built for the
usage at an electron cooler at GSI [90, 91].

The essential part of this chapter was submitted to the journal Metrologia
and has been put online on the arXiv [92]. A small part was extracted for
two conference proceedings at a specialized HV conference, both were accepted
for publication in SPRINGER Lecture Notes in Electrical Engineering [91, 93].
The chapter of this thesis is based on the original drafts of the three papers
mentioned above. These drafts were completely written by myself, the additions
and comments of the co-authors entered the published versions of the papers. Of
course, the co-authors contributed to the content of the papers in different depths,
especially the PhD student D. Winzen was involved in the measurements with
the G35 and the uncertainty calculations of the absolute calibration method.

5.1 Overview of the KATRIN HV dividers

Since HV can not be measured directly with ppm precision, HV dividers are
used to scale voltages into the range of typically 10 V. Here, precision digital
voltmeters (DVM) are calibrated with 10 V reference sources, which are traceable
to a natural standard at metrology institutes (see section 3.3).

Figure 5.1 shows a schematic overview of a simple HV divider. It consists
of a chain of multiple ohmic resistors $\sum_{i=1}^{n} R_i$ and a low voltage resistor R_{LV}
connected in series. The output voltage U_{LV} measured over R_{LV} is proportional
to the input voltage U_{HV} of the divider. The characteristic observable is the
so-called scale factor M:

$$M := \frac{U_{\mathrm{HV}}}{U_{\mathrm{LV}}} = \frac{\sum_{i=1}^{n} R_i + R_{\mathrm{LV}}}{R_{\mathrm{LV}}} = \frac{\sum_{i=1}^{n} R_i}{R_{\mathrm{LV}}} + 1. \tag{5.1}$$

Depending on the properties of R_{LV} compared to the overall resistance, arbitrary
and also – if R_{LV} consists of multiple resistors – numerous scale factors can be
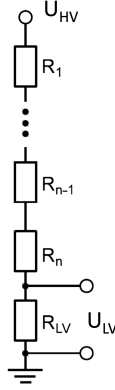
Figure 5.1: Schematic overview of a simple HV divider. The output voltage U_{LV} measured over a part R_{LV} of the resistor chain R_i is proportional to the input voltage U_{HV}. The proportionality factor is called scale factor M.

realized. Following equation (5.1), M depends on the ratio of R_{LV} and $\sum_{i=1}^{n} R_i$. If HV is applied to a voltage divider, its individual resistances might change due to dissipated power caused by Joule heating. Since the power of heating P scales quadratically with the current I and linearly with a resistance R

$$P \propto I^2 \cdot R = \frac{U^2}{R}, \tag{5.2}$$

one can conclude, that the resistances R_{LV} and R_i, and thus the scale factor M, are voltage dependent:

$$M = M(U_{\mathrm{HV}}). \tag{5.3}$$

To mitigate this effect, the total resistance of precision HV dividers is typically in the MΩ-range or higher, limiting the electrical current through the system to less than $1\,\mathrm{mA}$. Furthermore, usually high-quality resistors (e.g. [94]) with a low temperature coefficient in a closed stabilized thermal environment are used, resulting in low temperature dependency and long term stability of the scale factor in the (sub)-ppm range [71, 72, 81].

The following paragraphs give an overview over the K65. As both KATRIN HV dividers feature a similar setup, key components and designs are comparable. Figure 5.2 shows the circuit diagram of the K65. 165 precision resistors ($R_{1\text{-}165}$) create, in combination with 14 tap-resistors R_{LV}, the primary divider chain with a total resistance of $147\,\mathrm{M\Omega}$. Prior to the assembly of the HV divider, temperature dependency measurements of each resistor were performed in order to match single resistors with negative and positive temperature coefficients. It was shown, that the scale factors of the KATRIN dividers have a temperature dependency of less than $0.1\,\mathrm{ppm\,K^{-1}}$ and a voltage dependency of less than $0.1\,\mathrm{ppm\,kV^{-1}}$ [71, 72].

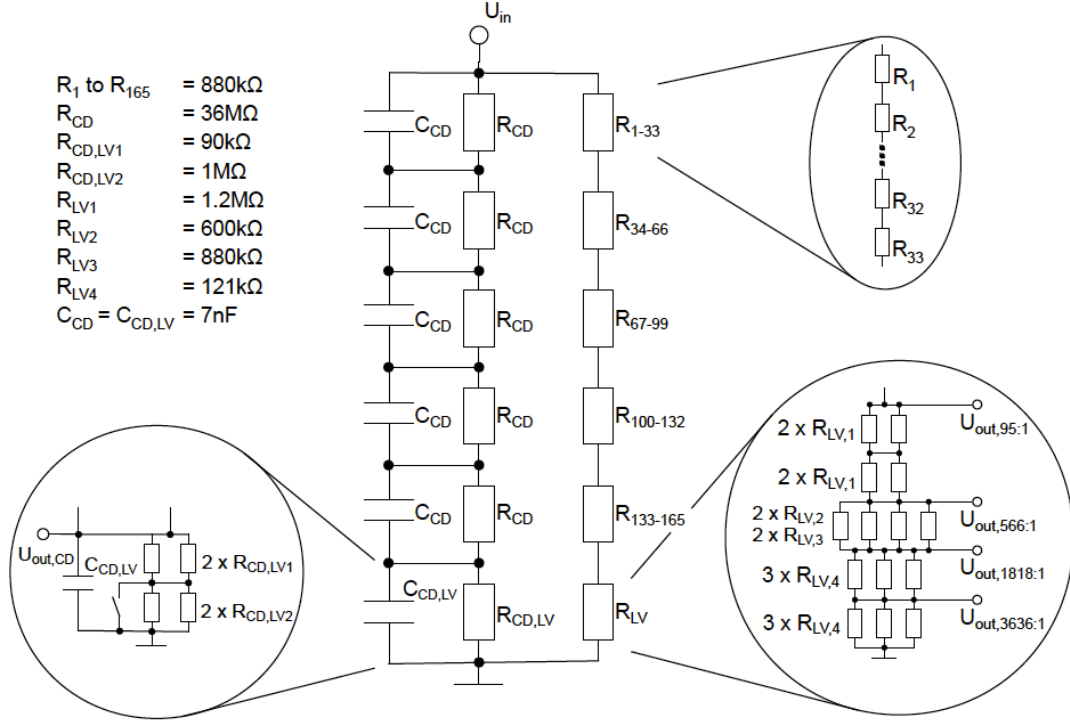The arrangement of the low voltage resistors results in multiple voltage taps (rounded):

Figure 5.2: Circuit diagram of the K65. The primary divider consists of 165 precision resistors connected in series each with $880\,\mathrm{k\Omega}$ and 14 low voltage resistors with resistances between $0.1\,\mathrm{M\Omega}$ and $1.2\,\mathrm{k\Omega}$. Multiple scale factors are realized. The secondary resistor chain protects the divider against HV transients, since the capacitive-resistive setup acts ass a high-pass filter. The image was taken from [36].

- 100:1 is used mainly for calibration (see section 5.3). Precision measurements up to $-1\,\mathrm{kV}$ can be performed.

- 500:1 allows precision measurements up to $-10\,\mathrm{kV}$.

- 2000:1 is the main voltage tap for the standard KATRIN operation at $-18.6\,\mathrm{kV}$.

- 4000:1 can be used up to $-35\,\mathrm{kV}$, e.g. for calibration measurements with Kr-83m (see chapter 6).

In addition, a secondary divider chain is installed, which consists of parallel circuits of resistive and capacitive impedances. This so-called control divider protects the K65 against HV transients by working as a high-pass filter. As the divider is designed for DC operation, this secondary chain additionally results in the reduction of high-frequent noise, e.g. the $50\,\mathrm{Hz}$ power line hum.

Figure 5.3 shows a picture of the K65 HV divider. The resistors are arranged in a helix structure between copper electrodes, which create a homogeneous electric potential. The five upper planes are equipped with the 165 precision resistors and the lowermost plane contains the tap resistors. A stainless steel vessel covered by
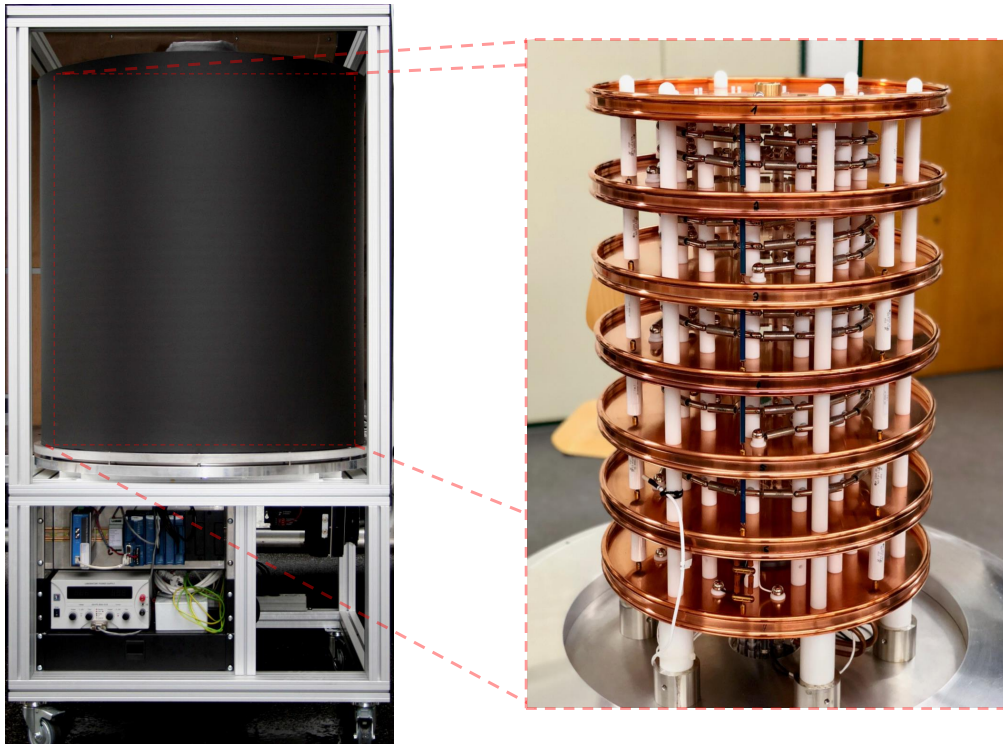
Figure 5.3: Image of the K65 HV divider. Left: The divider is surrounded by a stainless steel vessel and thermal insulation material. In the lower left area the SlowControl system is installed, which ensures the thermal stabilization. Right: Image of the actual HV divider consisting of a resistor chain arranged in a helix structure between copper electrodes, creating a homogeneous electric field for all resistors.

thermal insulation material shields the divider against electromagnetic radiation and environmental influences. A SlowControl system ensures a temperature stabilization to $25\,°C$ with $±0.1\,°C$ accuracy during operation. The vessel is filled with pure nitrogen, which works as isolating gas and prevents corrosive processes caused by air humidity. Temperature- and humidity-sensors are installed at multiple locations at the divider and record the environmental conditions within and outside of the vessel. The input voltage is applied to the top and the scaled output voltage can be measured at the bottom of the divider.

5.2 Repair and upgrade of the K65 voltage divider

During calibration measurements in 2015, an instable and unusual behavior of the K65 was discovered. The scale factor values obtained with the low-voltage calibration (see section 5.3.2) showed ppm-deviations and the HV divider was sensitive to mechanical vibrations. After extensive checks of the cabling and the

used calibration devices like DVMs, reference dividers etc. it was confirmed, that these problems originated from the K65 itself. In fact, even small movements of the device resulted in scale factor changes on the 10^{-2} level, which lead to the assumption of problems in one or multiple regions of the resistor chain.

In the past, similar problems were observed for the K65 (see [47]), which originated from loose connections of the resistors in their holding structures. This was fixed by tightening the screws, which attach the connection wires to the so-called T-elements between two neighboring resistors. Figure 5.4 shows two of these elements next to the resistors. The connection wires are fixed with headless screws. Loose screws could lead to an insufficient electrical connection, resulting in an unstable scale factor which reacts to mechanical influences. Therefore, the HV divider was opened and the screws of all 165 precision- and 14 tap resistors were checked. No loose connections were found. Since no other reason explaining these instabilities was identified (e.g. a broken feed through, plug connector etc.), the resistors were carefully examined. It was discovered, that multiple ones were loose and rotatable, revealing that the connection was not intact. Since the screws were tight, this indicated, that the connection wires were broken.

Therefore, the complete HV divider with all resistors was disassembled in order to investigate the status of the connection wires. One of the damaged wires after
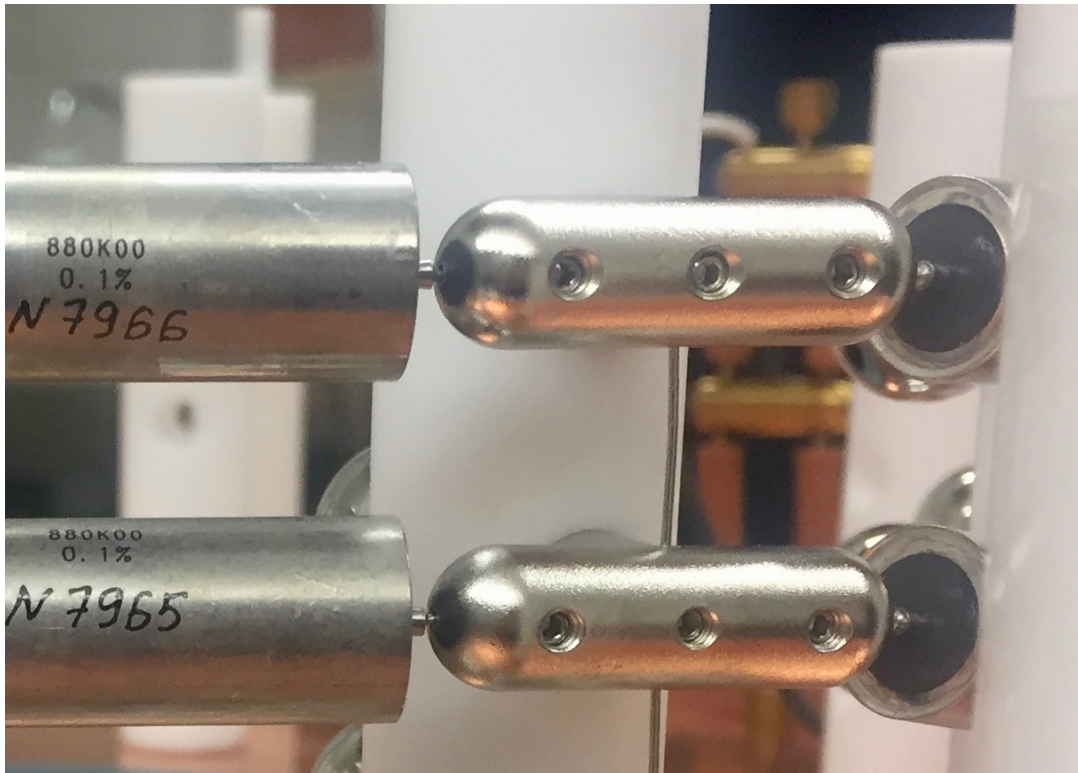

Figure 5.4: Closeup view of a part of the precision resistor chain of the K65. Two neighboring resistors are connected via so-called T-elements, where the connection wires are attached with headless screws.

the disassembly is shown in the left picture of figure 5.5. In this case, the wire was not cut, but highly deformed. Various resistors showed this problem, and multiple ones also featured a cut wire.

These connections of the concerned resistors were restored by the laser-welding technique. Extensions made from the original wire were welded directly to resistors, in order to avoid contact voltages caused by different materials. One example of a laser-welded wire is shown in the right picture of figure 5.5. This technique was preferred compared to soldering, since it heats the affected area only locally. Thus, the risk of damaging the resistors is minimized.

After all connection wires were restored, an improvement of the holding structure was developed. Since the damage to the wires was most likely caused by the headless screws, or respectively their tightening, a direct contact between the screw and the connection wire was avoided. Hence, the wires are not directly inserted into the connecting T-element, but within a metallic tube, such that the screw crimps the tube to the wire. In the original design, the opening for the wires of the T-elements was too small, prohibiting the insertion of an additional tube. Therefore, all pieces were rebored to a 2 mm opening. Furthermore, as many resistors featured a shortened connection wire not extendable by laser-welding, additionally a second hole was bored into the elements to account for the shortened wires. The concept of this repair plan is shown schematically in figure 5.6.

It was investigated, which material is suitable for the tubes. Since in the new configuration the electric connection of the resistors is realized via the tubes, the material must have a high conductivity. Furthermore, it has to be flexible enough, that crimping is possible. Finally, since the vessel of the HV divider
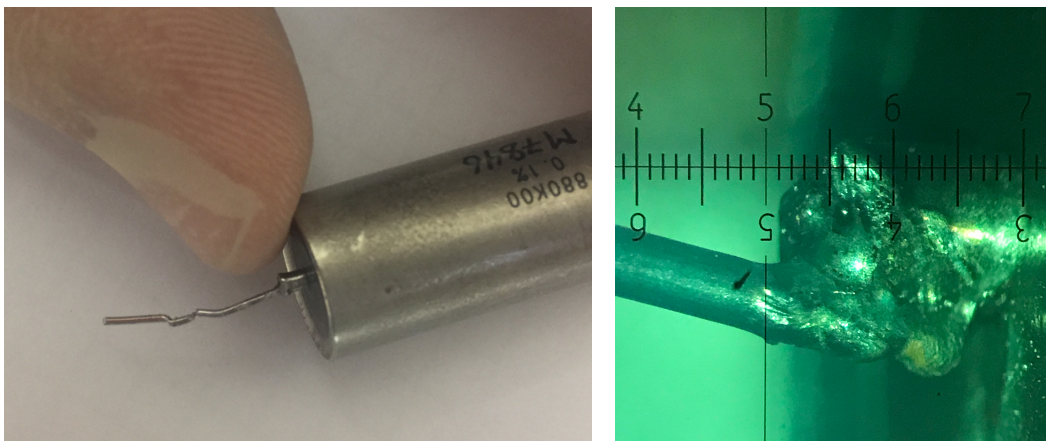

Figure 5.5: Left: Picture of a dismounted resistor. The connection wire, which was fixed with a headless screw in the connecting T-element, shows a high grade of deformation. Right: Micoscropic picture of laser-welded extension for a resistor with a cut connection wire.
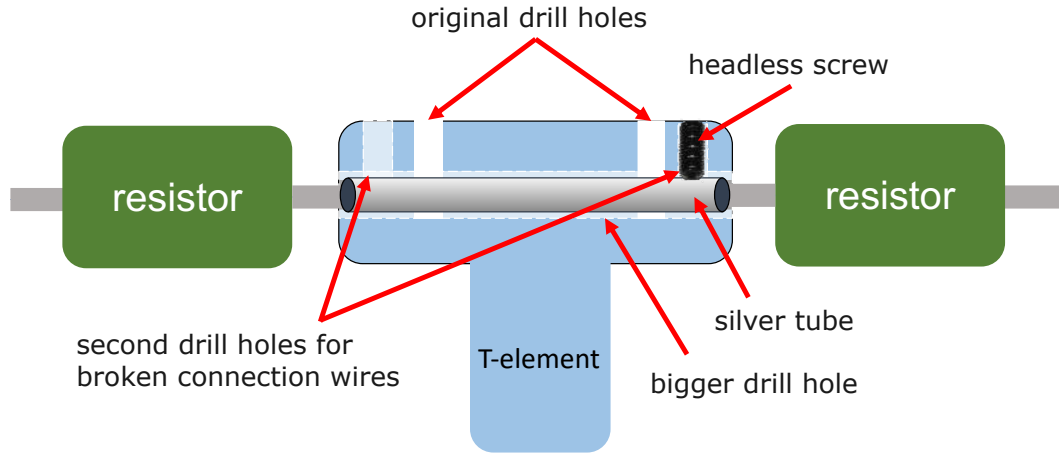
Figure 5.6: Schematic overview of the repair plan for the K65 HV divider. The connection of the wires via the T-elements is done with silver tubes, which are crimped to the wires with headless screws. Two additional drill holes had to be bored into the T-elements, since many resistors feature a shortened connection wire.

is filled with nitrogen gas, the material should not react chemically with this substance. An element fulfilling all these requirements is silver. It features one of the highest conductivities of all noble metals [95] and is much cheaper compared to gold. Additionally, as silver is not susceptible to oxidation processes triggered by environmental humidity, there is no danger of silver oxide generation at the tubes, influencing their conductivity. Instead, silver reacts chemically with sulfur from the atmosphere. However, since the vessel of the K65 is a closed volume filled with dry nitrogen gas, sulfidizing is not expected to be a problem. This assumption is supported by [96] and [97]. Figure 5.7 shows exemplary pictures of the modified T-elements and the acquired silver tubes.

After the modification of all parts, the HV divider was reassembled. For continuity reasons and in order to be comparable to past calibration measurements, all resistors were arranged in the same order. Figure 5.8 shows a closeup picture of a part of the reassembled resistor chain. Test measurements with the repaired K65 showed, that the scale factors are stable on the ppm-level and do not deviate significantly to previous calibration results (see next section). The whole repair process was done in cooperation with H.-W. Ortjohann and D. Winzen[1].

While the HV divider was shut down and dismounted, also a SlowControl system upgrade was performed, as the temperature stabilization was controlled by an expiring National Instruments (NI) compactFieldpoint module. The new system consists of a NI cRIO 9063 controller with the following components:

- NI 9216 RTD Analog Input Module: readout of temperature sensors

- NI 9221 Analog Input module: readout of the humidity sensors and the HV applied to the control divider

---

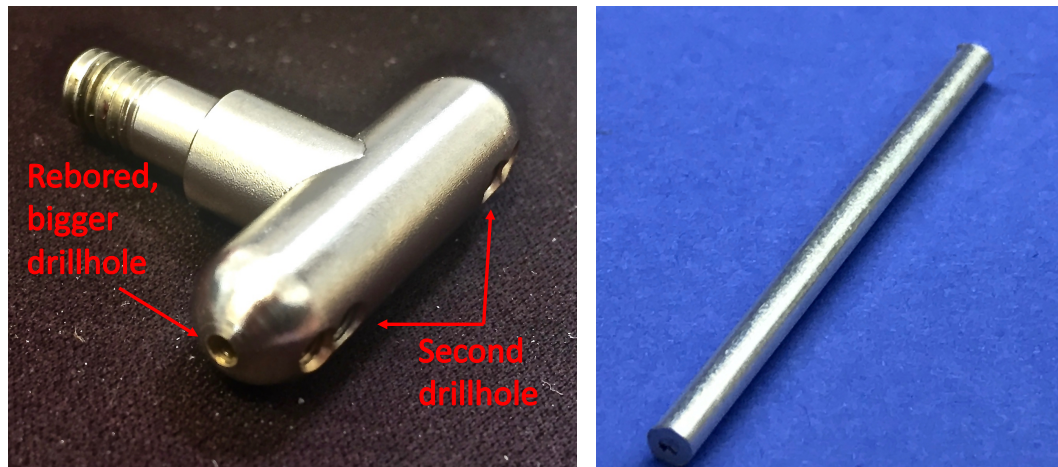[1]Insitut für Kernphysik, Westfälische Wilhelms-Universität Münster

Figure 5.7: Left: Modified T-element with two additional drill holes and a rebored bigger hole for the silver tubes. Right: One exemplary silver tube. In total, over 160 of these tubes were installed in all connecting T-elements of the K65.
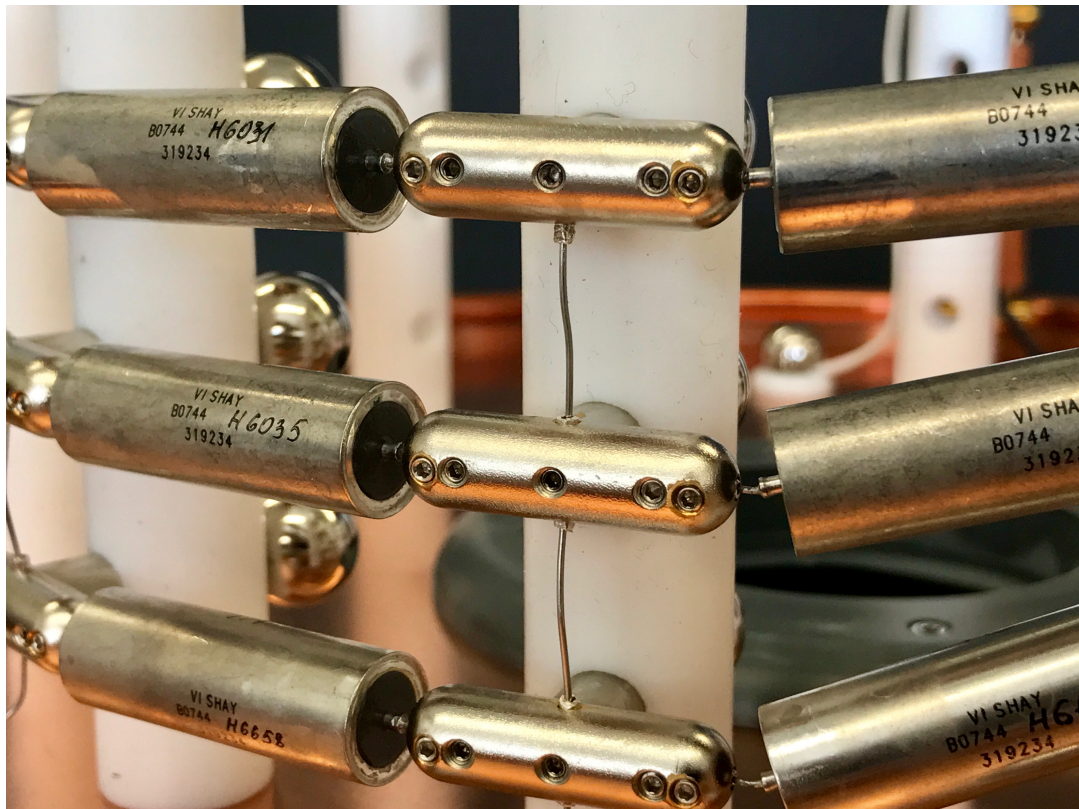

Figure 5.8: Closeup view of the reassembled K65 HV divider. The T-elements were modified with two additional drill holes. The silver tubes were also used for the fixation of the parallel connection wires of the T-elements, realizing different voltage taps.

- NI 9263 Analog output module: regulation of a power supply which is used for heating as part of the PID controlled temperature stabilization system.

A detailed overview of a comparable setup of the SlowControl system with the same components for a different HV divider is given in [90].

5.3 Former calibration methods

The calibration of HV divider scale factors requires the precise knowledge of its input- (U_{in}) and output (U_{out}) voltages. At KATRIN, the retarding potential has to be monitored with a precision of 3 ppm over a measurement period of 2 months. This implicates, that the scale factors have to be known to the ppm-level as well, requiring calibration measurements, where the input- and output voltages of the divider are known with ppm-precision.

For U_{out} this does not pose a problem, since it can be directly measured with a calibrated precision DVM to the sub-ppm-level. Usually, the desired output voltage is about 10 V, since this can be compared to a reference voltage source (see section 3.3).

The determination of the input voltage with this level of precision is the challenging part of the calibration. In the next subsections, different standard calibration methods for HV dividers are discussed. With these methods, the K35 & K65 were calibrated over the last years (see [36, 47]). Two new ideas and techniques, which were developed in the context of this thesis, are presented subsequently in this chapter and in chapter 6.

In order to calibrate the scale factor M_{A} of a HV divider, the general idea is to apply a calibration input voltage U_{HV} and measure the output voltage U_1 with a precision DVM. In the ideal case, the input resistance of a DVM is infinitely high. However, in reality the input resistance of the DVM $R_{\text{in,DVM}}$ (in the 100 GΩ to 1 TΩ range for high-end DVMs) has to be more than a million times larger than R_{LV} to determine the scale factor with ppm precision. Otherwise, the scale factor has to be corrected for $R'_{\text{LV}} = R_{\text{LV}} || R_{\text{in,DVM}}$. The input voltage has to be determined with a reference HV divider with the well known scale factor M_{B} and a second precision DVM measuring its output voltage U_2:

$$U_{\text{HV}} = M_{\text{B}} \cdot U_2. \tag{5.4}$$

This setup is shown schematically in figure 5.9. Following equation (5.1) and equation (5.4), the scale factor of the unit under test can be calculated to be

$$M_{\text{A}} = \frac{U_2 \cdot M_{\text{B}}}{U_1}. \tag{5.5}$$

For the reference divider with the well known scale factor M_{B} two options are available, which are discussed in the following sections.
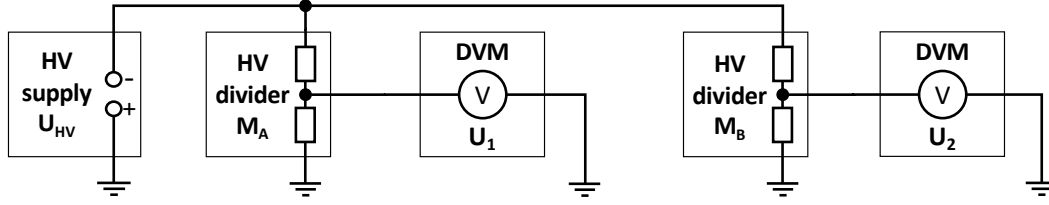
Figure 5.9: Connection scheme for the calibration of a HV divider with a HV supply (U_{HV}) and a precision DVM to measure the output voltage U_1 of the scale factor M_{A}. A reference HV divider with well known scale factor M_{B} is connected to the same HV source. In combination with a second precision DVM (U_2) it is used to determine the input voltage U_{HV}. For high voltages, this is only possible at metrology institutes like PTB with the required precision on the ppm-level. With commercial equipment, this procedure is limited to 1 kV.

5.3.1 High-voltage calibration

The general procedure of the high-voltage calibration (HVC) is to use a second HV divider with a well known scale factor as reference, in order to determine the input voltage. Since there are no commercially available devices with the required ppm-precision, for the K35 and K65 the only possible calibration can be performed at the German national metrology institute "Physikalisch-Technische Bundesanstalt" (PTB) in Braunschweig. The reference HV divider of PTB for this kind of calibrations is the MT100 [81], whose setup was the model for the K35 and K65. With a measurement setup as shown in figure 5.9, the scale factor of the unit under test is given by

$$M_{\mathrm{A}} = \frac{U_2 \cdot M_{\mathrm{B}}}{U_1} = \frac{U_2 \cdot M_{\mathrm{MT100}}}{U_1}. \tag{5.6}$$

Depending on the (multiple) scale factor(s) of the reference unit, this procedure can be done for arbitrary values of M_{A}. The main advantage of this method is, that the calibration is directly performed at high voltages. As explained in section 5.1, scale factors usually show a voltage- and temperature dependent behavior. By calibrating the HV divider at the HV potential where it is intended to be operated, these effects are included in the calibration.

The main disadvantage is, that this method can only be performed at PTB or comparable specialized metrology institutes. Since this requires a transport to Braunschweig and the absence of the HV divider for several weeks, it is not a suitable solution for the longterm operation at KATRIN. Additionally, by transporting the HV dividers with a car always the risk of damaging the devices is given, which should be minimized. Another disadvantage of the HVC at PTB is, that it relies on the calibration of the MT100, which is not completely traceable. Since the comparison of the entire divider with a known reference on the sub-ppm-level is not possible at high voltages, the voltage dependency is proven at the nominal voltage of each resistor. Overall, the MT100 is assumed to

have a negligible voltage dependency within the uncertainty of the scale factors of 2 ppm, mainly caused by the lack of traceability for the whole system.

The last calibration measurements at PTB were conducted in 2013 for the K35 and 2011 for the K65 HV divider. During the calibration measurements in 2013 at PTB, the K65 was instable and therefore could not be calibrated (see [47] for details). The obtained values for all scale factors are given in [36] and [47].

5.3.2 Low-voltage calibration

The general idea of the low-voltage calibration (LVC) is similar to the HVC. The difference is, that instead of a reference divider of a metrology institute commercially available devices are used. These HV dividers with (sub)ppm-precision, e.g. a Fluke 752A, are limited to the operation voltage of maximal 1 kV. The mentioned devices by Fluke offer a special built-in self calibration procedure based on a Wheatstone Bridge, resulting in an uncertainty of 0.5 ppm for the 100:1 scale factor [98]. The basic setup for the LVC is equal to the one presented in the previous section, shown in figure 5.9, where the role of the reference divider M_{B} is taken by the commercial device and the scale factor of the unit under test is given by

$$M_{\mathrm{A}} = \frac{U_2 \cdot M_{\mathrm{B}}}{U_1} = \frac{U_2 \cdot M_{\mathrm{Fluke\ 752A}}}{U_1}. \tag{5.7}$$

Figure 5.10 shows the calibration history of the K65 100:1 scale factor over the
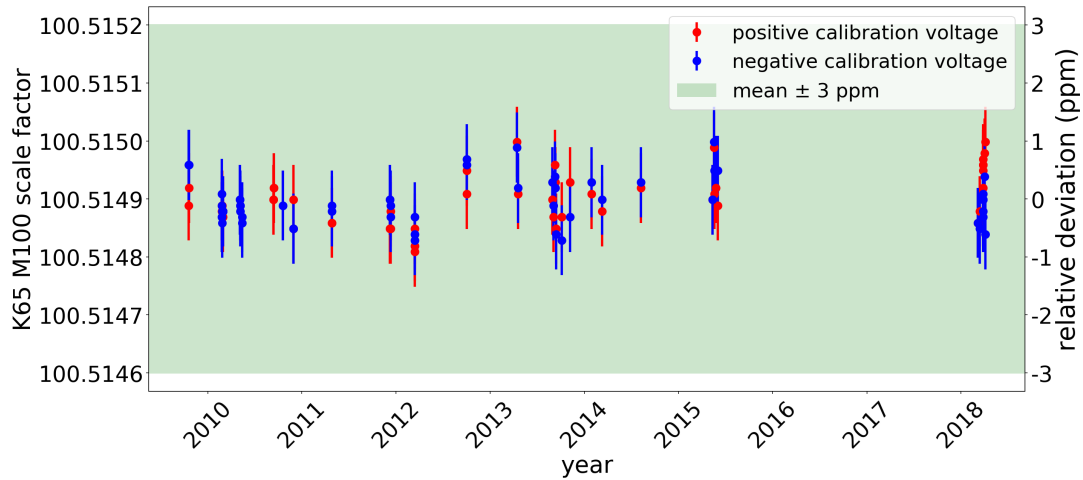

Figure 5.10: Low-voltage calibration of the K65 100:1 scale factor over the last years. The scale factor is stable on the ppm-level, which is illustrated by the green shaded area, indicating the KATRIN limitation of ±3 ppm for the uncertainty of the HV measurement. For the individual calibrations, an uncertainty of 0.58 ppm was assumed [36].

last years. For this and all other calibration results presented in this chapter, the obtained values after 2014 were determined in the context of this thesis. From the end of 2015 to 2017, the K65 was disassembled and repaired (see section 5.2). The overall uncertainty of 0.58 ppm [36] for the LVC results from the uncertainties of the three used devices: two DVMs and one reference divider. The measurements show, that the scale factor is stable over more than 8 years, with no visible drift within the uncertainties. The green shaded area indicates the KATRIN limitation for the HV uncertainty of 3 ppm, which is outperformed by the K65. The data also proofs, that the repair of the K65 was successful and the modifications to the system (e.g. using silver tubes as contacting material in the holding structure, see section 5.2) did not change the scale factor.

Since this method is limited to 1 kV, only scale factors up to 100:1 can be calibrated this way. For higher scale factors, the output voltage would be below the desired value of 10 V, losing one order of magnitude resolution of the precision DVM.

A standard procedure to avoid this problem is the step-up technique, performed with commercial LVC equipment. The prerequisite to apply this method is that the HV divider under test has multiple scale factors, one of them ideally scaling $M_A \approx 100{:}1$. In the first step, M_A has to be calibrated according to the procedure for 100:1 scale factors mentioned above. In a second step, the higher scale factor M_A' is calibrated by applying U_{HV} not to the regular divider input, but to the M_A output connection. By this configuration, the voltage drop over the low voltage resistors R_{LV} at a calibration voltage $U_{HV} \leq 1$ kV is comparable to the voltage drop over the resistors at an input HV of $U_{HV} \cdot M_A$. The output voltage at M_A' is measured with a precision DVM (U_1). As before, U_{HV} is measured with a reference HV divider (M_B) and a second precision DVM (U_2). The connection scheme of this method is shown in figure 5.11.
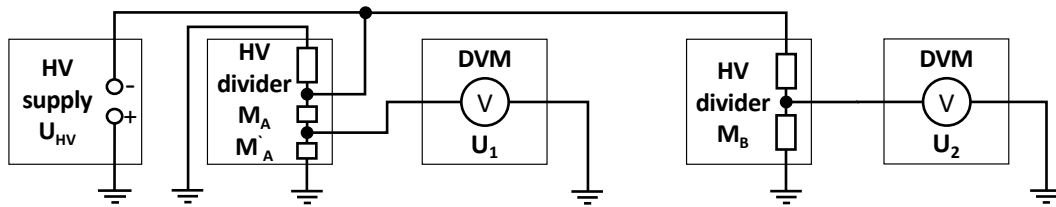

Figure 5.11: Connection scheme for the calibration of a HV divider with the two scale factors M_A and $M_A' > M_A$. Here the voltage created by a HV supply is not connected to the input of the unit under test, but to the scale factor M_A output connection. The scaled voltage U_1 is measured with a precision DVM at M_A'. A reference HV divider with scale factor M_B and a second DVM (U_2) are used to determine the input voltage.

For the calculation of M'_A, the determined input voltage has to be multiplied with M_A:

$$M'_\mathrm{A} = \frac{U_2 \cdot M_\mathrm{B}}{U_1} \cdot M_\mathrm{A} = \frac{U_2 \cdot M_\text{Fluke 752A}}{U_1} \cdot M_\mathrm{A}. \tag{5.8}$$

As M'_A depends on the previously determined scale factor M_A, the uncertainty is increased to be $\Delta M'_\mathrm{A} = 0.8\,\mathrm{ppm}$.

One disadvantage of this method is, that the upper part of the divider chain with the resistors R_i is not loaded with the correct voltage $M_\mathrm{A} \cdot U_\mathrm{HV}$. This means, that the voltage dependency of the scale factor M_A is not determined and included in the analysis properly. For a completely traceable calibration of a HV divider, the voltage dependency of the scale factors has to be taken into account correctly.

Figure 5.12 shows the calibration results for the 2000:1 and 4000:1 scale factors of the K65 over the last years. The spread of the calibration results is well within the KATRIN limit of $3\,\mathrm{ppm}$, proving that the K65 is stable on the (sub)ppm-level over years. Again, the calibration values obtained in 2018 confirm the success of the repair of the K65. The result regarding the stability of the K65 is in agreement with previous measurements, presented in [72].

The LVC was also performed with the K35 regularly over the last years. However, as this divider was used at KATRIN for measurements since 2015, there are no further low-voltage calibration values after this. The calibration histories for the 100:1, 2000:1 and 4000:1 scale factors are shown in figure 5.13. Similarly to the K65 result, the data demonstrates, that the K35 outperforms the KATRIN requirement, as the spread of the calibration values is smaller than $\pm 3\,\mathrm{ppm}$. No LVC was performed with the K35 after 2015, but the HV divider was calibrated with a novel calibration method based on mono-energetic conversion electrons of Kr-83m in 2017, which is presented in chapter 6.

5.4 Motivation for a novel absolute calibration method

Although in the last years ppm-precise calibration measurements were performed with the two described methods of LVC and HVC, multiple disadvantages – summarized in this section – motivated the development of a new independent calibration method. The main problem in this context is the disregard of the scale factors voltage dependency $M = M(U)$, originating from thermal effects and leakage currents with respect to different voltage ranges and powers as described in section 5.1. Hence, calibration values obtained at low voltages can not be considered for higher voltages without corrections.
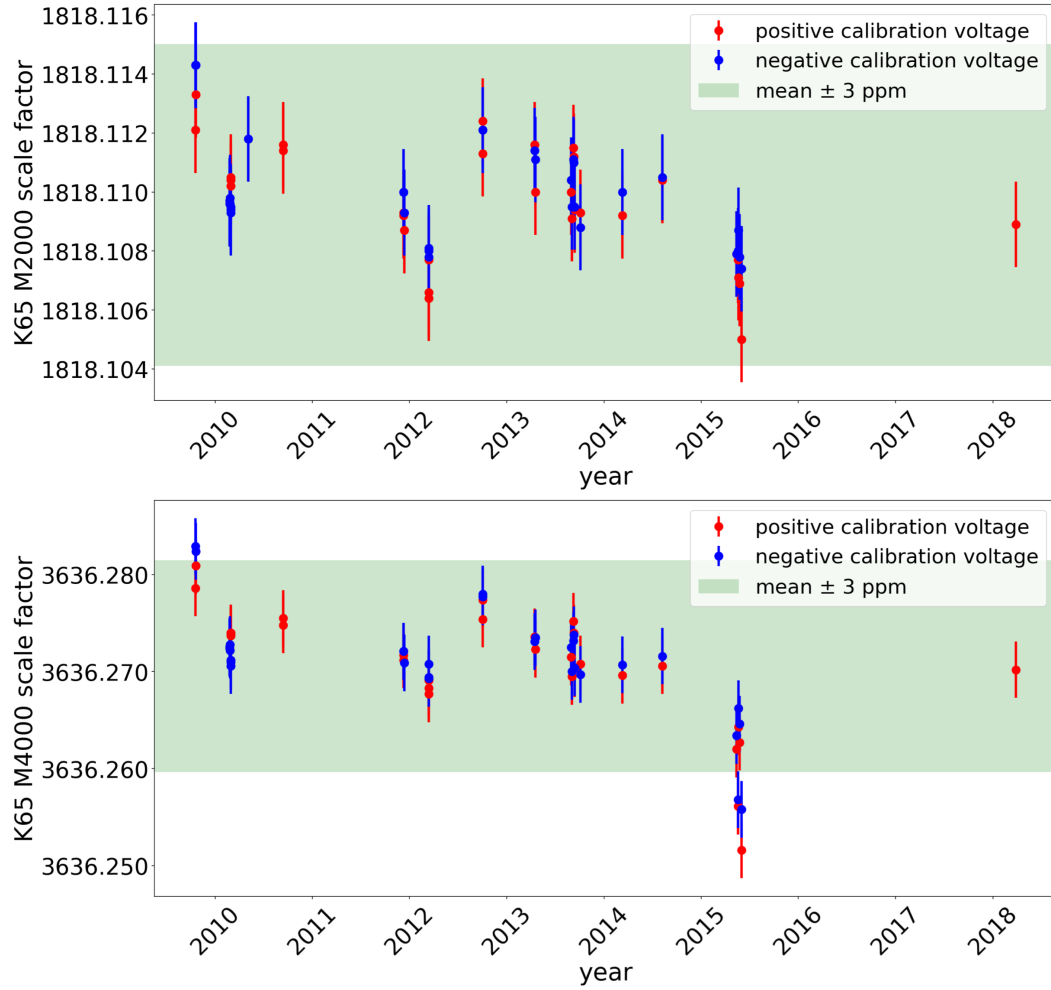
Figure 5.12: Low-voltage calibration of the K65 2000:1 and 4000:1 scale factors over the last years. The scale factors are stable on the ppm-level, which is illustrated by the green shaded area, indicating the KATRIN limitation of 3 ppm for the uncertainty of the HV measurement. The points exceeding this limit in 2015 were taken shortly before the repair of the K65 and are assumed to be caused by the problems mentioned in the previous section. For the individual calibration measurements an uncertainty of 0.8 ppm was assumed.

The HVC requires a second precision HV divider as reference. As only the MT100 HV divider of the PTB provides a sufficiently high precision, time consuming and possibly dangerous transports from Karlsruhe to Braunschweig are necessary, which are not compatible with the time schedule of KATRIN. Besides this issue, also a more general problem is given by the fact, that there is no completely traceable calibration of the MT100 as discussed above.

For the LVC, the main problem is the calibration of scale factors larger than 100:1. This procedure is based on the initial calibration of the 100:1 scale factor
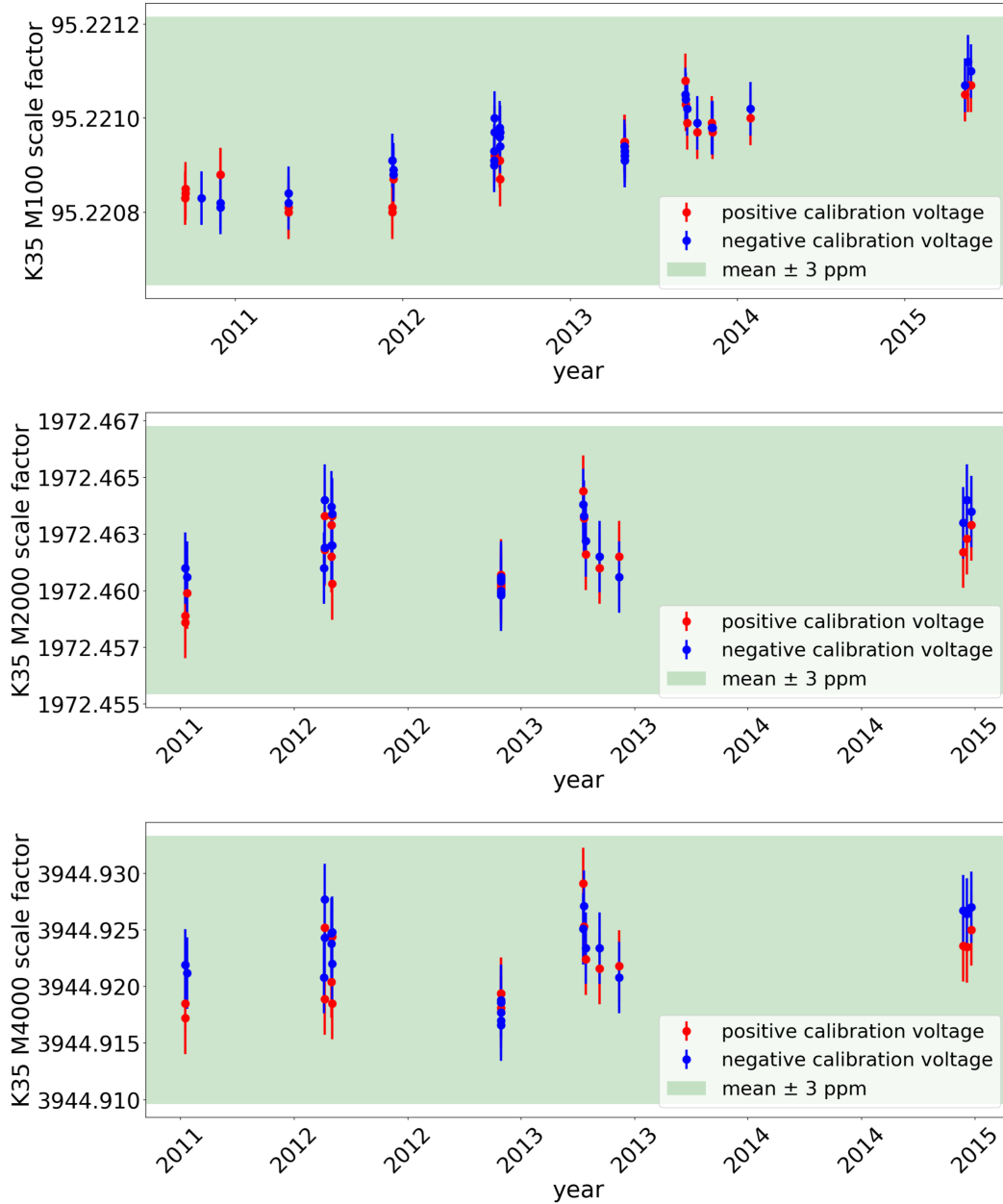
Figure 5.13: Low-voltage calibration of the K35 100:1, 2000:1 and 4000:1 scale factors over the last years. The scale factors are stable on the ppm-level, which is illustrated by the green shaded area, indicating the KATRIN limitation of 3 ppm for the uncertainty of the HV measurement. For the individual calibration measurements an uncertainty of 0.58 ppm (0.8 ppm) was assumed for the 100:1 (2000:1 & 4000:1) scale factor.

at 1 kV, and this value is applied for higher input voltages without corrections, neglecting the voltage dependency. Hence, for all the calibration values obtained with the LVC it has to be concluded, that they are not completely comparable to the ones obtained with the high-voltage calibration. However, although the

absolute values can be affected by additional uncertainties, the observation of relative deviations of the system is a valuable indicator for the status and condition of HV dividers.

Recently, a new method for an absolute calibration of HV dividers was reported in [99], where uncertainties in the range of 5 ppm were achieved. However, this procedure requires a complex experimental setup, featuring an ion beam line with a laser spectroscopy setup, making the method very difficult to apply.

In the following, a novel method for absolute calibrations of HV dividers to the ppm-level by measuring a traceable differential scale factor under HV conditions is discussed, which can be performed with commercially available equipment. The next sections give an overview over the idea of the newly developed calibration method and the technical realization. Subsequently, measurement results with achieved uncertainties of about < 1 ppm is presented.

5.5 Idea of the novel absolute calibration method

The basic idea of the novel absolute calibration method was developed by C. Weinheimer (Institut für Kernphysik, Westfälische Wilhelms-Universität Münster) and is based on the determination of the voltage dependency of the scale factors of a HV divider by measuring a differential scale factor directly at high voltages with commercially available equipment. This is especially important for scale factors up to 100:1, since they are used in the step-up technique to calibrate higher scale factors (see section 5.3.2).

As defined in equation (5.1), the scale factor is the possibly voltage dependent factor between the input- and output voltage of a HV divider. For a given input voltage the corresponding output voltage can be approximated by a Taylor expansion around $U_{\mathrm{HV}} = 0$:

$$U_{\mathrm{LV}} = a \cdot U_{\mathrm{HV}} + b \cdot U_{\mathrm{HV}}^2 + c \cdot U_{\mathrm{HV}}^3 + d \cdot U_{\mathrm{HV}}^4 + ... \tag{5.9}$$

with the coefficients a, b, c and d (neglecting higher orders). The necessary number of orders of magnitudes of the Taylor expansion depends on the properties of the calibrated HV divider (see discussion in section 5.7). For the voltage independent case, the parameters b, c and d are zero and a is the inverse of the constant part of the scale factor M_0:

$$a = \frac{1}{M_0}. \tag{5.10}$$

For the realistic case of a voltage dependent scale factor, equation (5.1) and equation (5.9) yield:

$$M = \frac{1}{a + b \cdot U_{\mathrm{HV}} + c \cdot U_{\mathrm{HV}}^2 + d \cdot U_{\mathrm{HV}}^3}. \tag{5.11}$$

The differential scale factor $\widetilde{M}$ can be defined as the derivative of U_{HV} with respect to U_{LV} at U_{HV}:

$$\widetilde{M} = \left. \frac{\delta U_{\mathrm{HV}}}{\delta U_{\mathrm{LV}}} \right|_{U_{\mathrm{HV}}} = \frac{1}{\left. \frac{\partial U_{\mathrm{LV}}}{\partial U_{\mathrm{HV}}} \right|_{U_{\mathrm{HV}}}} = \frac{1}{a + 2 \cdot b \cdot U_{\mathrm{HV}} + 3 \cdot c \cdot U_{\mathrm{HV}}^2 + 4 \cdot d \cdot U_{\mathrm{HV}}^3}. \tag{5.12}$$

The measurement of $\widetilde{M}$ at U_{HV} is done with the following procedure: at certain input voltages, U_{HV} is increased by a small amount of δU_{HV} and the change of the output voltage δU_{LV} is measured. In the ideal case, the voltage increase δU_{HV} is infinitesimal small in order to determine the slope of the scale factor curve at U_{HV}. However, due to technical limitations and because of the ambition to trace the voltage measurement back to a $10\,\mathrm{V}$ reference, this is not possible. Hence, the voltage is increased by $\delta U_{\mathrm{HV}} = 1\,\mathrm{kV}$, which can be measured with traceable equipment with ppm-precision. Therefore, it is assumed in the following, that the determined scale factor is valid for the input voltage $U_{\mathrm{HV}} + \delta U_{\mathrm{HV}}/2$. The two cases of the constant and voltage dependent scale factor are sketched in figure 5.14. Additionally $\widetilde{M}$ is illustrated for an exemplary input voltage $U_{\mathrm{HV},0}$.

By measuring the differential scale factor for different input voltages, the coefficients a, b, c and d can be determined and used to calculate the scale factor M for any given input voltage.

5.6 Technical realization

The technical realization of the $\widetilde{M}$-measurement is split into two steps: figure 5.15 shows the experimental setup for the first step. A high voltage U_{HV} is connected to the HV divider whose scale factor M_{B} is to be calibrated. Its output voltage U_2 is measured with a precision DVM versus a ppm-stable counter voltage $U_{\mathrm{HV}}/M_{\mathrm{A}}$ – provided by a Fluke Calibrator 5720A – as a null volt measurement. By using a counter voltage instead of a measurement versus ground potential, it is ensured, that the measured voltage is below $20\,\mathrm{V}$, which can be traced back to a $10\,\mathrm{V}$ reference source. The counter voltage is directly determined with a third DVM (U_3). Since U_3 has to be ppm-stable but the absolute value does not need to be known precisely, it can be monitored with a 6.5 digit DVM of type Fluke 8846A. Another possibility is to convert U_3 via a reference divider like Fluke 752A into the 0 to $10\,\mathrm{V}$ range. Additionally, a second HV divider (M_{A}) is needed as reference for the unit under test, which is connected to the same HV source. The output voltage of the reference HV divider is also measured with a DVM

(U_1) versus the counter voltage. In this measurement, the ratio of the scale
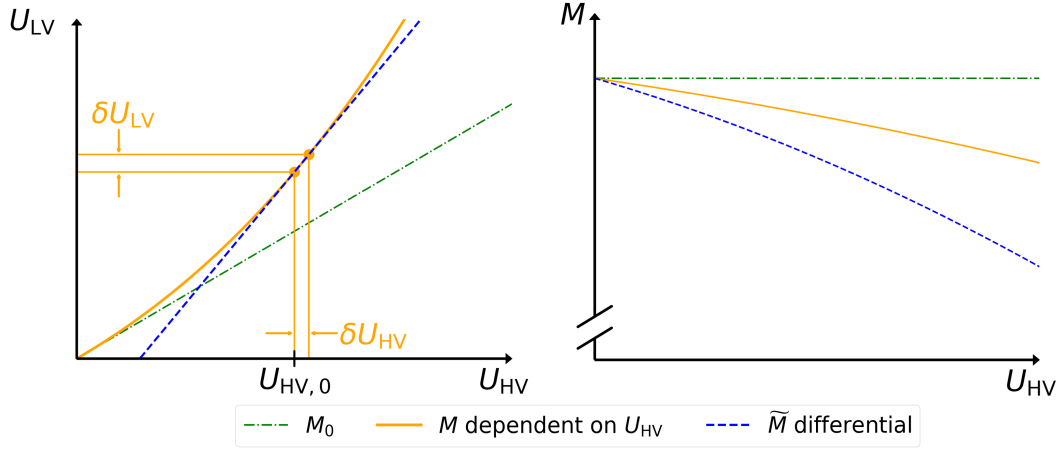

Figure 5.14: Illustration of scale factors as function of the input- and output voltages. Left: Output voltage as function of input voltage. Right: Scale factor as function of input voltage. A constant scale factor appears as a straight line. If the scale factor is dependent on the input voltage (see orange solid line), a deviation from the constant case is observed. For each input voltage U_{HV}, the differential scale factor is measured as a change of input- and output voltages. This is illustrated at the left at a certain input voltage $U_{\mathrm{HV,0}}$. The differential scale factor $\widetilde{M}$ appears as slope of the line through the two points $U_{\mathrm{HV,0}}$ and $U_{\mathrm{HV,0}}+\delta U_{\mathrm{HV}}$ (blue dashed line). M_0 notifies the scale factor derived at $U_{\mathrm{HV}} \approx 0$ (green dash dotted line).
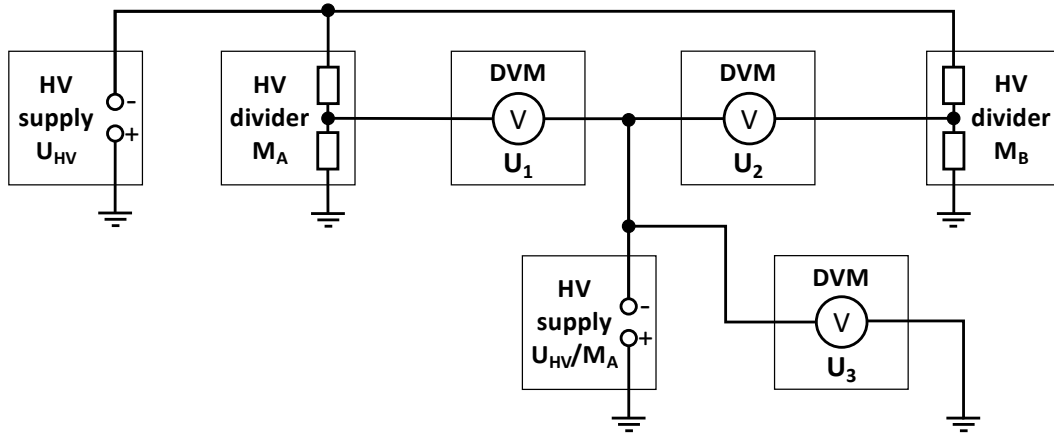

Figure 5.15: Connection scheme for the measurement of the ratio μ of the scale factors M_{A} and M_{B}. A HV U_{HV} is connected to both HV dividers and their output voltages are measured with two DVMs versus a counter voltage as a null volt measurement, which is monitored with a third DVM. The counter voltage labeled $U_{\mathrm{HV}}/M_{\mathrm{A}}$ is adjusted such that $U_1 \approx 0$.

factors μ

$$\mu := \frac{M_A}{M_B} = \frac{U_2 + U_3}{U_1 + U_3} \approx 1 + \frac{U_2}{U_3} \qquad (5.13)$$

can be determined applying Kirchhoff's circuit laws. The approximation on the right side of equation (5.13) is only valid for $U_1 \approx 0$ and should only illustrate that μ does not require a precise determination of U_3. This counter voltage is a key factor to achieve the ppm-precision for the novel absolute calibration method. The ratio μ can be measured with a short-term precision in the order of $< 10^{-7}$ without knowing the single scale factors M_A and M_B, since it only depends on the measured voltages $U_{1,2,3}$, which are determined with precision DVMs. Since both null volt measurements U_1 and U_2 are measured with the same counter voltage, both scale factors have to be of similar magnitude in order to not exceed the 10 V range of the DVMs.

In the second step, the input voltage of the HV divider under test is increased by δU_{HV}, which is generated and measured on top of the HV potential U_{HV} (see figure 5.16). The input voltage of the reference HV divider stays constant as well as the counter voltage, any potential change can be detected by continuously measuring U_1 and U_3. The DVM, which is used to measure the output voltage of the divider under test, measures a voltage increase of $\delta U_{HV}/\widetilde{M}_B$. According to Kirchhoff's circuit- and Ohm's laws, the differential scale factor is given by

$$\widetilde{M}_B = \frac{U_1 \cdot M_A + U_4 \cdot M_C}{U_2 + (1 - \mu) \cdot U_3}. \qquad (5.14)$$

As denoted in equation (5.14), the scale factor of the reference HV divider M_A is needed to calculate $\widetilde{M}_B$. However, the term $U_1 \cdot M_A$ is close to zero since U_1 is a null volt measurement against the stable counter voltage adjusted to $U_1 \approx 0$. Hence, the dominant factor of the numerator is $U_4 \cdot M_C$, which means, that the absolute value of M_A needs to be stable but does not have to be known precisely in order to calibrate the unit under test to the ppm-level. The measurements, which are presented in the next section, demonstrated, that a relative uncertainty of up to $1 \cdot 10^{-4}$ can be allowed for M_A, without changing the calibration result for M_B on the sub-ppm-level.

Utilizing this property, another HV divider, intended to be used as reference unit M_A, was built within the context of this thesis, featuring precision resistors with uncertainties in the $1 \cdot 10^{-5}$ range (see figure 5.17) [100]. It consists of 2×18 resistors ($30 \times 20\,\text{M}\Omega$ Caddock type USF 371 and $6 \times 1\,\text{M}\Omega$ Caddock type USF 370) connected in series and offers a scale factor of $M_A \approx 100 : 1$.

In order to characterize this new HV divider, its reproducibility and voltage dependency were measured with the K65 multiple times as shown in figure 5.18. The setup of the measurement is equal to the one shown in figure 5.9. The uncertainty of the measurement is dominated by the uncertainty of the K65 scale factor of about 1 ppm. A first measurement with voltages of 1 kV was performed in 2017. After that, over several month high-voltage measurements

were performed with the device, before the voltage dependency was investigated two times in 2018. The first measured absolute scale factor value (at 1 kV) deviates about 20 ppm compared to later calibrations. Since the resistors were acquired and used for the first time in 2017, this behavior was expected, as aging and conditioning effects occur especially in the first time of usage of these elements. The manufacturer specifies the shelf life stability to be better than 20 ppm year^{-1} [100].

For different calibration HV, a non-linear voltage dependency of below 10 ppm per measurement series was observed. This does not pose a problem for the novel absolute calibration method, since – as described above – uncertainties in the order of 100 ppm can be accepted for the scale factor.

More important than the absolute value is the stability of the scale factor within an absolute calibration measurement. This was investigated by measuring the scale factor at -18.6 kV as demonstrated in figure 5.19. The usual duration of a measurement in this context is in the order of 10 min. On this time scale, the new HV divider showed a stability on the $1 \cdot 10^{-7}$ level.

Finally, the uncertainty of U_3 in equation (5.14) is negligible, since the ratio of the scale factors μ is close to 1. Therefore, U_2 and its uncertainty are dominating
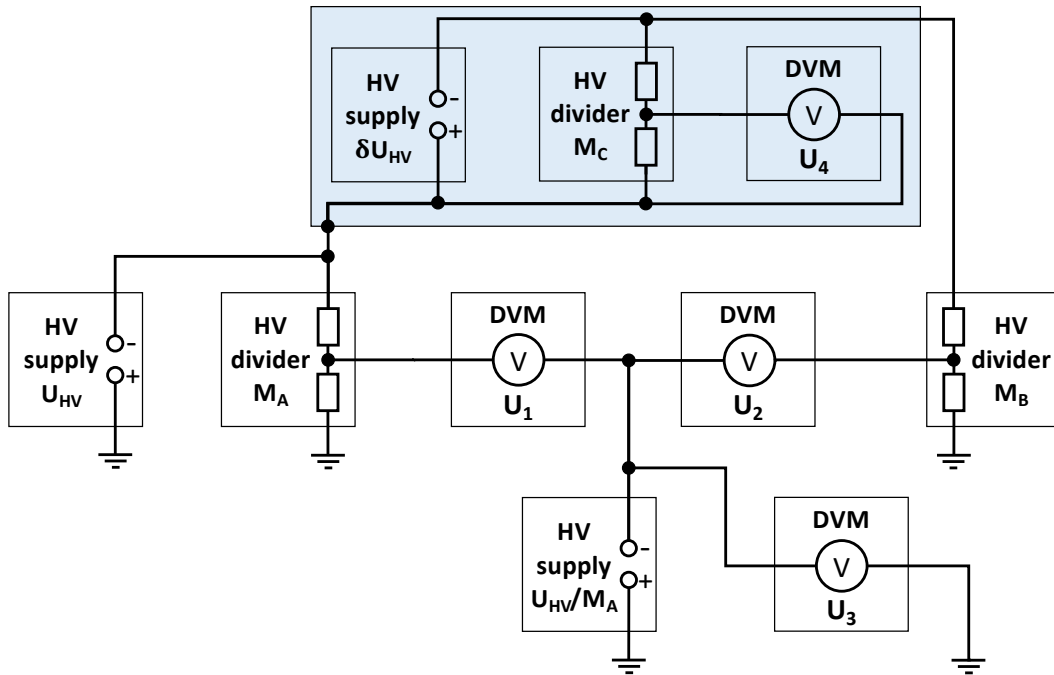

Figure 5.16: Connection scheme for differential scale factor measurement. On top of a high-voltage potential an additional calibration voltage is created, which is applied to the unit under test. The reference HV divider is unaffected by the calibration voltage. The devices in the blue shaded box are located in a HV cage and read out via an optical link.

the denominator for the determination of $\widetilde{M}_{\mathrm{B}}$.

During a measurement campaign in 2018, numerous calibrations of different HV dividers were performed. The main goal was to check the reproducibility and longterm stability of the newly developed absolute calibration method as well as its capability to measure the voltage dependency of scale factors. The calibration measurements were performed with two ppm-precise HV dividers: the K65 [72] and the G35 [91, 90], which was designed and built by D. Winzen[2] for measuring the acceleration voltage of the electron cooler at the heavy ion storage ring CRYRING at GSI. The design of the G35 is similar to the K35. In order to crosscheck the results, the two ppm-precise HV dividers and the newly built reference divider were used mutually as reference M_{A}.

Commercial HV dividers of type Fluke 752A – calibrated each day before the measurements – were used to measure the calibration voltage δU_{HV} up to $1\,\mathrm{kV}$. The voltage measurements were performed with 8.5 digit precision DVMs. In order to measure U_1, U_2 and U_4, the devices Fluke 8508A, Agilent 3458A and Keysight 3458A were used. For these devices, a precisely time-synchronized measurement is essential, since the voltage measurements are highly correlated and a delay of one or more devices would result in a wrong scale factor calcula-

---

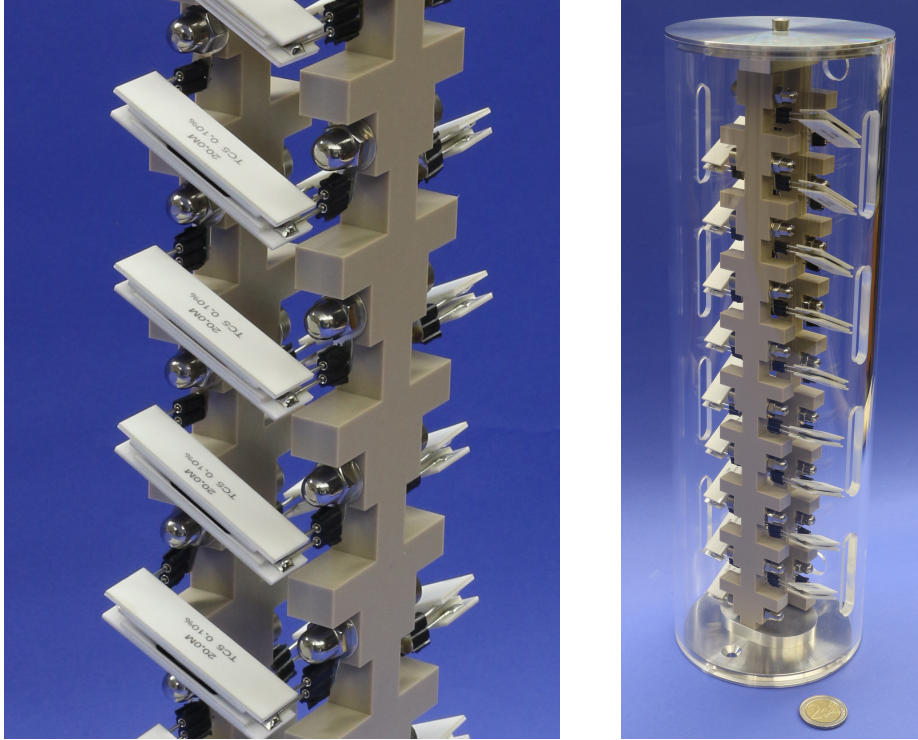[2]Institut für Kernphysik, Westfälische Wilhelms-Universität Münster

Figure 5.17: Pictures of the custom made HV divider consisting of two times 18 precision resistors connected in series. The scale factor $M_{\mathrm{A}} \approx 100 : 1$ has a relative uncertainty of about $10\,\mathrm{ppm}$.
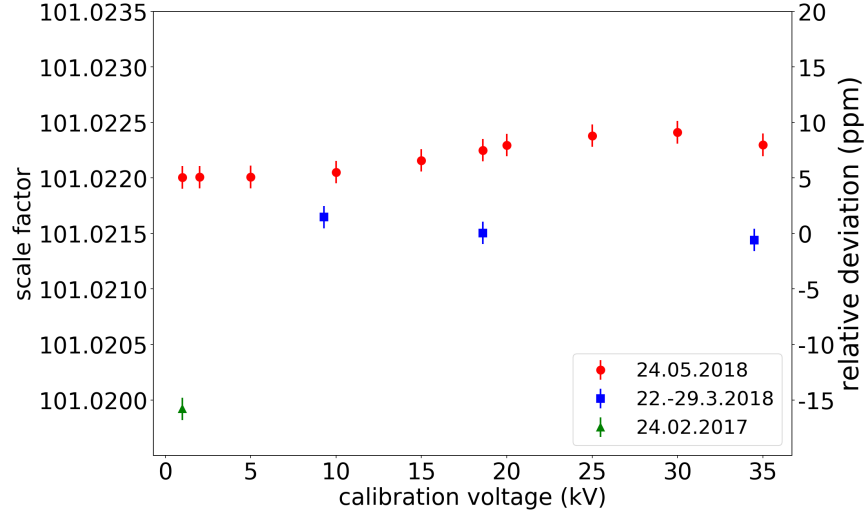
Figure 5.18: Voltage dependency of the newly built HV divider measured with the K65. Between the first measurement in 2017 and the other two measurement series, multiple (longterm) HV measurements were performed with the device. The uncertainties of about 1 ppm for each data point are dominated by the uncertainty of the K65.
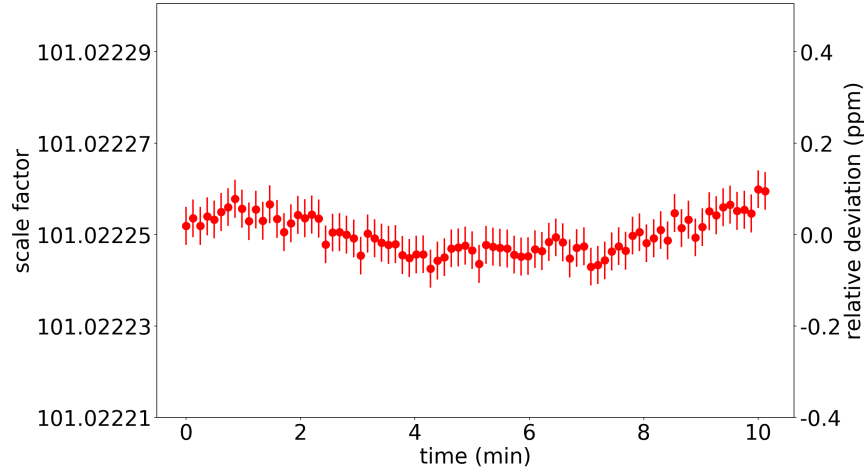

Figure 5.19: Short-term stability of the newly built HV divider measured at $-18.6\,\text{kV}$ with the K65. Here, only the standard deviation of the measurement is shown as statistical uncertainty, since the absolute value (affected by systematic uncertainties) is not relevant on the $1 \cdot 10^{-4}$ scale for the newly developed calibration method.

tion. The less critical voltage U_3 was monitored with a 6.5 digit DVM of type Fluke 8846A. The used HV source U_{HV} and the G35 HV divider are limited to 35 kV. For the operation of the devices on HV potential (Keysight DVM, HV divider M_C and the HV source δU_{HV}), an isolated cage identically to the one described in section 4.3, was used (see figure 5.20), which can be set on HV potential.

Figure 5.20: Picture of the custom-made HV cage. The inner cage can be operated on HV potential of up to 35 kV. The electrical devices within are supplied with power by an insulating transformer and controlled and read out via an optical link. In the right picture,the back-side of the cage can be seen, where the custom-made reference HV divider is installed.

5.7 Calibration results

The stability of the scale factor ratio-measurement was investigated as described in the previous sections. Figure 5.21 shows a single μ determination run consisting of 17 measurements before and 17 measurements after the determination of the differential scale factor $\widetilde{M}_{\mathrm{B}}$. In order to determine its mean value, which according to equation (5.14) is needed to calculate the differential scale factor, the data was fitted with a constant. As described in the previous section, the ratio can be determined with relative uncertainties smaller than 0.1 ppm without knowing the individual scale factors of both dividers.

Subsequently, $\widetilde{M}_{\mathrm{B}}$ was measured according to figure 5.16. The differential scale factor was derived with equation (5.14), including the calculated mean μ-value determined directly before and after the calibration measurement.
Figure 5.22 shows a single measurement of the differential scale factor. The standard deviation is below 0.5 ppm. The differential scale factor, always together with the ratio μ, was measured multiple times each day during the calibration campaign, agreeing well within uncertainties.
 In order to derive the real scale factor M_{B} from $\widetilde{M}_{\mathrm{B}}$, the differential scale factor was measured for different voltages up to $-35\,\mathrm{kV}$ (see figure 5.23 and figure 5.24) and the data was fitted with MINUIT according to equation (5.12) to obtain
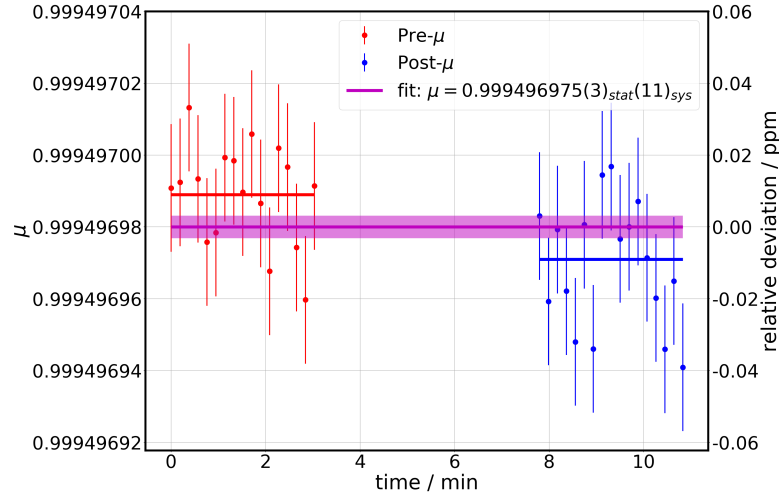
Figure 5.21: Exemplary measurement of the scale factor ratio μ of the unit under test (K65) and a reference HV divider (G35). As both scale factors are about 100:1, the ratio is close to one. The data was fitted with a constant to determine the mean value. The measurement was performed at $U_{\mathrm{HV}} = -18.6\,\mathrm{kV}$. Since the short-term uncertainties of the digital voltmeters are not known, the measured fluctuations were used to determine the uncertainties. Therefore, the error bars are scaled such, that the quadratic deviation per number of degrees of freedom is equal to one ($\chi_r^2 = 1$).
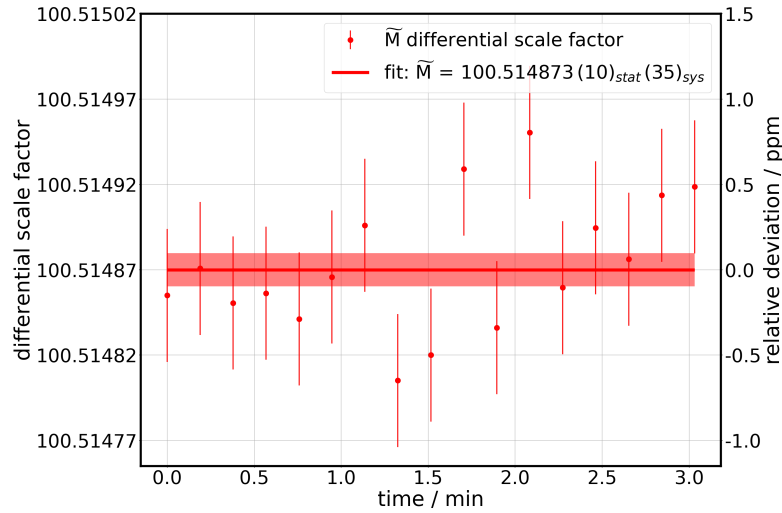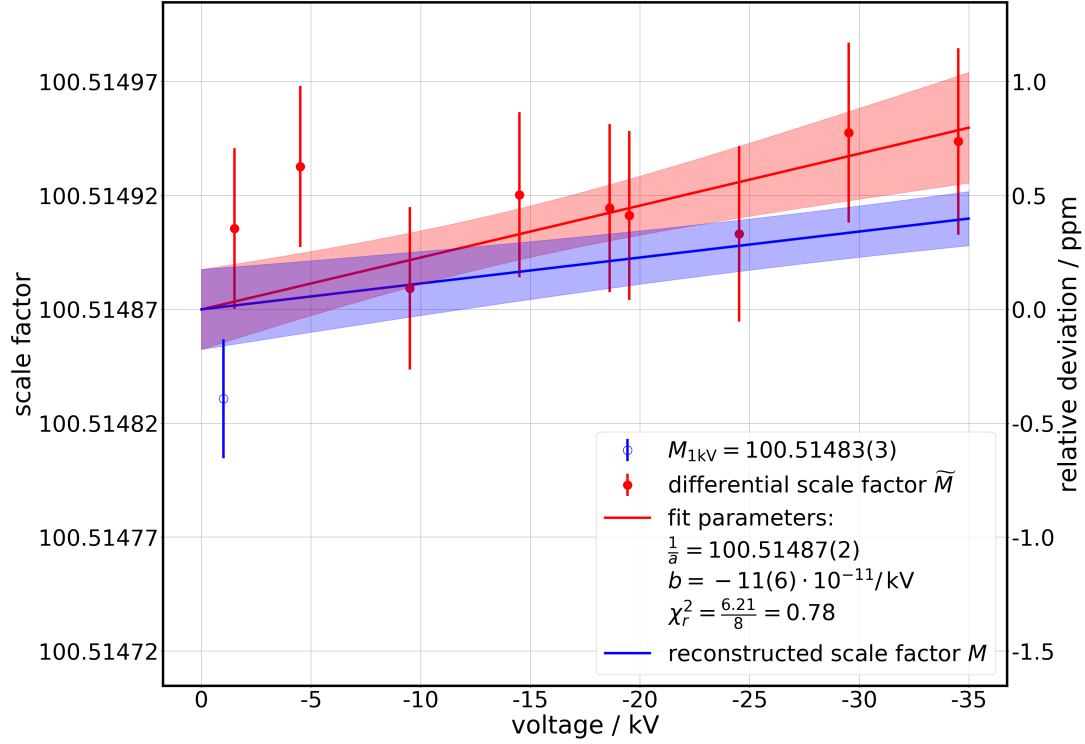

Figure 5.22: Exemplary measurement of the K65 differential scale factor determined with the newly developed absolute calibration method. The data was fitted with a constant to determine the mean value. The measurement was performed at $U_{\mathrm{HV}} = -18.6\,\mathrm{kV}$. Since the short-term uncertainties of the digital voltmeters are not known, the measured fluctuations were used to determine the uncertainties. Therefore the error bars are scaled such, that the quadratic deviation per number of degrees of freedom is equal to one ($\chi_r^2 = 1$).

Figure 5.23: Voltage dependency of the K65 100:1 scale factor determined with the newly developed absolute calibration method. The differential scale factors $\widetilde{M}$ measured at different voltages (red points) and the low voltage scale factor M_{1kV} (blue point) are fitted with a polynomial of first order (red line). The error-bars include the statistical and systematic uncertainties. The obtained coefficients are used to calculate the real scale factor M for a voltage range from 0 to $-35\,\text{kV}$ (blue line).

the coefficients a, b c, and d. Also the low voltage calibration values measured as described in section 5.3.2 (see setup in figure 5.9) were included into the analysis. Since in that measurements the real scale factor is determined at $1\,\text{kV}$, a combined fit was used to describe all data points. The fit function is a sum of equation (5.11) for the data point obtained with the low voltage calibration measurement and equation (5.12) for the data points of the differential scale factor determination. Subsequently, M_B is calculated using equation (5.11) with the determined coefficients. For the K65 HV divider, a negligible linearity $\leq 1\,\text{ppm}$ was observed, which is within the uncertainties in agreement with former calibration measurements at PTB [72]. Here, a linear voltage dependency $(c = 0 = d)$ was assumed for the fit, as indicated by χ^2-studies of higher orders.

The scale factor M_B derived this way for the G35 HV divider showed deviations of up to $3.3\,\text{ppm}$ at $-35\,\text{kV}$ compared to the low voltage scale factor M_{1kV}. This result was crosschecked by comparing the scale factor M_B of the G35 with the one measured directly with the K65 using a setup as shown in figure 5.9 two months earlier. As indicated in figure 5.24, the data agrees within
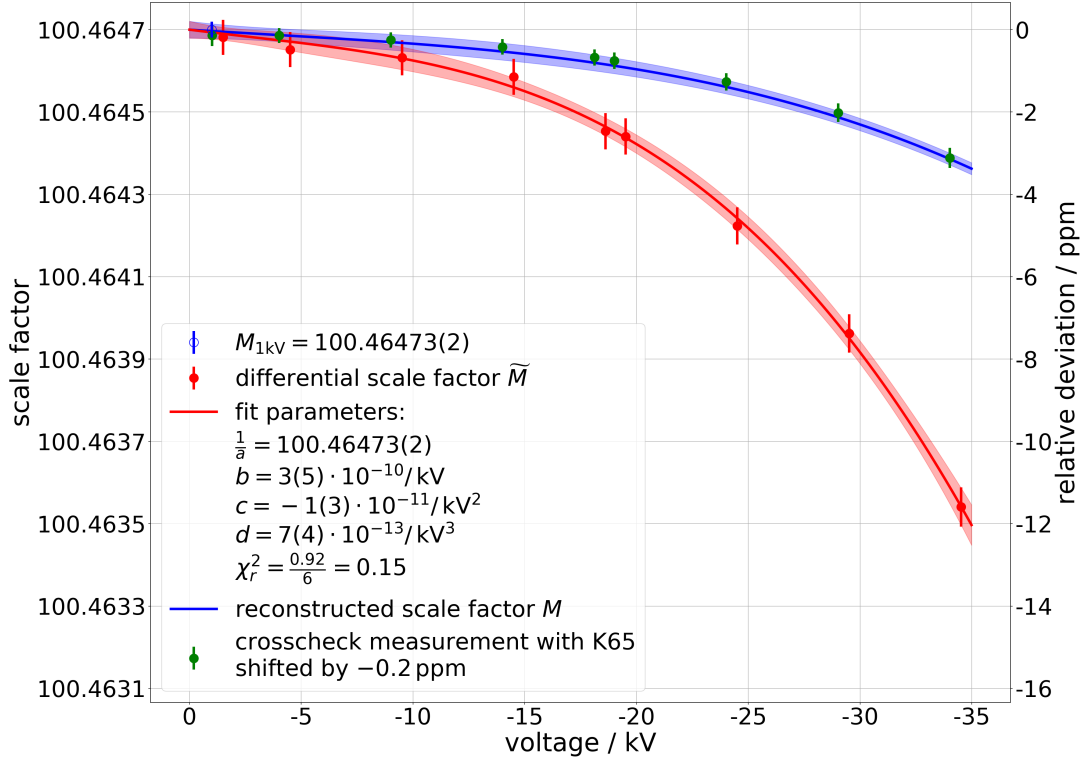
Figure 5.24: Voltage dependency of the G35 100:1 scale factor determined with the newly developed absolute calibration method. The differential scale factors $\widetilde{M}$ measured at different voltages (red points) and the low voltage scale factor $M_{1\mathrm{kV}}$ (blue point) are fitted with a polynomial of third order (red line). The error-bars include the statistical and systematic uncertainties. The obtained coefficients are used to calculate the real scale factor M for a voltage range from 0 to $-35\,\mathrm{kV}$ (blue line). In order to verify the result for the G35, the two month earlier calibrated K65 was used to crosscheck the voltage dependency (green points). Note, that all green data points are shifted by $-0.2\,\mathrm{ppm}$ in y direction (see text).

the uncertainties, confirming the result obtained for the linearity measurement with the novel absolute calibration method. To get an excellent agreement, the absolute value of the scale factor required a constant offset of $-0.2\,\mathrm{ppm}$ over the full range of $-35\,\mathrm{kV}$. This shift exceeds the combined short-term uncertainties (voltage dependent, average about $0.1\,\mathrm{ppm}$) for the real scale factor. However, an additional relative uncertainty of $\pm0.5\,\mathrm{ppm}$ for the absolute value of the scale factor is considered to be realistic, since all previous low voltage- and high-voltage measurements showed this level of uncertainty, when repeated later on a time scale of weeks or months. Therefore, it is reasonable to shift data points of measurements with a significant time difference (here more than 2 months for the comparison shown in figure 5.24) with a constant offset, in order to check the voltage dependency.

The linearity measurements of the G35 were performed at different temperatures in order to investigate the optimal working conditions of the divider. An overview

of this measurements is given in [91] and an extensive discussion will be presented in [90].

In order to check the reliability and reproducibility of the novel absolute calibration method, the long term stability of $\widetilde{M}$ was investigated. Figure 5.25 shows the differential scale factor of the K65 HV divider measured over a time period of about 330 days. The scattering of the determined values of $\widetilde{M}$ is below ± 0.5 ppm. Compared to the stability of the K65 of 0.02 ppm per month determined at PTB in 2011 [36], the results obtained with the newly developed absolute calibration technique are in good agreement, confirming the general principle and functionality of this method.

The uncertainties of the differential scale factor of about 0.4 ppm are mainly dominated by the two devices, which are operated on the HV potential: the 1 kV reference divider and the corresponding DVM. Accordingly, their calibration before the measurement is of crucial importance. The full uncertainty budget is shown in table 5.1, showing the contributions of the single devices.
Furthermore, at this level of precision, also the resistances of the used cables become relevant. Especially on the HV side of the setup, cable resistances, which can be in the order of 1 Ω, influence the calibration result when they are not included in the analysis. The used reference HV divider Fluke 752A has an input resistance of 2 MΩ. This means, that a cable resistance in the order of 1 Ω influences the calibration result on the ppm level. However, this is more
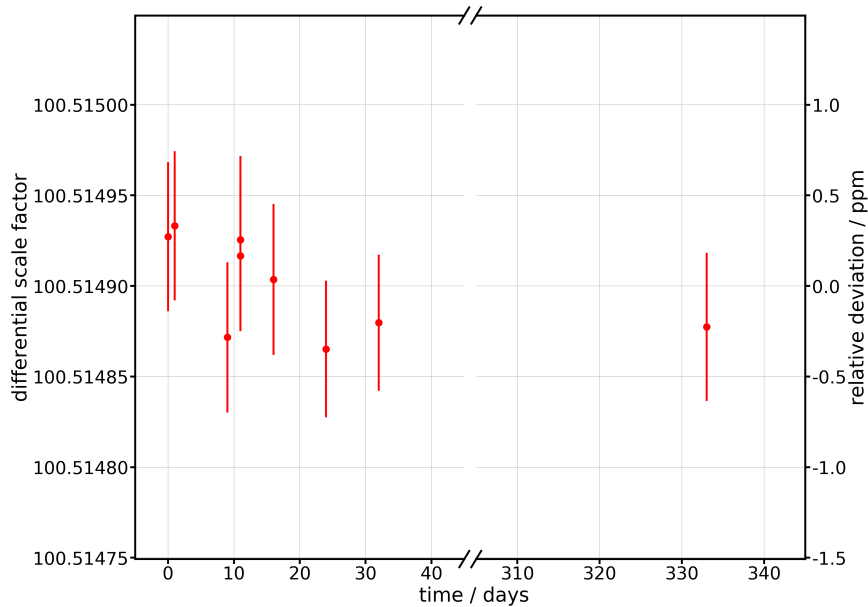

Figure 5.25: Differential scale factor $\widetilde{M}$ of the K65 measured at a voltage of $U_{\mathrm{HV}} = -18.6$ kV. The error-bars include the statistical and systematic uncertainties. Over a time period 330 days all measurements of the differential scale factor show a scattering $< \pm 0.5$ ppm.

Table 5.1: Estimated uncertainty budget for the systematic uncertainty of the differential scale factor with the most important contributions (shown for an exemplary measurement). For all parameter values a Gaussian distribution (1 σ) for the uncertainty was assumed.

parameter	value	abs. uncertainty	unit	rel. import. (%)
M_C HV divider	100.000000	0.000017		22.59
U_4 DVM (10 V cal.)	-10.0000928	0.0000012	V	11.32
U_4 DVM ($\widetilde{M}$ meas.)	-10.0027489	0.0000012	V	11.32
U_2 DVM (μ meas.)	0.0935306	0.0000011	V	10.67
U_2 DVM ($\widetilde{M}$ meas.)	-9.8580844	0.0000011	V	10.67
U_2 DVM (offset cal.)	-0.0000067	0.0000011	V	10.57
U_2 DVM (10 V cal.)	-10.0000948	0.0000011	V	10.57
other uncertainties				12.28
total uncertainty	100.514876	0.000035		100

important for the low voltage calibration – described in section 5.3.2 – since the effect nearly cancels out in the two steps of the differential scale factor measurement of the novel absolute calibration method. Finally, as described above, an additional uncertainty of about 0.5 ppm for the absolute value of the scale factor has to be assumed.

For the calibration of scale factors $M'_A > 100{:}1$, a procedure similar to the one described in section 5.3.2 can be applied, but to load the resistors R_i correctly, the corresponding HV is additionally applied to the input of the HV divider under calibration using a HV cage (see figure 5.26). The investigated scale factor M'_A is calculated according to equation (5.8). The critical scale factor $M_A \leq 100 : 1$ is determined with the novel absolute calibration method as described above. Thus, the issues regarding traceability and the previously neglected voltage dependencies of M_A and M'_A vanish.

To summarize, it could be demonstrated, that with the newly developed absolute calibration method reproducible measurements can be performed with systematic uncertainties of less than 1 ppm. This method can be performed with commercially available equipment and therefore is not restricted to metrology institutes, but offers measurements of linearities of HV dividers with ppm-precision for a wide range of applications. The calibration of the K65 demonstrates, that the HV divider is stable on the ppm-level, outperforming the KATRIN requirements. With this novel calibration method, both HV dividers can be calibrated directly on-site at KATRIN. As the newly built third HV divider can be used as reference, the calibration of the K35 and K65 can be performed during tritium measurement phases, since the HV measurement of the main spectrometer requires only one HV divider, while the second one can be calibrated and vice versa.
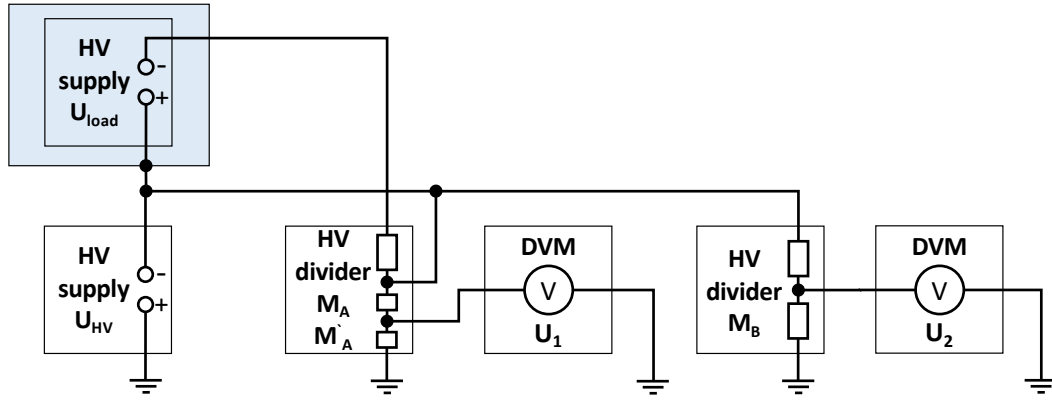
Figure 5.26: Connection scheme for the corrected determination of M_A'. The input voltage U_{HV} is connected to the scale factor output M_A of the unit under test. The upper part of the HV divider with the resistors R_i is loaded with the voltage $U_{load} = U_{HV} \cdot M_A$ created by an additional HV supply, which is operated on the potential of U_{HV} in a HV cage. A second HV divider with the well known scale factor M_B is used to determine U_{HV}.

Calibration of the K35 HV divider with Kr-83m

In July 2017, a calibration and measurement campaign with gaseous Kr-83m, injected into the WGTS from a Rb-83 generating source [101], was performed with the complete KATRIN beamline [29]. With the well-known energies of mono-energetic conversion electrons of this isotope, source properties of the WGTS and the transmission of electrons through the spectrometers were investigated. Furthermore, the adiabatic transport of electrons from the source to the detector and the general alignment and functionalities of the complete system were tested [62, 64]. This measurement campaign also provided the opportunity to calibrate the K35 HV divider to the ppm-level by comparing two conversion electron lines.

A similar HV calibration was previously performed using a condensed Kr-83m source at the former Mainz neutrino mass experiment in [60]. The main idea is to compare the kinetic energy of conversion electrons emitted from two different atomic shells but from the same nuclear transition. The systematic uncertainty of the nuclear transition energy can be canceled; the only remaining uncertainty, which is an order of magnitude lower, arises from the atomic binding energies. The measurements reported in [60] were limited by systematic corrections in the order $100\,\mathrm{meV}$. These corrections, which are not precisely known, account for the final state effects of the decaying nucleus in a sub-mono-layer of Kr-83m on a highly oriented pyrolytic graphite (HOPG) substrate. Gaseous sources overcome the disadvantages of a condensed or solid state source.

In this chapter, the calibration of the HV divider K35 with gaseous Kr-83m is

presented. The next section gives an overview of the calibration idea and the determination of the HV divider scale factor using Kr-83m conversion electron line measurements. Subsequently, the results of the calibration measurements performed at KATRIN are presented.

In addition to the gaseous source, for the first time the condensed krypton source was operated at KATRIN in 2017. During these measurements, the post regulation and fast measurement mode of the main spectrometer high-voltage system (see sections 4.2 and 4.3) were tested with the CKrS. This is discussed in section 6.5.

The essential part of this chapter was published in the journal European Physical Journal C (EPJ C) in 2018 [102]. The chapter of this thesis is based on the original draft of the paper, completely written by myself. The co-authors additions and comments entered the published versions of the papers.

6.1 Calibration of the KATRIN HV dividers with Kr-83m

As described in section 3.2.1, Kr-83m decays via two cascaded transitions with gamma energies of $32\,151.6(5)\,\text{eV}$ and $9405.7(6)\,\text{eV}$, respectively [103]. Both transitions decay dominantly by the emission of conversion electrons instead of gamma radiation. In this analysis, only conversion electrons from the $32\,\text{keV}$ transition are used.

The kinetic energy E_{kin} of a conversion electron from a Kr-83m atom decaying freely in vacuum depends on the energy of the transition E_γ, the atomic binding energy E_{bin} and the recoil energies of the gamma E_{rec}^{γ}[1], and the conversion electron $E_{\text{rec}}^{\text{ce}}$:

$$E_{\text{kin}} = E_\gamma - E_{\text{bin}} + E_{\text{rec}}^{\gamma} - E_{\text{rec}}^{\text{ce}}. \tag{6.1}$$

The binding energy is defined by the atomic shell of the emitted electron. Compared to the other two sources discussed in section 3.2.2, no further corrections have to be applied, since there are no surface or solid body effects. The values for E_{bin} used in this analysis were determined with X-ray spectroscopy measurements [83] yielding $14\,327.26(4)\,\text{eV}$ for the K- and $1679.21(3)\,\text{eV}$ for the L$_3$-subshell.

The recoil energy of the conversion electrons $E_{\text{rec}}^{\text{ce}}$ can be calculated assuming energy and momentum conservation, which is demonstrated in the following for the K-32 line in the non-relativistic case. The kinetic energy of about $E_{\text{kin}} \approx E_\gamma - E_{bin} \approx 17\,824\,\text{eV}$ yield an electron velocity v_{el} of about

$$v_{\text{el}} = \sqrt{\frac{2E_{\text{kin}}}{m_{\text{el}}}} \approx 0.264c, \tag{6.2}$$

---

[1]The recoil energy of the gamma transition E_{rec}^{γ} enters, since the nuclear transition energy ΔE_{fi} and the tabulated gamma energy E_γ differ by this gamma recoil energy: $\Delta E_{\text{fi}} - E_{\text{rec}}^{\gamma} = E_\gamma$.

where c denotes the speed of light and m_{el} the mass of the electron. The momentum p of the electron and the decaying krypton atom are equal because of momentum conservation with

$$p = m_{el} \cdot v_{el} \approx 134\,904\,\mathrm{eV\,c^{-1}}, \tag{6.3}$$

yielding a recoil velocity $v_{kr} = p/m_{kr} \approx 1.73 \cdot 10^{-6}c$ for the krypton nucleus with mass m_{kr}. Finally, the recoil energy can be calculated to be

$$E_{rec}^{ce} = \frac{m_{kr}v_{kr}^2}{2} = 0.12\,\mathrm{eV} \tag{6.4}$$

for the K- and analog $0.207\,\mathrm{eV}$ for the L$_3$-subshell.

Kr-83m atoms decay in the WGTS under ultra-high vacuum conditions. The β-electrons are guided magnetically and adiabatically through the beamline to the main spectrometer, where an integrated spectrum is recorded by varying the retarding potential U. The retarding energy $E = eU$ for an electron of charge e can be determined using

$$E = q \cdot U = q \cdot U_{DVM} \cdot M_{K35}, \tag{6.5}$$

such that a precision digital voltmeter (Fluke 8508A)[2] measures the output voltage U_{DVM} of the HV divider K35 (M_{K35}).

The transmission condition for electrons to pass the main spectrometer is given by

$$E_{kin} \geq q \cdot U_{DVM} \cdot M_{K35} - \Delta\Phi - q \cdot U_{pot.dec.}, \tag{6.6}$$

where $\Delta\Phi$ describes the difference between the source and spectrometer work functions. Due to the large dimensions of the main spectrometer (diameter of approximately 10 m), the retarding potential across the analyzing plane is not completely homogeneous and shows a radial dependence. Therefore, a correction for the radial potential $U_{pot.dec.}$ is necessary. This potential decrease depends on the retardation voltage and the radial position in the analyzing plane. It was determined for every FPD pixel by an electric field calculation with the simulation software KASSIOPEIA [55] by J. Behrens[3] (see section 6.3).

The so-called transmission edge is a special case where the kinetic energy of the electrons equals the right-hand side of equation (6.6). Using equations (6.1) and (6.5) and equation (6.6), the scale factor of the HV divider is then given by

$$M_{K35} = \frac{E_\gamma - E_{bin} + E_{rec}^\gamma - E_{rec}^{ce} + \Delta\Phi + q \cdot U_{pot.dec.}}{e \cdot U_{DVM}} \tag{6.7}$$

with U_{DVM} measured at the transmission edge. Following equation (6.7), the K35 could be calibrated by analyzing just a single conversion electron line position. However, the nuclear transition energy and the work function difference are not

---

[2]The DVM was calibrated with a PTB-calibrated 10 V reference device (Fluke 732A).
[3]Institute for Nuclear Physics, Karlsruhe Institute of Technology (KIT)

known to the desired $20\,\mathrm{meV}$ level, prohibiting a ppm-precise calibration of the scale factor. This limitation can be resolved using the energy difference of two conversion electron lines from the same gamma transition

$$M_{\mathrm{K35}} = \frac{\Delta E_{\mathrm{bin}} + \Delta E_{\mathrm{rec}}^{\mathrm{ce}} + e \cdot \Delta U_{\mathrm{pot.dec.}}}{e \cdot \Delta U_{\mathrm{DVM}}} \qquad (6.8)$$

such that E_γ and $\Delta\Phi$ are eliminated from equation (6.7)[4]. The differences of the binding and recoil energies

$$\Delta E_{\mathrm{bin}} = E_{\mathrm{bin}}^{\mathrm{L_3\text{-}32}} - E_{\mathrm{bin}}^{\mathrm{K\text{-}32}}, \qquad (6.9)$$

$$\Delta E_{\mathrm{rec}}^{\mathrm{ce}} = E_{\mathrm{rec}}^{\mathrm{ce,\ L_3\text{-}32}} - E_{\mathrm{rec}}^{\mathrm{ce,\ K\text{-}32}} \qquad (6.10)$$

add up to

$$\Delta E_{\mathrm{bin}} + \Delta E_{\mathrm{rec}}^{\mathrm{ce}} = 12647.963(50)_{\mathrm{sys}} \ \mathrm{eV}. \qquad (6.11)$$

In order to determine the individual conversion electron line energy positions, the observed integral spectrum was fitted with MINUIT. The fit function consists of a Lorentzian with free amplitude a, width Γ and the energy $E(\mathrm{K\text{-}32})$ or $E(\mathrm{L_3\text{-}32})$, convoluted with the transmission function $T(E, U_{\mathrm{DVM}})$ of the main spectrometer (see section 2.2.1)

$$T(E, U_{\mathrm{DVM}}) = \begin{cases} 0 & \text{for } E - eU \leq 0 \\[2mm] \dfrac{1-\sqrt{1-\frac{E-eU}{E}\frac{B_{\mathrm{s}}}{B_{\mathrm{a}}}\cdot\frac{2}{\gamma+1}}}{1-\sqrt{1-\frac{B_{\mathrm{s}}}{B_{\mathrm{m}}}}} & \text{for } 0 < E - eU < \Delta E_{\mathrm{trans}} \\[2mm] 1 & \text{for } E - eU \geq \Delta E_{\mathrm{trans}} \end{cases} \qquad (6.12)$$

Furthermore, a constant background term b is added. Here, the abbreviation $U = U_{\mathrm{DVM}} \cdot M_{\mathrm{K35}}$ from equation (6.5) was used. The width of the transmission function

$$\Delta E_{\mathrm{trans}} = E \cdot \frac{B_{\mathrm{a}}}{B_{\mathrm{m}}} \cdot \frac{\gamma + 1}{2} \qquad (6.13)$$

is calculated from the energy of the electrons and the ratio of the magnetic flux densities in the analyzing plane ($B_{\mathrm{a}} = 0.268\,\mathrm{mT}$) and at the exit of the spectrometer ($B_{\mathrm{m}} = 4.20\,\mathrm{T}$). The normalization factor $\left(1 - \sqrt{1 - \frac{B_{\mathrm{s}}}{B_{\mathrm{m}}}}\right)$ accounts for the fact, that the magnetic field in the source ($B_{\mathrm{s}} = 2.52\,\mathrm{T}$) is lower than the maximum magnetic field encountered by the electrons on their way to the detector (see section 2.2.1). Relativistic corrections are included in equation (6.12) using the Lorentz factor γ of the electron. The final fit function for the K-32 line is

$$f(E) = \int\limits_{eU_{\mathrm{DVM}}M_{\mathrm{K35}}}^{\infty} \frac{a/\pi \cdot \Gamma/2}{(E(\mathrm{K\text{-}32}) - E')^2 + \Gamma^2/4} \cdot T(E', U_{\mathrm{DVM}}) dE' + b. \qquad (6.14)$$

---

[4]The work functions of the source and spectrometer should be constant on the time scale of the measurements.

6.2 Corrections of transmission function

Equation (6.14) contains three additional corrections, which are discussed in this section.

Synchrotron radiation

The conversion electrons of Kr-83m start in the WGTS and are guided through the experimental stages to the FPD by strong magnetic fields (B-fields) in the order of several tesla. Figure 6.1 shows the magnetic field strength along the beam line as function of the distance to the analyzing plane in the center of the MS. It is nearly homogeneous at around $2.5\,\mathrm{T}$ for the WGTS (at about $-40\,\mathrm{m}$) and shows in the transport section ($-16\,\mathrm{m}$ to $-34\,\mathrm{m}$) with its chicane geometries (see section 2.1.3) high gradients and maximum values of up to $4\,\mathrm{T}$. At around $-15\,\mathrm{m}$ the pre-spectrometer is placed. Here, the amplitude drops nearly to 0, since according to the working principle of a MAC-E-filter the magnetic field strength in the analyzing plane is in the order of 10^{-3} tesla. During the krypton measurement campaign 2017, the B-fields over the whole beam line were scaled to $70\,\%$ of the nominal value given in the design report due to short-term appearing technical restrictions.

As described in Maxwell's equations, accelerated charged particles in magnetic
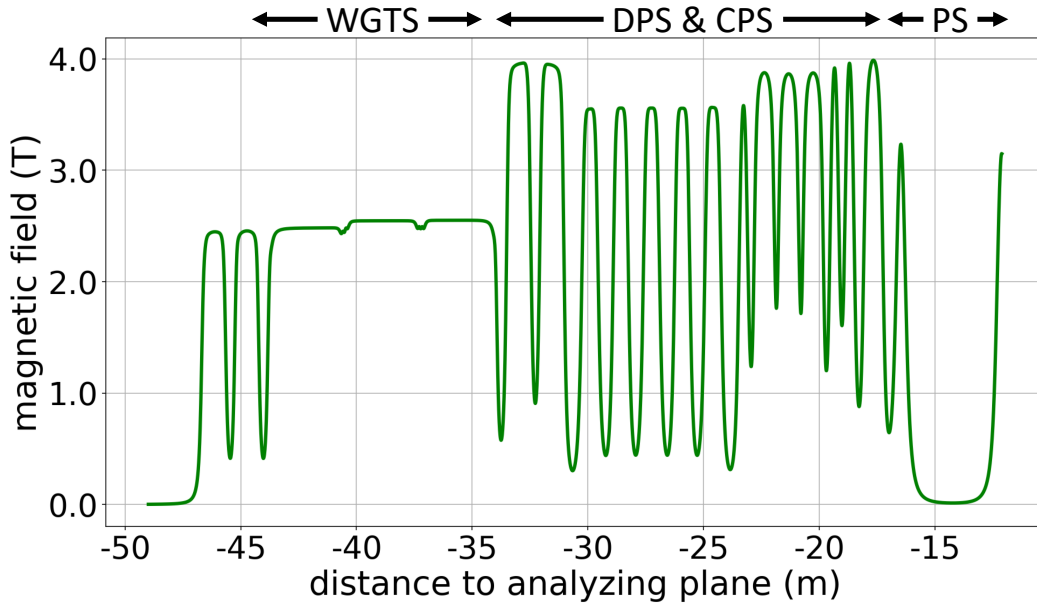
Figure 6.1: Magnetic fields along the KATRIN beam line calculated with the simulation software KASSIOPEIA. The values are scaled to $70\,\%$ compared to the nominal values given in the design report, since this was the maximum setting used in the krypton measurement campaign 2017.

fields emit electromagnetic synchrotron radiation. Therefore, the conversion electrons starting in the WGTS lose energy on their trajectory to the main spectrometer. This energy loss has to be included in the analysis, since it depends on the pitch angle (see section 2.2.1) of the electrons and therefore broadens the width of the transmission function. As it affects only the transversal contribution to the kinetic energy $E_\perp$, the power loss $\dot{E}_\perp$ due to the emission of synchrotron radiation is given by

$$\dot{E}_\perp = -\frac{e^4 \beta^2 \gamma^2}{6\pi\varepsilon_0 m_e^2 c} \cdot B^2 \qquad (6.15)$$

with the relativistic factor γ and the velocity $\beta = \frac{v_\perp}{c}$ for the electron with mass m_e. Here, ε_0 stands for the vacuum permittivity and c represents the speed of light. Since the power loss is dependent on the velocity in transversal direction $v_\perp$ and therefore on the kinetic energy, its influence on electrons originating from different shells (and therefore kinetic energies) varies. The difference of E_{kin} for electrons from the K- and the L-shell is for example in the keV range.

The energy loss for electrons starting in the WGTS with different polar angles was calculated in [57] and is shown in figure 6.2. It depends on the starting position in the WGTS and increases for higher polar angles to a maximum of about 80 meV at 50.77°, since this is the cut-off angle due to magnetic reflections of the main spectrometer (see section 2.2.1).

In order to include this into the analysis, the broadening of the transmission function caused by the emission of synchrotron radiation was calculated. Since
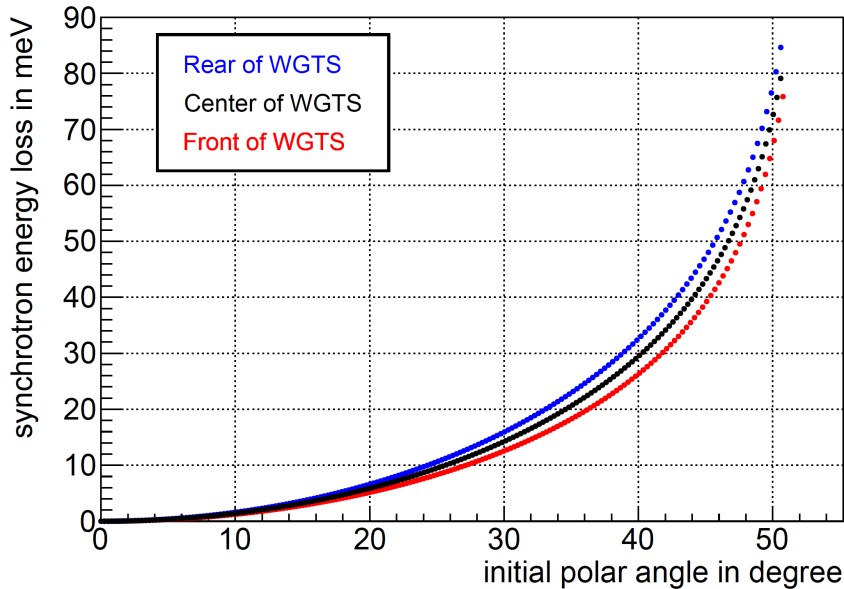

Figure 6.2: Synchrotron radiation energy loss of electrons originating from different positions in the WGTS depending on their starting polar angle. Calculated by and taken from [57].

an analytical description of the synchrotron energy loss was not available, the calculations were performed numerically for 12 different starting polar angles, interpolating linearly the intermediate range. The values for the energy loss were taken from figure 6.2 but scaled to 70 % magnetic field strength.

Figure 6.3 shows the influence of this correction. The uncorrected analytical transmission function (green line) is approximated numerically for 12 points (blue). The inclusion of the calculated synchrotron radiation energy loss causes a shift to higher energies for larger starting polar angles (red). The transmission function gets broadened, since electrons starting with higher polar angles are affected to a larger extend by synchrotron radiation energy losses (it scales with the amount of initial transversal kinetic energy) and are transmitted at lower retarding potentials [58].

This correction was implemented for the K-32 and the L$_3$-32 line, resulting in a 3 % and 2 % broadening of the transmission function. Overall, the influence on the line positions obtained with the fit is given by 11 mV for the K-32 line and 15 mV for the L$_3$-32 line in the analysis.
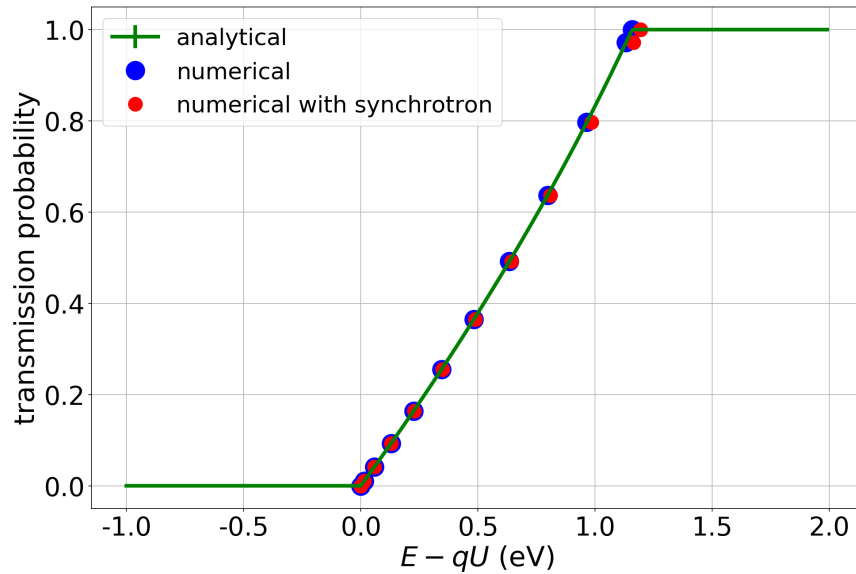

Figure 6.3: Effect of the synchrotron radiation energy loss on the transmission function. The analytical function without synchrotron radiation loss is shown by the green line. For 12 different starting angles a numerical transmission function was calculated (blue points) and the intermediate range was interpolated linearly. The synchrotron radiation energy loss affects the transmission function by a small additional broadening, which is shown in red. For clarity, the interpolation between the calculated points is not shown.

HV ripple

Throughout the measurements, a HV ripple of the retarding potential was observed, since the post regulation system (see section 4.2) was inactive. The ripple had a nearly sinusoidal shape with an amplitude of 187 mV for the K-32 line and of 208 mV for the L_3-32 line. The raw signal, measured with the ripple probe and an oscilloscope, is shown in figure 6.4 a). As described in detail in [33], an unknown HV fluctuation results in a broadening of the transmission function and has to be included in the analysis.

Thermal broadening

The third correction to the transmission function accounts for the temperature of the krypton gas inside the WGTS of $T = 100$ K. Therefore, the kinetic energy of the conversion electrons is modified by a thermal Gaussian broadening, which can be calculated according to [58] with

$$\sigma_E = \sqrt{(E_{\mathrm{kin}} + 2m_e) \cdot E_{\mathrm{kin}} \cdot k_B T / m_{\mathrm{kr}}} \qquad (6.16)$$

to be 46 meV for the K-32- and 60 mV for the L_3-32 line. Here, k_B denotes the Boltzmann constant. This broadening is shown schematically for a Gaussian in figure 6.4 b). The recorded ripple signal and the Gaussian broadening are convoluted with the newly obtained numerical transmission function (modified to include the synchrotron radiation energy losses) in the fit, in order to include all these effects into the analysis.
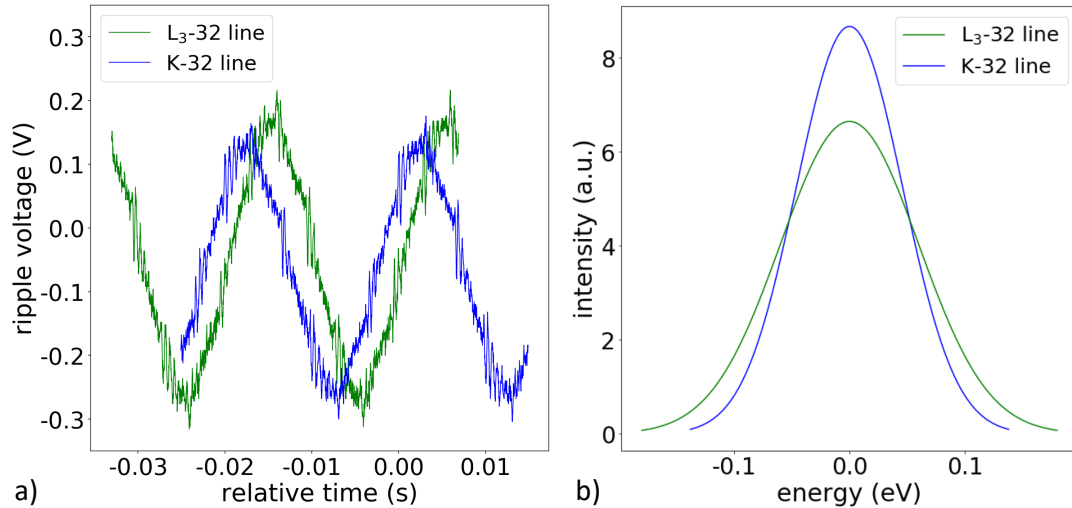

Figure 6.4: Additional corrections of the transmission function. a) Observed HV ripple for the HV settings of the K-32- and L_3-32 line measurements. b) Gaussian broadening of the K-32- (46 meV) and L_3-32 (60 mV) line caused by the thermal movement of the krypton atoms at 100 K in the WGTS.

6.3 Run- and pixel selection

During the calibration and measurement phase in July 2017, the energy of all conversion electron lines of the gaseous- and condensed Kr-83m source were measured. Different experimental settings were tested in order to characterize the system. Overall, about 600 measurement runs with both sources were performed. For the HV calibration, runs of the K-32 and the L_3-32 lines taken with the gaseous source were used. Since the analysis described in the previous sections is based on the difference of these two line positions, runs with a comparable experimental set-up regarding magnetic field settings (2.7 G in the analyzing planes) and voltage step size (0.5 V) were used. Furthermore, in order to avoid unknown systematics which could arise on larger time scales, two measurements within a short time interval were used for the analysis.

The two chosen runs are #33054 for the K-32- and #33083 for the L_3-32 line, which were taken on the same day. Figure 6.5 shows the averaged rate measured with the FPD for the individual pixels of both runs. For the L_3-32 line measured at about -30 keV, nearly the whole detector is illuminated by electrons hitting the FPD with a count-rate of approximately 50 cps. The K-32 line is measured at voltages of about -18 keV. At this retarding potential not only electrons from the K-shell are transmitted, but e.g. also the high-energy electrons originating from the L_3-32 line. For these electrons with a kinetic energy of about 10 keV higher than the retarding energy of the MS the motion through the spectrometer becomes non-adiabatic. Hence, electrons from outer radii of the flux tube do not follow the magnetic field lines and will not reach the FPD at the corresponding pixels, but might get shifted to larger radii. Since no energy cut was applied to the count-rate shown in figure 6.5, the contribution for the central part of the
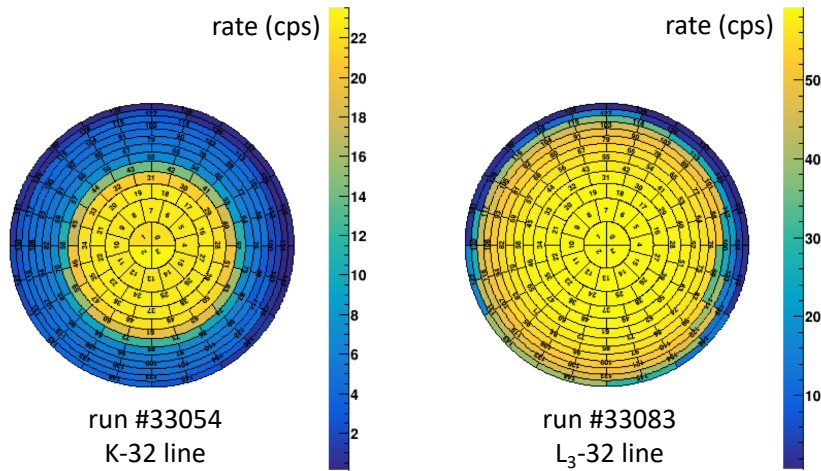

Figure 6.5: Averaged measured rate for the individual pixels during the K-32- (left) and L_3-32 line (right) measurement runs. No energy cut is applied.

FPD is mainly originating from the L_3-32 line. The electrons of the K-32 line have a count-rate of about 6 cps, which can be seen in the outer pixel rings.

In the direct comparison of the two runs, the rate of the L_3-32 line electrons is higher in run #33083, since the valve setting of the generator, which regulates the gas flow into the WGTS, was changed in-between both runs. Before analyzing, a cut of ± 3 keV around the MS retarding energy was applied to the data.

To avoid increased systematic uncertainties at larger beam radii, a combined analysis of the 40 innermost detector pixels was performed in order to obtain high statistics. Each detector pixel was treated with its corresponding potential decrease. Figure 6.6 shows $U_{\text{pot.dec.}}$ for the example of the K-32 line. The decrease ranges from 1.8 V for the outermost FPD pixels to about 2.3 V for the center of the detector. This behavior is expected, since the corresponding areas in the analyzing plane for the outer pixels are close to the wire electrode, creating the retarding potential.

$U_{\text{pot.dec.}}$ amounts to about 2.25 V for both the K-32 and the L_3-32 measurement with a r.m.s. value of less than 60 mV for the 40 innermost detector pixels. The average difference over all these pixels between both HV settings (about 18 kV and 30 kV) amounts to 9 mV only.
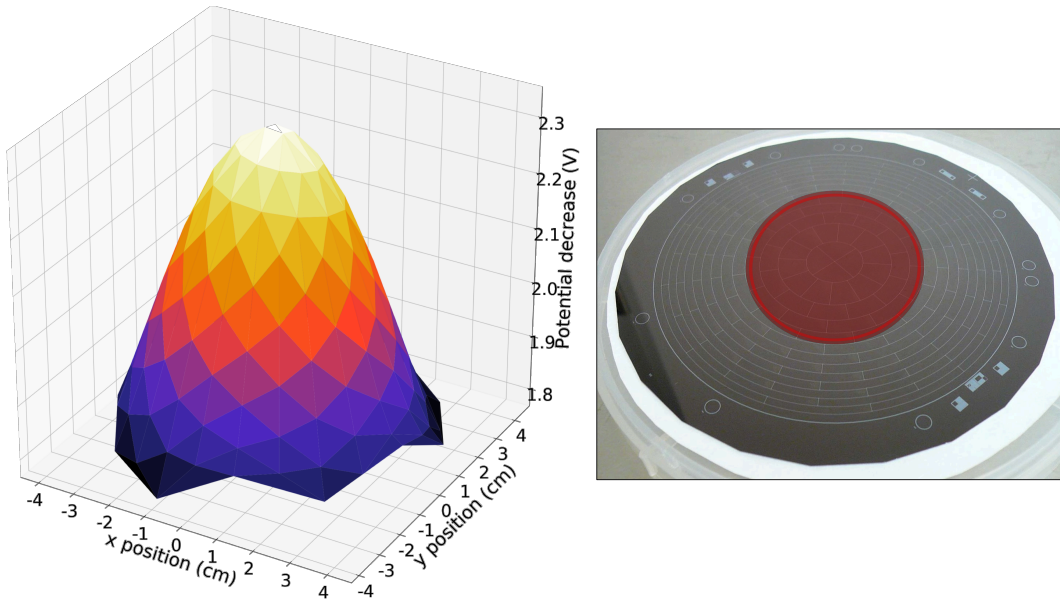

Figure 6.6: Potential decrease calculated with the simulation software KASSIOPEIA for the HV setting of 18 kV of the MS. The decrease is smaller for the outer FPD pixel rings, since they are close to the wire electrode. The highest values occur for the innermost pixels. The picture of the circular FPD consisting of 148 segments illustrates the effect for the 40 innermost pixels, used in the analysis (see red shaded area).

6.4 Calibration results for the K35 HV divider

The discussed K-32 and L$_3$-32 measurement runs were used to calibrate the high-voltage divider K35 as described in the previous sections. For illustrative reasons, the average of all K-32 and L$_3$-32 conversion electron data of the 40 innermost detector pixels was calculated and fitted, as shown in figure 6.7. The good agreement between data and the fit model can be seen in the residuals as well as in the reduced χ^2 values of the fits ($\chi^2_{\mathrm{red}} = \frac{17.25}{27} = 0.64$ for the K-32 and $\chi^2_{\mathrm{red}} = \frac{39.28}{28} = 1.40$ for the L$_3$-32 line).

For the final result, the averaging of the pixel-dependent $U_{\mathrm{pot.dec.}}$ values is avoided by performing a combined 82-parameter fit of the data from the 40 innermost detector pixels, leading to the results shown in table 6.1. In this combined analysis, common fit parameters for the line width Γ and position E(K-32) (or E(L$_3$-32), respectively) but with separate fit parameters for amplitude a_i and background b_i for each pixel ($i = 1, ..., 40$) were used.

The results from table 6.1 yield a voltage difference of

$$\Delta U_{\mathrm{DVM}} = 6.412315(15)_{\mathrm{stat}}(15)_{\mathrm{sys}} \text{ V}. \tag{6.17}$$
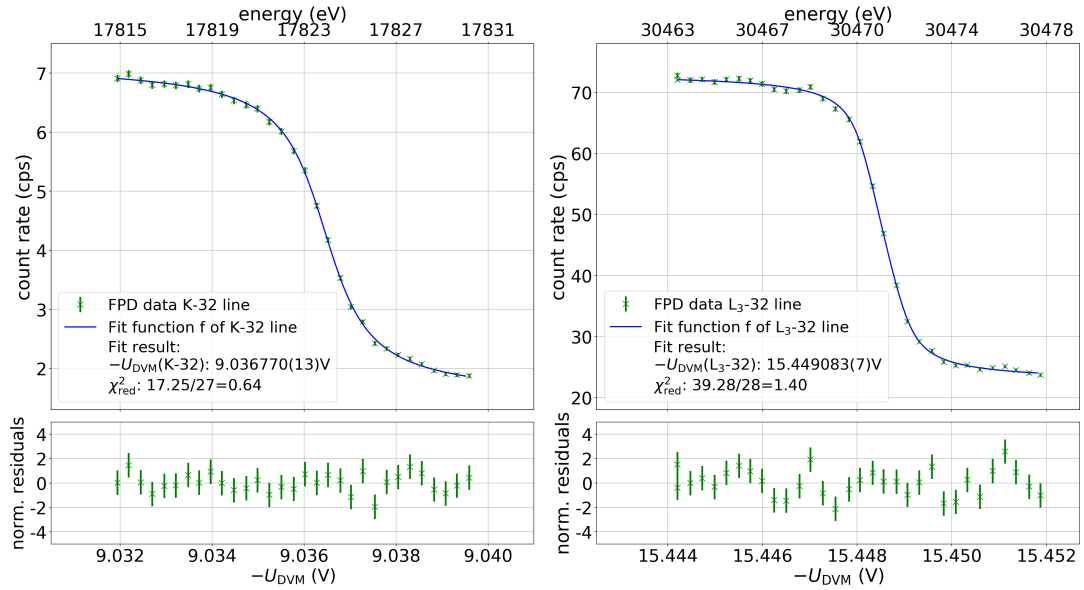

Figure 6.7: Averaged K-32 (left) and L$_3$-32 (right) data of the innermost 40 detector pixels with a four-parameter line fit to visualize the more complex combined fit of the 40 individual pixels (see text). The denoted line positions do not include the work function difference $\Delta\Phi$ between the source and the spectrometer, which is not known to ppm precision, or other systematic uncertainties. The upper abscissa provides the corresponding energies according to equation (6.5) and assuming a scale factor of 1972.4531 for the K35, which was the latest calibration value determined at the PTB. The panels below the fits display the normalized residuals.

Table 6.1: Fit result for the combined analysis of the 40 innermost detector pixels. For the denoted line, the work function difference $\Delta\Phi$ between the source and the spectrometer is not known with competitive precision and is not included. The same holds for other systematic uncertainties. The uncertainty of $\Delta\Phi$ was estimated to be of the order of a few $100\,\text{meV}$. As $\Delta\Phi$ drops out in the calculation of ΔU_{DVM}, this does not pose a problem for further analyses.

parameter	K-32	L$_3$-32
-U$_{\text{DVM}}$ line position (V)	9.036768(12)	15.449083(9)
U$_{\text{DVM}}$ line width (V)	0.00135(4)	0.00056(2)
χ^2_{red}	$\frac{1131.91}{1158}{=}0.98$	$\frac{1257.51}{1198}{=}1.05$

In the evaluation of the systematic uncertainties associated with this measurement, a $\pm20\,\%$ variation of the high-voltage ripple amplitude and a $\pm50\,\%$ uncertainty of the synchrotron radiation correction was considered. The assumed $\pm5\,\text{meV}$ uncertainty on the variation of $U_{\text{pot.dec.}}$ for the different conversion electron lines results in an uncertainty of $\pm2.5\,\mu\text{V}$ for ΔU_{DVM} (equation (6.5)). In the voltage determination with the DVM, a $0.5\,\text{ppm}$ uncertainty of the read value and a $0.2\,\text{ppm}$ uncertainty of the full range of the device was applied. These effects yield the uncertainties of $8.5\,\mu\text{V}$ ($11.7\,\mu\text{V}$) for the K-32 (L$_3$-32) voltage reading, and $14.5\,\mu\text{V}$ for ΔU_{DVM}, respectively.

Since the term $q \cdot \Delta U_{\text{pot.dec.}}$ was already absorbed in the fitted data, the scale factor can be determined simply by dividing equation (6.11) by equation (6.17):

$$M_{K35} = 1972.4488(45)_{\text{stat}}(91)_{\text{sys}} \approx 1972.449(10). \tag{6.18}$$

This result is in good agreement with the last calibration at PTB (1972.4531(20) in 2013) within the uncertainties. With a four-year interval between the two calibrations, the relative deviation amounts to $\Delta M_{\text{K35}}/M_{\text{K35}} = -2(5)\,\text{ppm}$. This means that the stability of the scale factor is on the ppm-level per year or better, assuming a constant drift. For a typical KATRIN measurement period, which is partitioned in two-month intervals, sub-ppm-stability can be assumed. This demonstrates, that the relative stability of the HV divider is better than $3\,\text{ppm}$ in a two-month interval, which significantly surpasses the design specifications. The uncertainty of $5\,\text{ppm}$ of this new calibration method is dominated by the uncertainty of the difference of the atomic binding energies (relative uncertainty of $4\,\text{ppm}$). This could improve in the next years with more precise spectroscopy measurements or theoretical calculations. The combined statistical relative uncertainty of about $2\,\text{ppm}$ can be improved by future measurements with higher statistics during calibration phases at KATRIN. The similarly large uncertainty of the voltage reading could be improved by measuring the two conversion lines in quick succession ($\sim20\,\text{min}$) in order to mitigate the temporal drift effect of the device.

6.5 Kr-83m with fast HV monitoring & post regulation system

During the krypton measurements, the setup of the fast voltage measurement (see section 4.3) and the post regulation system (see section 4.2) were used for the first time after their commissioning in physics related measurements. Due to technical limitations the PR was used exclusively with the CKrS during the krypton campaign. Since it was limited to operation voltages of about $-20\,\mathrm{kV}$, only conversion electrons with kinetic energies up to $20\,\mathrm{keV}$ (e.g. the K-32 line) were measured. Since the fast voltage measurement system was not tested within the HV system of KATRIN before, it was investigated if the same level of precision as in the standard mode can be achieved. Furthermore, tests with and without active PR were performed, in order to examine the influence of the HV ripple on the precision measurements.

An ideal indicator for this checks is the measurement of the K-32 line, since its absolute energy and line width are precisely known. Figure 6.8 shows as a comparison of two K-32 line measurements with active PR, one with the standard- (a) and one with the fast voltage measurement setup (b). In the analysis of the standard measurement, five runs were combined in order to increase statistics. Since the CKrS illuminates only several pixels due to the small dimensions of the substrate (see section 3.2.2), in contrast to the measurements with the gaseous source only one pixel was used in the analysis. The left part of figure 6.8 shows a standard measurement of the K-32 line. The fit function is given by equation (6.14), but the corrections discussed in section 6.2 are different. The transmission function is not convoluted with a thermal Gaussian broadening, since the krypton atoms are frozen onto a substrate at cryogenic temperatures. Furthermore, the assumed ripple of the HV was measured to be $<20\,\mathrm{mV}$, since the post regulation system was active during the measurements. In order to account for unknown systematic effects, which are currently under investigation and will be further discussed in [104], an additional Gaussian broadening of the conversion electron line of $360\,\mathrm{mV}$ (see [105]) was assumed in the fit.

The data is described well by the model, demonstrated by the good value of $\chi^2_{\mathrm{red}} = 0.92$ and also by the normalized residuals. The result for the line width of $2.74(1)\,\mathrm{eV}$ is in agreement with previous measurements in [35] within the uncertainties. Since the measured line position depends on corrections for this kind of sources (e.g. image charges, work function, cleanliness of the substrate etc.) and the HV calibration, the absolute value is not known to the ppm-level and is only stated as an estimation.

As demonstrated in the right plot of figure 6.8, the measurement of the K-32 line with the fast measurement setup yields a comparable result. Here, only one run was available for the analysis. The line width of $2.74(1)\,\mathrm{eV}$ agrees with the standard measurement, whereas the line position deviates by $114(15)\,\mathrm{meV}$. This can be explained by the fact that the line position measured with the CKrS showed a time dependent behavior during the measurement campaign, which
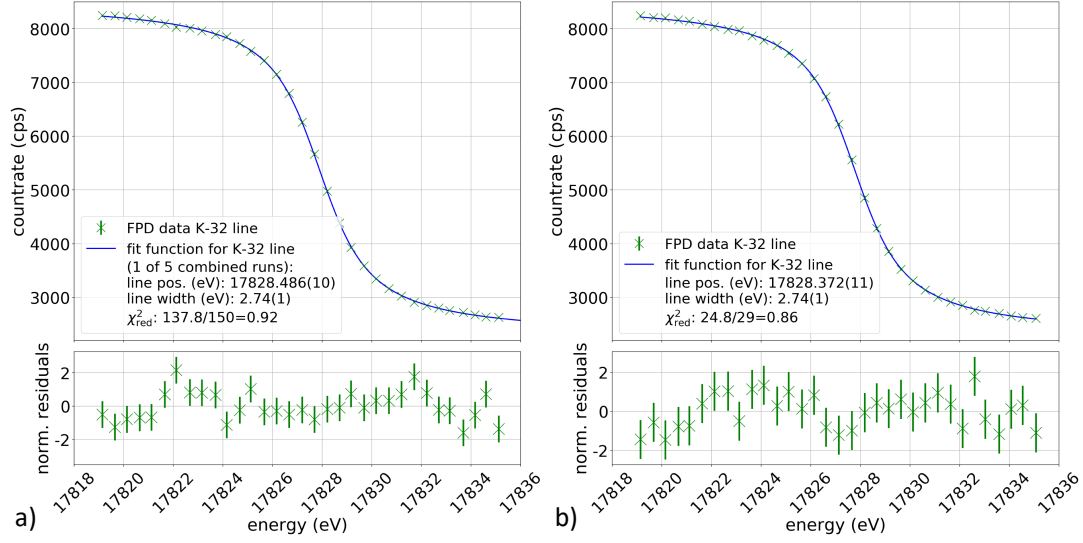
Figure 6.8: CKrS measurement of the K-32 line with the standard (a) and fast (b) HV monitoring setup. For the standard measurement, five runs were combined in order to increase the statistics (only one of the five measured lines is shown). For each of the five measured lines individual parameters for the amplitude, background and line position were assumed. The line width was used as one common parameter. For the fast measurement setup only one run was available.

was presumably caused by the condensation of residual gas onto the substrate (see discussion in [37]). The absolute value varied on the $100\,\text{meV}$ scale over the whole measurement campaign. Therefore, comparisons to the ppm-level are not reasonable. However, since in this configuration only the general idea and functionality of the fast voltage measurement system were tested, this does not pose a problem.

The reduced $\chi^2_{\text{red}} = 0.86$ is slightly worse for the fast measurement, which can be explained by the increased uncertainty of the HV measurement. In this mode, two DVM are used in order to determine the retarding potential, whereas in the standard mode only one DVM is used with the K35. However, one has to keep in mind also the fact, that for the standard mode the number of data points is a factor of 5 higher.

Finally, the influence of the post regulation system on the measurement of the K-32 line was investigated in the standard HV monitoring mode. Therefore, the measurements shown in figure 6.8 (a) were compared to a combined fit of five runs without active post regulation. The result of the analysis is shown in table 6.2. For the measurements without active PR, the measured sinusoidal HV ripple of $240\,\text{mV}$ was assumed in the fit function. Although the line widths are in agreement within the uncertainties, the measurements with active post regulation show a better χ^2_{red} value, indicating that the model fits the data to a better extent. Since the PR system smoothens any arbitrary form of HF noise,

Table 6.2: Comparison of K-32 line measurements with and without active post regulation. For both measurements, a combined analysis of 5 runs was performed, where the line width was used as common fit parameter for all runs and the other parameters (line position, amplitude and background) were treated individually for every run. For the HV ripple, a sinusoidal shape with the below stated amplitude was assumed, measured with the ripple probe and an oscilloscope.

Post regulation system status	assumed HV ripple (mV)	Doppler broadening (mV)	line width (eV)	χ^2_{red}
active	20	360	2.74(1)	$^{137.8}/_{150} = 0.92$
not active	240	360	2.75(1)	$^{248.9}/_{169} = 1.47$

this is expected, as the HV ripple can not be assumed as completely sinusoidal.

To summarize, these measurements proof, that the fast HV monitoring system can be used at KATRIN for precision measurements without significantly increased uncertainties. The system is installed stationary at the basement of the MS and will be included completely in the KATRIN SCS in the next months. Furthermore, it could be demonstrated that the measurements with an active post regulation system can be described well with the model of an assumed HV ripple of about $20\,\mathrm{mV}$, whereas the measurements without active PR are influenced by non-sinusoidal HV fluctuations, indicated by the worse χ^2_{red}.

Conclusion and outlook

Although major observations and experimental milestones were achieved over the last decades in the field of neutrino physics, many important questions are still not answered. After their postulation in 1930 by Pauli, it took experimental physicists more than 20 years until this charge-less, weakly interacting fermion was observed by Cowan and Reines 1956 via the inverse β-decay. In the standard model of particle physics, which describes all elementary particles and their interactions, neutrinos are assumed to be massless. In the 1990, the SNO and Super-Kamiokande experiments, investigating solar and atmospheric neutrinos, proved that neutrinos oscillate. The fact that this phenomenon was observed requires, that the neutrino flavor eigenstates are connected via the non-trivial mixing matrix U_{PMNS} with the mass eigenstates and that the neutrino mass is not zero. Since experiments examining neutrino oscillation are not sensitive to this parameter, the absolute mass scale still needs to be determined. A model-independent direct method based on energy- and momentum conservation is given by direct kinematic measurements of the β-decay. Experiments measuring the β-decay of tritium were performed in Mainz and Troitsk and provided a current upper limit of $m_{\overline{\nu}_e} < 2\,\mathrm{eV\,c^{-2}}$ [5].

The next generation experiment KATRIN aims to increase the sensitivity to $0.2\,\mathrm{eV\,c^{-2}}$ at 90 % C.L. [28]. Gaseous tritium decays in a windowless source with an overall activity of $\approx 1 \times 10^{11}$ Bq. About 50 % of the electrons are guided with strong magnetic fields provided by superconducting magnets to the transport section, where the tritium gets removed from the beam tube by means of differential and cryogenic pumping. Subsequently, the energy of the electrons is analyzed in

the spectrometer-detector section. Here, the low energy part of the spectrum gets reflected by the pre-spectrometer with an electrostatic retarding potential. The high-energy electrons close to the endpoint of the spectrum reach the main spectrometer, where their energy is analyzed with an unprecedented precision. Like that, an integrated spectrum is measured. Both spectrometers are based on the technique of a magnetic adiabatic collimation combined with an electrostatic filter (MAC-E filter). The energy resolution of the main spectrometer is 0.93 eV at the tritium endpoint of about 18.6 keV. Finally, for each retarding potential of the main spectrometer, the transmitted electrons are counted with the focal plane detector, a silicon PIN diode with 148 pixels.

The retarding potential of the main spectrometer – as one of the major systematic uncertainties – has to be maintained and monitored with a precision of about 60 mV at -18.6 kV (3 ppm). This holds for short-term fluctuations as well as for the longterm operation over a measurement period of two months. The potential is monitored with a third MAC-E filter at the monitor spectrometer and directly measured with two custom-made ultra-precise HV dividers K35 and K65.
A complex high-voltage system consisting of several cascaded power supplies is used to create and distribute up to 44 individual potentials to the wire electrode system covering the inner surface of the main spectrometer vessel. AC fluctuations of the retarding potential are smoothened passively by three capacitors, which were installed between the main spectrometer vessel and the grounded beam tube. Additionally, an active post regulation system based on a triode shunt regulator attenuates fluctuations between DC and 1 MHz. With this system, the measured HV ripple of the retarding potential was reduced by more than one order of magnitude below 20 mV, agreeing with previous measurements [33].
In order to test the achievable longterm stability of the system, measurements with a fixed retarding potential were performed for about 15 h in the context of this thesis. Without active post regulation, stabilities for 10 min up to 1 h measurement intervals with standard deviations of about 8 mV (0.4 ppm) were achieved. When the post regulation is activated, it smooths the retarding potential of the main spectrometer and also regulates the DC value measured with an auxiliary voltage divider. Hence, the stability is limited by this HV divider. With active post regulation, stabilities for 10 min up to 1 h measurement intervals with standard deviations of about 20 mV (1 ppm) were achieved. Both results outperform the KATRIN requirement of 3 ppm for the HV uncertainty.

In the standard HV monitoring mode of a tritium measurement run at KATRIN, the length of a sub-run for an individual HV setting is limited by the integration time of the precision digital voltmeters (about 6 s) to be longer than 30 s in order to gather enough statistics. Furthermore, measurement time gets lost when the HV setting is changed because a new sub-run starts after the HV was measured to be stable to the ppm-level. Therefore, a new method was developed within this thesis, dividing the HV monitoring into a measurement of a static reference

potential of $U_{\mathrm{ref}} = -18.6\,\mathrm{kV}$ and the voltage difference $U_{\mathrm{diff}} \leq 1\,\mathrm{kV}$ to the main spectrometer HV $U_{\mathrm{MS}} \approx -18.6\,\mathrm{kV}$. U_{ref} is measured with the KATRIN HV dividers in combination with slow precision DVMs. For the difference voltage, a fast measuring DVM with integration times on the sub-second scale can be used, since the absolute precision of about $20\,\mathrm{mV}$ is only on a 10^{-4} level.

With this setup, the sub-run length for tritium measurements is not limited to about $30\,\mathrm{s}$, but can be chosen to be below $10\,\mathrm{s}$. More importantly, the time between sub-runs can also be reduced significantly. In the standard mode, the stability monitoring of the HV before each sub-run usually takes about $20\text{-}30\,\mathrm{s}$. The newly developed fast HV mode reduces this time up to a factor of four, limited by the post regulation system. With the fast measurement setup, the duration needed to change and stabilize the retarding potential to the ppm-level with the post regulation was investigated to be about $5\,\mathrm{s}$. Since a standard measurement run at KATRIN consists of about 40 sub-runs, a significant amount of waiting time can be avoided with this method.

First successful test measurements with krypton in a calibration campaign in 2017 demonstrated, that the system can be used with the same ppm-precision as provided by the standard HV measurement mode. After the first tritium measurements in 2019, it is planned to integrate the setup into the KATRIN SlowControl system in order to allow the usage for future measurement phases following later this year.

The overall longterm monitoring of the high voltage at KATRIN is performed by the two precision HV dividers K35 and K65. Hence, regular calibration measurements are essential in order to check the stability of the devices. Over the last years, multiple calibrations were performed using high voltages at the German national metrology institute Physikalisch-Technische Bundesanstalt (PTB) and additionally with commercially available low voltage equipment up to $1\,\mathrm{kV}$ on-site. Both HV dividers showed (sub)ppm stability per year for all of their scale factors. These calibration methods are not completely traceable to reference standards, as they neglect the voltage dependency of resistors for different voltages caused by thermal effects and leakage currents. Therefore, two new independent absolute calibration methods were developed in the scope of this work, which overcome the disadvantages of previous methods and can be performed on-site at KATRIN.

The first method is based on the principle of electrical calibrations traceable to the Josephson voltage standard [61]. Here, the commercially available traceable equipment for voltages up to $1\,\mathrm{kV}$ is operated on high-voltage potential in order to determine a differential scale factor. The general procedure is divided into two steps. Firstly, the HV divider under test M_{B} and a second divider M_{A} used as reference, both with a scale factor ideally scaling 100:1, are connected to a HV source U_{HV}. The ratio of the two scale factors can be determined with sub-ppm precision without knowing the single scale factors.

In the second step, the input voltage of the unit under test is increased by δU_{HV} with a second HV source, precisely measured and operated on the potential U_{HV}.

The differential scale factor $\widetilde{M_B}$ is given by the ratio of the change of the input-(δU_{HV}) and output (δU_{LV}) voltages

$$\widetilde{M_B} = \left.\frac{\delta U_{\mathrm{HV}}}{\delta U_{\mathrm{LV}}}\right|_{U_{\mathrm{HV}}} \tag{7.1}$$

measured at U_{HV}. As the reference voltage divider is only used to monitor the stability of U_{HV}, the absolute value of its scale factor can have relative uncertainties in the 10^{-4} range. For this purpose, a new device was built with commercial precision resistors, showing short-term stabilities on sub-ppm-level and a long-term reproducibility in the 10 ppm range.

First test measurements of this newly developed calibration method were performed with two precision HV dividers K65 [72] and G35 [90] over one year and demonstrated (sub)ppm stability. Calibration measurements regarding the absolute values and linearity of the K65 scale factors showed a negligible voltage dependency and are in agreement with the results shown in [36], which were determined at PTB. Test measurements with the second precision HV divider G35 showed a voltage dependency of about 3 ppm over the full range of $-35\,\mathrm{kV}$, which was crosschecked and confirmed by a reference measurement with the K65. The overall uncertainty of the differential scale factor was in all cases below 1 ppm, limited by the uncertainties of the commercial devices, operated on the HV potential and measuring the differential voltage.

This calibration method and the results presented in this thesis were submitted to the Journal Metrologia in 2019 and published on arXiv [92]. Additionally, a small part was extracted for two conference proceedings, both accepted for publication in SPRINGER Lecture Notes in Electrical Engineering [91, 93].

The second calibration method uses mono-energetic conversion electrons of Kr-83m as natural standard. During a krypton calibration measurement campaign in 2017 at KATRIN [62], gaseous Kr-83m was injected into the WGTS. This isotope decays via two cascaded gamma transition, both highly converted into the emission of conversion electrons, offering multiple lines with various energies up to 35 keV. The kinetic energy depends i.a. on the gamma transition- and atomic binding energy, which are known from spectroscopic measurements. Hence, the HV system of KATRIN can be calibrated by measuring the energy of a known conversion electron line with the main spectrometer. In order to reach ppm-precision, the difference of two conversion electron lines from the same nuclear transition, but from different atomic shells, was used. Thereby, systematic uncertainties (like the work function difference between source and spectrometer or the energy of the gamma transition) – not known to the 10 meV level – cancel out. The K35 was calibrated with conversion electrons from the K- and $L_3 - 32$ line, resulting in a scale factor of $M_{\mathrm{K35}} = 1972.449(10)$. This deviates by $-2(5)\,\mathrm{ppm}$ to the calibration value measured at PTB in 2013, confirming that the K35 is stable on ppm-level per year or better. The uncertainty of this calibration method is dominated by the uncertainty of the difference of the atomic binding energies of about 4 ppm, which could improve in the next years

by more precise spectroscopic measurements.

This calibration method and the results presented in this thesis were published in the Journal European Physical Journal C (EPJ C) in 2018 [102].

Later this year, the K65 HV divider – currently located at the Institut für Kernphysik in Münster – will be transported to KATRIN in Karlsruhe together with the equipment for the newly developed absolute calibration method based on the differential scale factor. There, cross-calibration measurements of the K35 and K65 are planned, and both dividers will be calibrated regularly with the two calibration procedures developed in the context of this thesis. Thereby it is ensured, that the HV monitoring system at KATRIN fulfills all requirements needed to reach the design goal of measuring the neutrino mass with a sensitivity of $0.2\,\mathrm{eV\,c^{-2}}$.

Bibliography

[1] J. A. Formaggio and G. P. Zeller, "From ev to eev: Neutrino cross sections across energy scales," *Rev. Mod. Phys.*, vol. 84, pp. 1307–1341, Sep 2012.

[2] C. W. W. for the Super-Kamiokande collaboration, *The Super-Kamiokande Experiment*, pp. 19–43.

[3] A. Bellerive, J. Klein, A. McDonald, A. Noble, and A. Poon, "The sudbury neutrino observatory," *Nuclear Physics B*, vol. 908, pp. 30 – 51, 2016. Neutrino Oscillations: Celebrating the Nobel Prize in Physics 2015.

[4] F. Halzen and S. R. Klein, "Invited review article: Icecube: An instrument for neutrino astronomy," *Review of Scientific Instruments*, vol. 81, no. 8, p. 081101, 2010.

[5] M. Tanabashi *et al.*, "Review of particle physics," *Phys. Rev. D*, vol. 98, p. 030001, Aug 2018.

[6] V. M. Lobashev, "The search for the neutrino mass by direct method in the tritium beta-decay and perspectives of study it in the project KATRIN," *Nucl. Phys.*, vol. A719, pp. 153–160, 2003.

[7] C. Kraus *et al.*, "Final results from phase II of the Mainz neutrino mass search in tritium beta decay," *Eur. Phys. J.*, vol. C40, pp. 447–468, 2005.

[8] C. Grupen, *Astroparticle Physics.* Springer, 2005.

[9] K. Zuber, *Neutrino Physics.* Taylor and Francis Group, LLC, 2004.

[10] J. Chadwick, "Intensitaetsverteilung im magnetischen spektrum der b-strahlen von radium b+c," *Verhandlungen der deutschen Physikalischen Gesellschaft 16 (1914) 383*, 1914.

[11] W. Pauli, "Offener brief an die gruppe der radioaktiven bei der gauvereinstagung zu tübingen," *Letter*, 1930.

[12] J. Chadwick, "Possible existence of a neutron," *Nature*, vol. 129, no. 3252, pp. 312–312, 1932.

[13] E. Fermi, "Versuch einer theorie der β-strahlen. i," *Zeitschrift für Physik*, vol. 88, pp. 161–177, Mar 1934.

[14] C. L. Cowan, F. Reines, F. B. Harrison, H. W. Kruse, and A. D. McGuire, "Detection of the free neutrino: a confirmation," *Science*, vol. 124, no. 3212, pp. 103–104, 1956.

[15] F. Reines and C. L. Cowan, "Free antineutrino absorption cross section. i. measurement of the free antineutrino absorption cross section by protons," *Phys. Rev.*, vol. 113, pp. 273–279, Jan 1959.

[16] S. Mele, "The Measurement of the Number of Light Neutrino Species at LEP," *Adv. Ser. Direct. High Energy Phys.*, vol. 23, pp. 89–106, 2015.

[17] R. Adhikari *et al.*, "A white paper on keV sterile neutrino dark matter," *Journal of Cosmology and Astroparticle Physics*, vol. 2017, pp. 025–025, jan 2017.

[18] M. Agostini *et al.*, "Comprehensive measurement of pp-chain solar neutrinos," *Nature*, vol. 562, no. 7728, pp. 505–510, 2018.

[19] R. J. Davis and J. J. Evans, "Report on the brookhaven solar neutrino experiment,"

[20] B. T. Cleveland, T. Daily, R. Davis, Jr., J. R. Distel, K. Lande, C. K. Lee, P. S. Wildenhain, and J. Ullman, "Measurement of the solar electron neutrino flux with the Homestake chlorine detector," *Astrophys. J.*, vol. 496, pp. 505–526, 1998.

[21] A. B. McDonald, "Sudbury neutrino observatory results," *Physica Scripta*, vol. T121, pp. 29–32, jan 2005.

[22] S. Turck-Chièze, S. Couvidat, L. Piau, J. Ferguson, P. Lambert, J. Ballot, R. A. García, and P. Nghiem, "Surprising sun: A new step towards a complete picture?," *Phys. Rev. Lett.*, vol. 93, p. 211102, Nov 2004.

[23] T. GERSHON, "Overview of the cabibbo–kobayashi–maskawa matrix†," *Pramana*, vol. 79, pp. 1091–1108, Nov 2012.

[24] A. Yu. Smirnov, "The MSW effect and solar neutrinos," in *Neutrino telescopes. Proceedings, 10th International Workshop, Venice, Italy, March 11-14, 2003. Vol. 1+2*, pp. 23–43, 2019.

[25] Planck Collaboration, "Planck 2015 results - xiii. cosmological parameters," *A&A*, vol. 594, p. A13, 2016.

[26] S. R. Elliott, A. A. Hahn, and M. K. Moe, "Direct Evidence for Two Neutrino Double Beta Decay in ^{82}Se," *Phys. Rev. Lett.*, vol. 59, pp. 2020–2023, 1987. [,989(1987)].

[27] M. Agostini *et al.*, "Improved limit on neutrinoless double-β decay of ^{76}Ge from gerda phase ii," *Phys. Rev. Lett.*, vol. 120, p. 132503, Mar 2018.

[28] KATRIN collaboration, *KATRIN design report.*

[29] G. Drexlin, V. Hannen, S. Mertens, and C. Weinheimer, "Current direct neutrino mass experiments," *Adv. High Energy Phys.*, vol. 2013, p. 293986, 2013.

[30] F. T. Harms, *Characterization and Minimization of Background Processes in the KATRIN Main Spectrometer.* PhD thesis, 2015. 51.03.01; LK 01.

[31] M. Arenz *et al.*, "Katrin design report 2.0," *(KATRIN collaboration), to be published*, 2019.

[32] M. Babutzka, *Design and development for the Rearsection of the KATRIN experiment.* PhD thesis, 2014.

[33] M. Kraus, *Energy-Scale Systematics at the KATRIN Main Spectrometer.* PhD thesis, Karlsruher Institut für Technologie (KIT), 2016.

[34] KATRIN collaboration, "KATRIN homepage," 2019.

[35] B. Ostrick, "Eine kondensierte 83mkr-kalibrationsquelle für das katrin-experiment," *doctoral thesis, University of Münster*, 2009.

[36] S. Bauer, "Energy calibration and stability monitoring of the katrin experiment," *doctoral thesis, University of Münster*, 2013.

[37] S. Dyba, "Background reduction by the inner wire electrode and set-up of the condensed krypton source at the neutrino mass experiment katrin," *doctoral thesis, University of Münster*, 2019.

[38] N. Wandkowsky, *Study of background and transmission properties of the KATRIN spectrometers.* PhD thesis, 2013.

[39] A. Picard *et al.*, "A solenoid retarding spectrometer with high resolution and transmission for kev electrons," *Nuclear Instruments and Methods in Physics Research Section B: Beam Interactions with Materials and Atoms*, vol. 63, no. 3, pp. 345 – 358, 1992.

[40] K. Bokeloh, "Calibration of hot and cold dark matter experiments," *doctoral thesis, University of Münster*, 2014.

[41] J. D. Jackson, *Classical electrodynamics.* New York, NY: Wiley, 3rd ed. ed., 1999.

[42] M. Arenz *et al.*, "Commissioning of the vacuum system of the KATRIN main spectrometer," *Journal of Instrumentation*, vol. 11, pp. P04011–P04011, apr 2016.

[43] M. Arenz *et al.*, "Reduction of stored-particle background by a magnetic pulse method at the katrin experiment," *The European Physical Journal C*, vol. 78, p. 778, Sep 2018.

[44] J. Behrens, "Design and commissioning of a monoenergetic photoelectron source and active background reduction by magnetic pulse at the katrin experiment," *doctoral thesis, University of Münster*, 2016.

[45] K. Valerius, "Spektrometeruntergrund und seine unterdrückung beim katrin experiment," *doctoral thesis, University of Münster*, 2009.

[46] M. Prall, "Background reduction of the katrin spectrometers: Transmission function of the pre-spectrometer and systematic test of the main-spectrometer wire electrode," *doctoral thesis, University of Münster*, 2011.

[47] O. Rest, "Inbetriebnahme der präzisionshochspannung am hauptspektrometer des katrin-experiments," *master thesis, University of Münster*, 2014.

[48] M. Erhard *et al.*, "High-voltage monitoring with a solenoid retarding spectrometer at the KATRIN experiment," *JINST*, vol. 9, p. P06022, 2014.

[49] M. Arenz, "Production and pac studies of kr-83m solid state calibration sources for the katrin experiment," *doctoral thesis, University of Bonn*, 2017.

[50] M. Zboril, "Solid electron sources for the energy scale monitoring in the katrin experiment," *doctoral thesis, University of Münster*, 2011.

[51] M. Slezák, "Monitoring of the energy scale in the katrin neutrino experiment," *PhD thesis, Nuclear Physics Institute Czech Academy of Sciences*, 2015.

[52] M. Kleesiek, *A Data-Analysis and Sensitivity-Optimization Framework for the KATRIN Experiment*. PhD thesis, 2014.

[53] N. Steinbrink, V. Hannen, E. L. Martin, R. G. H. Robertson, M. Zacher, and C. Weinheimer, "Neutrino mass sensitivity by MAC-e-filter based time-of-flight spectroscopy with the example of KATRIN," *New Journal of Physics*, vol. 15, p. 113020, nov 2013.

[54] N. M. N. Steinbrink, J. D. Behrens, S. Mertens, P. C.-O. Ranitzsch, and C. Weinheimer, "kev-scale sterile neutrino sensitivity estimation with time-of-flight spectroscopy in katrin using self-consistent approximate monte carlo," *The European Physical Journal C*, vol. 78, p. 212, Mar 2018.

[55] D. Furse *et al.*, "Kassiopeia: a modern, extensible c++ particle tracking package," *New Journal of Physics*, vol. 19, no. 5, p. 053012, 2017.

[56] J. Behrens *et al.*, "A pulsed, mono-energetic and angular-selective uv photo-electron source for the commissioning of the katrin experiment," *The European Physical Journal C*, vol. 77, p. 410, Jun 2017.

[57] S. Groh, *Modeling of the response function and measurement of transmission properties of the KATRIN experiment.* PhD thesis, 2015.

[58] M. Kleesiek, J. Behrens, G. Drexlin, K. Eitel, M. Erhard, J. A. Formaggio, F. Glück, S. Groh, M. Hötzel, S. Mertens, A. W. P. Poon, C. Weinheimer, and K. Valerius, "β-decay spectrum, response function and statistical model for neutrino mass measurements with the katrin experiment," *The European Physical Journal C*, vol. 79, p. 204, Mar 2019.

[59] L. I. Bodine, D. S. Parno, and R. G. H. Robertson, "Assessment of molecular effects on neutrino mass measurements from tritium β decay," *Phys. Rev. C*, vol. 91, p. 035505, Mar 2015.

[60] T. Thümmler, "Praezisionsueberwachung und kalibration der hochspannung für das katrin-experiment," *doctoral thesis, University of Münster*, 2007.

[61] R. Behr, O. Kieler, J. Kohlmann, F. Müller, and L. Palafox, "Development and metrological applications of josephson arrays at ptb," *Measurement Science and Technology*, vol. 23, no. 12, p. 124002, 2012.

[62] M. Arenz *et al.*, "First transmission of electrons and ions through the KATRIN beamline," *Journal of Instrumentation*, vol. 13, pp. P04020–P04020, apr 2018.

[63] D. Venos *et al.*, "Katrin krypton mode," *KATRIN internal report*, 2016.

[64] M. Arenz *et al.*, "First spectroscopic measurements of conversion electrons using gaseous krypton at katrin," *(KATRIN collaboration), to be published*, 2019.

[65] S. Bauer, B. Grees, D. Spitzer, M. Beck, R. Bottesch, H.-W. Ortjohann, B. Ostrick, T. Schäfer, H. H. Telle, A. Wegmann, M. Zbořil, and C. Weinheimer, "Ellipsometry with polarisation analysis at cryogenic temperatures inside a vacuum chamber," *Review of Scientific Instruments*, vol. 84, no. 12, p. 123103, 2013.

[66] M. Fedkevych *doctoral thesis, University of Münster*, expected 2019.

[67] C. W. Leming and G. L. Pollack, "Sublimation pressures of solid ar, kr, and xe," *Phys. Rev. B*, vol. 2, pp. 3323–3330, Oct 1970.

[68] R. Pöpel, "The josephson effect and voltage standards," *Metrologia*, vol. 29, pp. 153–174, jan 1992.

[69] Fluke, *Fluke 732A Instruction Manual.*

[70] F. James, *MINUIT - Function Minimization and Error Analysis.* CERN Geneva, March 1994.

[71] T. Thümmler, R. Marx, and C. Weinheimer, "Precision high voltage divider for the KATRIN experiment," *New J. Phys.*, vol. 11, p. 103007, 2009.

[72] S. Bauer, R. Berendes, F. Hochschulz, H. W. Ortjohann, S. Rosendahl, T. Thümmler, M. Schmidt, and C. Weinheimer, "Next generation KATRIN high precision voltage divider for voltages up to 65kV," *JINST*, vol. 8, p. P10026, 2013.

[73] S. Rosendahl, "Präzisionshochspannung für das katrin-experiment," *diploma thesis, University of Münster*, 2011.

[74] B. Hillen, "Untersuchung von methoden zur unterdrückung des spektrometeruntergrunds beim katrin-experiment," *doctoral thesis, University of Münster*, 2011.

[75] S. Benning, "Entwicklung eines lasersensors und feldemissionsuntersuchungen für die drahtelektrode im katrin-hauptspektrometer," *diploma thesis, University of Münster*, 2010.

[76] FuG Elektronik GmbH, *Manual HV Supply HCP 70M-35000*, 2013.

[77] J. Barrett *et al.*, "Results of the

first KATRIN SDS measurement phase," *KATRIN internal report*, 2014.

[78] C. Rodenbeck *doctoral thesis, University of Münster*, expected 2021.

[79] F. M. Fränkle, *Background Investigations of the KATRIN Pre-Spectrometer*. PhD thesis, 2010.

[80] J. Behrens, V. Hannen, O. Rest, and D. Winzen, "Overview of e-gun measurements at the monitor spectrometer," *KATRIN internal report*, 2014.

[81] R. Marx, "New concept of ptbs standard divider for direct voltages of up to 100 kv," *IEEE Transactions on Instrumentation and Measurement*, vol. 50, pp. 426–429, April 2001.

[82] J. Ullmann, Z. Andelkovic, C. Brandau, A. Dax, W. Geithner, C. Geppert, C. Gorges, M. Hammen, V. Hannen, S. Kaufmann, K. König, Y. A. Litvinov, M. Lochmann, B. Maaß, J. Meisner, T. Murböck, R. Sánchez, M. Schmidt, S. Schmidt, M. Steck, T. Stöhlker, R. C. Thompson, C. Trageser, J. Vollbrecht, C. Weinheimer, and W. Nörtershäuser, "High precision hyperfine measurements in bismuth challenge bound-state strong-field qed," *Nature Communications*, vol. 8, pp. 15484 EP –, 05 2017.

[83] O. Dragoun, A. Špalek, and F. Wuilleumier, "Increased accuracy of the binding energy of k- and l-subshell electrons in krypton from re-analysis of experimental data: Importance for determination of the neutrino mass," *Czechoslovak Journal of Physics*, vol. 54, pp. 833–839, Aug 2004.

[84] P. van der Heide, *XPS Instrumentation*, pp. 27–60. John Wiley and Sons, Inc., 2011.

[85] A. D. Andersen, "No transition without transmission: Hvdc electricity infrastructure as an enabler for renewable energy?," *Environmental Innovation and Societal Transitions*, vol. 13, pp. 75 – 95, 2014.

[86] S. L. Teichler and I. Levitine, "Hvdc transmission: A path to the future?," *The Electricity Journal*, vol. 23, no. 4, pp. 27 – 41, 2010.

[87] C. Humpert, "Long distance transmission systems for the future electricity supply – analysis of possibilities and restrictions," *Energy*, vol. 48, no. 1, pp. 278 – 283, 2012. 6th Dubrovnik Conference on Sustainable Development of Energy Water and Environmental Systems, SDEWES 2011.

[88] E. Pierri, O. Binder, N. G. Hemdan, and M. Kurrat, "Challenges and opportunities for a european hvdc grid," *Renewable and Sustainable Energy Reviews*, vol. 70, pp. 427 – 456, 2017.

[89] O. Vestergaard, "Hvdc - enabling the transition to an energy system based on renewables," *IET Conference Proceedings*, pp. 31–31(1), January 2010.

[90] D. Winzen *doctoral thesis, University of Münster*, expected 2019.

[91] O. Rest, V. Hannen, D. Winzen, and C. Weinheimer, "Absolute calibration of a ppm-precise HV divider for the electron cooler of the ion storage ring CRYRING@ESR," *Accepted for publication in Lecture Notes in Electrical Engineering*, 2019.

[92] O. Rest, D. Winzen, S. Bauer, R. Berendes, J. Meisner, T. Thümmler, S. Wüstling, and C. Weinheimer, "A novel ppm-precise absolute calibration method forprecision high-voltage dividers." arXiv:1903.01261, 2019.

[93] J. Meisner, S. Passon, A.-P. Elg, K. König, J. Krämer, W. Nörtershäuser, O. Rest, C. Weinheimer, and D. Winzen, "Comparison of Four Different ppm-level Methods for Traceability of HVDC Measuring Systems," *Accepted for publication in Lecture Notes in Electrical Engineering*, 2019.

[94] VISHAY Israel, *Hermetically Sealed High Precision Bulk Metal Foil Technology Resistors*.

[95] D. Nandedkar, "Analysis of conductivity of noble metals near room temperature," *Journal of Physics, Public Service Framework, American Institute of Science, Delaware, U.S.A.*, vol. 1, pp. 255–265, 10 2015.

[96] M. Myers, "The performance implications of silver as a contact finish in traditionally gold finished contact applications," in *2009 Proceedings of the 55th IEEE Holm Conference on Electrical Contacts*, pp. 310–318, Sep. 2009.

[97] R. Bauer, "Sulfide corrosion of silver contacts during satellite storage," *Journal of Spacecraft and Rockets - J SPACECRAFT ROCKET*, vol. 25, p. 12, 03 1988.

[98] Fluke, *Fluke 752A Instruction Manual*.

[99] J. Krämer, K. König, C. Geppert, P. Imgram, B. Maaß, J. Meisner, E. W. Otten, S. Passon, T. Ratajczyk, J. Ullmann, and W. Nörtershäuser, "High voltage measurements on the 5 ppm relative uncertainty level with collinear laser spectroscopy," *Metrologia*, 2018.

[100] Caddock Electronics, Inc., *Type USF Ultra-Stable Low TC Film Resistors 200 Series and 300 Series*, 2017.

[101] J. Sentkerestiová, D. Vénos, and M. Slezák, "Gaseous 83m kr generator of monoenergetic electrons based on 83 rb deposited in zeolite," *Journal of Physics: Conference Series*, vol. 888, no. 1, p. 012072, 2017.

[102] M. Arenz *et al.*, "Calibration of high voltages at the ppm level by the difference of kr-83m conversion electron lines at the katrin experiment," *The European Physical Journal C*, vol. 78, p. 368, May 2018.

[103] E. McCutchan, "Nuclear data sheets for a = 83," *Nuclear Data Sheets*, vol. 125, no. Supplement C, pp. 201 – 394, 2015.

[104] A. Fulst *doctoral thesis, University of Münster*, expected 2020.

[105] C. Weinheimer, "Can the N2-/N3-32 doublet be resolved? ," *electronic logbook Krypton 2017 (entry 103), KATRIN internal site*, 2017.

List of Abbreviations

AC	Alternating Current
AFG	Arbitrary Function Generator
CKrS	Condensed Krypton Source
CPS	Cryogenic Pumping Section
DC	Direct Current
DPS	Differential Pumping Section
DVM	Digital Voltmeter
FPD	Focal Plane Detector
GKrS	Gaseous Krypton Source
HF	High-Frequent
HV	High Voltage
HVC	High-Voltage Calibration
IE	Inner wire Electrode system
KATRIN	Karlsruhe Tritium Neutrino Experiment
KIT	Karlsruhe Institute of Technology
LVC	Low-Voltage Calibration
MAC-E-Filter	Magnetic Adiabatic Collimation with an Electrostatic Filter
MoS	Monitor Spectrometer
MS	Main Spectrometer
ppm	parts per million
PS	Pre-Spectrometer
PTB	Physikalisch-Technische Bundesanstalt
SCS	SlowControl System
SDS	Spectrometer Detector Section
SKrS	Solid (implanted) Krypton Source
STS	Source and Transport Section
TLK	Tritium Laboratory Karlsruhe
WGTS	Windowless Gaseous Tritium Source

Ich möchte mich außerdem bei der gesamten AG Weinheimer und den Kollegen am KIT in Karlsruhe für die positive Arbeitsatmosphäre, den Spaß und die erfolgreiche gemeinsame Zusammenarbeit bedanken. Ganz besonders danke ich Stephan Dyba, mit dem ich den Großteil der Zeit das Büro und auf gemeinsamen Dienstreisen stets das Zimmer teilen durfte. Ich hoffe, dass wir den Kontakt nicht abreißen lassen und in Zukunft vielleicht wieder wie in den letzten Jahren üblich den Abschluss des alten und Beginn des neuen Jahres zusammen feiern können :) Außerdem danke ich den ehemaligen Kollegen aus der Arbeitsgruppe (Stephan B., Philipp R., Stephan R., Jan B., Nicholas S. und Jonas V.) für die gute Zusammenarbeit und den gemeinsamen Spaß.

Einen besonderen Dank möchte ich nun Daniel aussprechen. Zusammen haben wir unzählige Stunden im HV-Labor verbracht, gemeinsam über Auswertungen und Analysen gerätselt und dabei trotz diverser Rückschläge immer weiter gemacht und den Spaß nicht aus den Augen verloren. Neben der Arbeit hatten wir außerdem noch viele lockere und ernste Gesprächsthemen, sodass uns nie langweilig wurde. Wir haben aufgrund der Überschneidungen unserer Themen häufig sehr eng und vertrauensvoll zusammen gearbeitet und uns immer gegenseitig unterstützt. Vielen Dank!

Neben dem Studium und der Arbeit darf man den Spaß abseits dieser Themen nicht vernachlässigen. Dafür (und für die fachliche Unterstützung natürlich auch) möchte ich mich bei Nils, Christopher, Alex und Michael bedanken. Jetzt haben wir es alle tatsächlich hinter uns gebracht und sind gemeinsam über die letzten Jahre durch den Parkour der Promotion geschritten. Zahlreiche lustige und entspannte Abende (zum Beispiel unsere gemeinsamen SuperBowl Nächte) und Ausflüge zum Saison-Abschluss werden mir dabei noch lange in Erinnerung bleiben. Alex möchte ich außerdem für den spannenden gemeinsamen Kurzurlaub in Toronto danken. Für zahlreiche gemeinsame Film- und Serien Marathons an den Wochenenden und einen für immer unvergesslichen Roadtrip durch Kalifornien möchte ich Michael besonders danken. Zusammen mit Euch allen waren die letzten fünf Jahre eine spannende und ereignisreiche Reise, an die ich mich in Zukunft gerne erinnern werde.

Zuletzt möchte ich mich natürlich auch bei meiner gesamten Familie bedanken, die mich in den letzten Jahren und darüber hinaus immer unterstützt hat. Ganz besonders gilt der Dank meinen Eltern, die mich von Anfang an ermutigt, mich immer begleitet und mir stets den Rücken frei gehalten haben. Danke, dass ich mich immer auf Euch verlassen kann. Gerade die letzten Monaten der Promotion haben unter dem Druck der Zeit nochmal eine neue Herausforderung dargestellt. Dafür, dass Du mich in dieser anstrengenden Zeit immer unterstützt, mich zum Lachen und auch mal auf andere Gedanken gebracht hast, möchte ich Dir, Eva, ganz besonders danken. Nur dank Euch bin ich an diesen Punkt gekommen und mit Euch schaue ich vertrauensvoll und freudig in die Zukunft.

Oliver Rest

Persönliche Informationen

Geburtsdatum	26.12.1988	Familienstand	ledig
Geburtsort	Lingen (Ems)	Staatsangehörigkeit	deutsch

Ausbildung

2011–2014 **Master of Science Physik**, *Westfälische Wilhelms-Universität*, Münster, *Note: 1,3*.

2008–2011 **Bachelor of Science Physik**, *Westfälische Wilhelms-Universität*, Münster, *Note: 2,3*.

1999–2008 **Abitur**, *Franziskusgymnasium*, Lingen (Ems), *Note: 2,4*.

Abschlussarbeiten

2014 **Inbetriebnahme der Präzisionshochspannung am Hauptspektrometer des KATRIN-Experiments**, *Masterarbeit*, WWU Münster, Prof. Dr. C. Weinheimer.
Note: 1,0

2011 **Aufbau und Test eines Elektronenmonitordetektors für das KATRIN-Experiment**, *Bachelorarbeit*, WWU Münster, Prof. Dr. C. Weinheimer.
Note: 1,0

Promotion

05/2014 **Beginn der Promotion (Dr. rer. nat.)**, *Westfälische Wilhelms-Universität*, Münster, Institut für Kernphysik.
Betreuer: Prof. Dr. C. Weinheimer

Publikationen (Auswahl)

2019 **Absolute calibration of a ppm-precise HV divider for the electron cooler of the ion storage ring CRYRING@ESR**, *Accepted by SPRINGER series Lecture Notes in Electrical Engineering*, O. Rest et al., Corresponding Author.

2019 **A novel ppm-precise absolute calibration method for precision high-voltage dividers**, *Submitted to Metrologia in April 2019*, O. Rest et al., Corresponding Author.

2018 **Calibration of high voltages at the ppm level by the difference of Kr-83m conversion electron lines at the KATRIN experiment**, *Eur. Phys. J. C (2018) 78:368*, KATRIN Kollaboration, Corresponding Author.

Clevornstr. 12 – 48153 – Münster
℘ *0151 2525 4188* • ✉ *oliver.rest@googlemail.com*

Berufserfahrung

05/2014–07/2019 **Wissenschaftlicher Mitarbeiter**, *Westfälische Wilhelms-Universität*, Münster.
Arbeitsgruppe Prof. Dr. C. Weinheimer

10/2012–02/2014 **Studentische Hilfskraft**, *Westfälische Wilhelms-Universität*, Münster.
Betreuung experimenteller Übungen von Studierenden mit Nebenfach Physik

12/2011–07/2012 **Studentische Hilfskraft**, *Westfälische Wilhelms-Universität*, Münster.
Arbeitsgruppe Prof. Dr. C. Weinheimer

Eingeladene Vorträge

12/2018 **Physikalisch-Technische Bundesanstalt**, *The KATRIN neutrino mass experiment: A new challenge for precision high voltage at the ppm level*, Braunschweig.

11/2018 **APPEC Technology Forum 2018**, *Longterm stabilization and voltage reference at the KATRIN experiment*, Veldhoven (NL).

06/2018 **Technische Universität Darmstadt**, *High voltage and energy calibration of the KATRIN experiment*, Darmstadt.

Konferenzen (Auswahl)

2017 **TAUP 2017**, *Sudbury (CA)*, Posterpräsentation.
Calibration of the high voltage and the energy scale of the KATRIN experiment
Auszeichnung mit 2. Platz für den Posterpreis (44 Teilnehmer)

2016 **Neutrino 2016**, *London (GB)*, Posterpräsentation.
Energy calibration of the KATRIN experiment

2011–2019 **Frühjahrstagung der Deutschen Physikalischen Gesellschaft**, *Diverse Vorträge und Posterpräsentationen*, 2016 Posterpräsentation in Darmstadt.
Calibration of the precision high voltage dividers of the KATRIN experiment
Auszeichnung mit 1. Platz für den Posterpreis (102 Teilnehmer)

2011–2018 **Internationales KATRIN Kollaborationsmeeting**, *Diverse Vorträge*.